Fabrication and Characterisation of III-nitride light emitting diodes emitting at non-standard wavelengths

Cavanagh, Kate Frances

Award date:
2019

Awarding institution:
University of Bath

Fabrication and Characterisation of III-nitride light emitting diodes emitting at non-standard wavelengths

submitted by

Kate Frances Cavanagh

for the degree of Doctor of Philosophy

of the

University of Bath

Department of Electronic and Electronic Engineering

December 2017

Acknowledgements

I would like to than my supervisory team; Dr.Duncan Allsopp, Dr.Philip Sheilds and Prof.Wang Nang Wang for the opportunity to do this work.

A huge thank you to Siva Sivaraya, for all of the help, support and teaching over the years. None of this would be possible without you.

Thank you to the GaN group in Bath; Pierre-Marie, Pierre, Simon, Szymon, Jiang, Paulo, Chris, Margaret and Manu. A special thanks to Sophie, for being an amazing colleague and friend. Thanks also to the various project students who have helped over the years.

Thank you to all the technicians; Stephen, Richard, Wendy and the staff in MAS, for making all of this possible.

I would like to thank Juraj and Alex at STUBA for the characterisation they provided and for their hospitality. Thanks also to Plasma Quest Ltd, especially James and Sarah, for providing samples and allowing me to use their characterisation equipment. Thanks to Chaowang Liu of IQE for providing samples.

Thank you to Jason and Shelley at Imperial College for inviting me to work on their UV device project. Further thanks to Jason for all of his support and friendship throughout. I would like to thank all my friends but especially Rachel, Peter, Kim, Criostoir, David, Ed and Rob for their unwavering love, support and friendship. I would especially like to thank my dear friend, Damyan, who not only spend a summer helping in the lab but has been a wonderful friend too.

Abby Osborne, thank you for everything you have done. Honestly none of this is possible without you.

Finally I would like to thank my family. My parents Sarah and Dermot for always pushing me, believing me and supporting me. Thanks also to my sister Ruth, brother-in-law Michael and nieces Tanith and Astara for all the love and support.

Abstract

This thesis details research centering around GaN based light emitting diodes (LEDs) emitting at non-standard wavelengths i.e. outside of the blue region of the electromagnetic spectrum.

The first part of the work focuses on developing a simple procedure which allows for the characterisation for loss mechanisms in high indium content LEDs. A strong quantum confined stark effect was observed and had a strong correlation with Poole-Frenkle emission, high forward and reverse bias leakage currents, reverse bias emission and suppressed light emission. These effects are largely attributed to epitaxy.

The use of thin metal interlayer was studied as a means of improving current spreading layers. It was found that the inclusion of a thin Ni layer improved the contact resistance, leakage and wall plug efficiency of devices with both ITO and AZO contacts. Further to this it was found that annealing in O_2 and slightly increasing the thickness of the metal layer improved device characteristics.

Finally a series of experiments showed that a structure free of a p-type layer could be used as a source of UV emission. These devices exhibited resonant tunnelling behaviour which correlated to enhanced light output.

Contents

Chapter 1

Introduction

Light emitting diodes (LEDs) have attracted significant interest in recent years due to their potential for energy saving in commercial and household lighting, automotive lighting, visual signs and display applications. In fact the impact LEDs have made, in particular those emitting in the blue region, was reflected when the 2014 Nobel prize for Physics was awarded to the pioneers of the gallium nitride (GaN)/ indium gallium nitride (InGaN) LED, Isamu Akasaki, Hiroshi Amano and Shuji Nakamura. Whilst significant progress has been made, the challenge of achieving high efficiencies across the visible range remains.

The region which poses most difficulty in realising high efficiency lies between the blue and the red visible light regions of the electromagnetic spectrum and is known as the "green gap". Further introduction to this can be found in section 1.5, with a more detailed discussion following in section 2.1.2. It is this which provides the motivation for this work. As well as the push for high brightness high efficiency LEDs, reduced price and improved colour rendering index (CRI) are significant motivators. Indeed a particular aim of this research is to discover the causes of lower efficiency for LEDs emitting in green-yellow light.

1.1 A brief history of LEDs

The discovery of electroluminescence was made in the early 1900's by H.J Round, using a point metallic contact on silicon carbide (SiC) [1]. Nearly two decades later, Oleg Losev, announced the creation of the first LED [2]. The first modern LED (i.e with a p-n or p-i-n structure) was developed by accident in 1961 at

Texas instruments by James Biard and Gary Pittman. It was a gallium arsenide (GaAs) based device which emitted infra-red radiation. The following year Nick Holonyak Jr of General Electrics Company created the first LED to emit visible light, in this case red. This device employed gallium arsenide phosphide (GaAsP) on a GaAs substrate. It would be a further decade before LEDs would venture out of the infra-red/red region of the electromagnetic spectrum. In 1972, Monsanto's George Crawford developed the first yellow emitting device, which also used GaAsP [3]. Crawford also developed an improved red LED. The same year saw the realisation of the violet LED. Herber Maruska and Jacques Pankove of RCA labs, employed Mg-doped gallium nitride (GaN) films [4] and thus laid the foundations for modern III-nitride based devices and the creation of the blue LED, although such developments would take several decades to be realised.

Progress was rapid and the 1970's saw additional colours become available. LEDs were now sought for a huge range of applications and demand soared as cost dropped and brightness increased.

The early 1990's brought the long awaited blue LED, created by Shuji Nakamura at Nichia Corporation [5] [6] [7]. At the same time, Isamu Akasaki [8] and Hiroshi Amano, working at Nagoya made breakthroughs in the development of p-type doping GaN. This was critical in furthering the efficiency of such devices. This and Nakamura's work resulted in the first white light LED, and changed the landscape of household and commercial lighting applications, especially with regards to energy saving.

1.2 Recombination Mechanisms

Recombination describes the process in which electrons and holes in a semiconductor come together and annihilate accompanied by a release of energy. This released energy can either be described as radiative or non-radiative, depending on whether or not a photon is emitted. Whilst the non-useful non-radiative processes (which emits energy as heat rather than light) cannot be eliminated, there are various approaches to enhancing the useful, radiative process. The summation of radiative and non-radiative processes, used to determine the internal quantum efficiency (η_{IQE}) (see equation (1.1)), is commonly known as the ABC model, details of which can be found in [9]. Based on this model the intrinsic

efficiency of material or device in converting electric current into light is given by:

$$\eta_{IQE} = \eta_{inj} \frac{Bn^2}{An + Bn^2 + Cn^3} \tag{1.1}$$

Where η_{IQE} is known as the internal quantum efficiency and A,B and C relate to Shockley-Read-Hall, radiative, and Auger recombination respectively. The injection efficiency is denoted η_{inj}. Factor n is the electron density which is assumed to equal the hole density, since each electron lost to non-radiative recombination necessarily involves the simultaneous loss of a hole. Recombination, illustrated schematically in Figure 1-1,is discussed next.

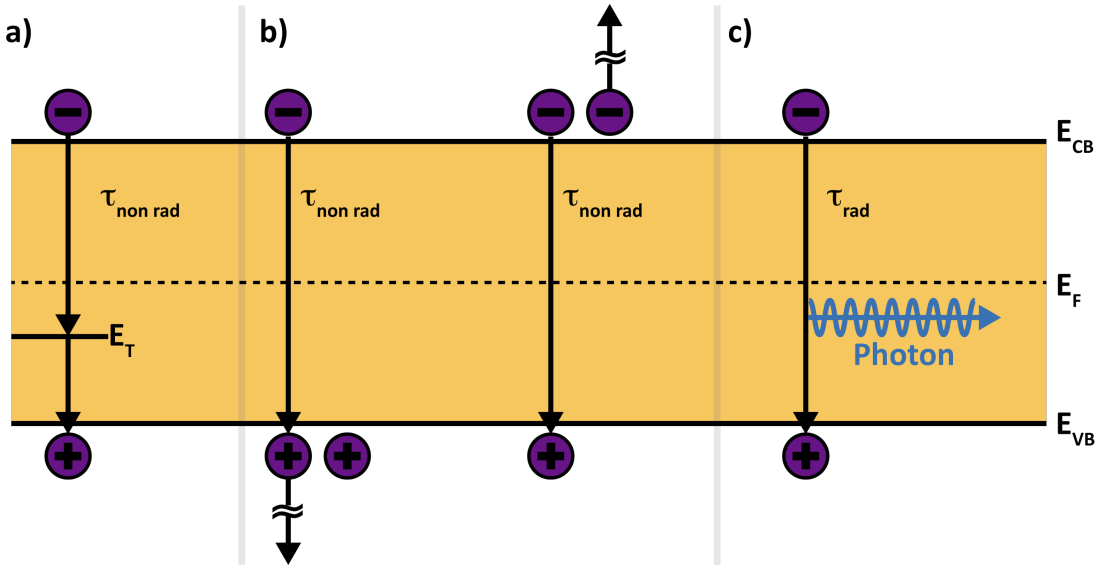

Figure 1-1: Recombination mechanisms. (a) SRH recombination (b) Auger recombination (c) Radiative recombination. Replicated from [10]

1.2.1 Radiative Recombination

Radiative recombination is the phenomenon in which electrons and holes in a semiconductor recombine and a photon is emitted, the wavelength of which is determined by the energy difference of the quantum states of the electron and hole, which in an LED can be approximated by the bandgap of the material. It is of course most prevalent in direct bandgap semiconductors, due to the necessity to conserve momentum as well as energy in a recombination event. A more detailed discussion of Equations (1.2) - (1.14) can be found in Schubert textbook [10].

Under equilibrium conditions the product of free carrier concentrations (that is electron concentration,n_0 and hole concentration,p_0), is proportional to the square of the intrinsic carrier concentration n_i, i.e.

$$n_0 p_0 = {n_i}^2 \tag{1.2}$$

Radiative recombination only becomes manifest when excess non-equilibrium concentrations of electrons and holes are present in a direct band gap semiconductor. Thus it is possible to use an injected current or light to generate an excess of carriers. The summation of excess and equilibrium carrier concentrations is used to determine the total concentration of carriers, i.e.

$$n = n_0 + \Delta n \tag{1.3}$$

$$p = p_0 + \Delta p \tag{1.4}$$

As previously stated, electrons and holes recombine and release energy. So intuitively, as recombination occurs the concentration of carriers will decrease if only a pulse of electrons and/or holes are injected into the semiconductor. The rate of recombination is therefore related to changes in the carrier concentration. The relationship is described in the following equation.

$$R = -\frac{dn}{dt} = -\frac{dp}{dt} = Bnp \tag{1.5}$$

B is known as the bimolecular radiative recombination coefficient and is calculated using the van Roosbroeck-Shockley model (see [10]). When a semiconductor undergoes excitation by absorbing photons excess electrons and holes are generated in pairs. This means that the excess concentrations of electrons and holes are equal;

$$\Delta n(t) = \Delta p(t) \tag{1.6}$$

When the excitation level is low, the concentration of majority carriers is much greater than that of the generated excess of carriers. This results in a rate equation which is the sum of the equilibrium R_0 and excess R_{excess} recombination rates, given by

$$R = R_0 + R_{excess} \tag{1.7}$$

From equation (1.7) the carrier lifetime, τ can be ascertained.

$$\tau = \frac{1}{B(n_0 + p_0)} \tag{1.8}$$

A detailed derivation of equation (1.8) can be found in [10]. When the semiconductor is doped, (1.8) can be rewritten for p-type and n-type material respectively.

$$\tau_n = \frac{1}{Bp_0} \approx \frac{1}{BN_A} \tag{1.9}$$

$$\tau_p = \frac{1}{Bn_0} \approx \frac{1}{BN_D} \tag{1.10}$$

Where τ_n is the electron lifetime, and τ_p is the hole lifetime. N_A and N_D are the acceptor and donor concentrations respectively. This then allows for determination of rate equations for different doping types. For p-type material equation (1.5) becomes

$$\frac{d}{dt}\Delta n(t) = -\frac{\Delta n(t)}{\tau_n}. \tag{1.11}$$

For n-type material the rate equation becomes

$$\frac{d}{dt}\Delta p(t) = -\frac{\Delta p(t)}{\tau_p}. \tag{1.12}$$

For a doped semiconductor under low level excitation, the majority carrier concentration is significantly larger than that of the generated carriers. However the concentration of generated carriers will far exceed that of the minority carrier concentration. Solving (1.11) and (1.12) reveals that the majority and minority carrier concentrations both decay exponentially. Since only a small proportion of the majority carriers will recombine, so under such conditions the time taken for this is a great deal larger than the minority carrier lifetime. When the level of excitation is increased the concentration of generated carriers exceeds that of the equilibrium carriers, giving a rate equation of:

$$\frac{d\Delta n(t)}{dt} \approx -B\Delta n^2 \tag{1.13}$$

Using the relationship described by equation (1.13), it can be seen that under these conditions the decay time is not exponential, being quadratic in the excess density carrier if B is independent of Δn [1].

Quantum well type structures are frequently employed in III-nitride LED structures, and will be discussed in more depth in the next chapter. The recombination rate for quantum well (QW) structures can be identified. A quantum well acts to confine carriers to a narrow region. The three-dimensional electron concentration can be approximated by: $\frac{n^{2D}}{L_{QW}}$

Similarly the three-dimensional hole concentration can be approximated by: $\frac{p^{2D}}{L_{QW}}$

Where L_{QW} is the width of the quantum well. The above approximations allow a recombination rate to be ascertained.

$$R = B\frac{n^{2D}}{L_{QW}}\frac{p^{2D}}{L_{QW}} \tag{1.14}$$

From (1.14) it is easy to see that higher carrier concentrations can be achieved by narrowing the well width. This also reduces the dependence of B on n^{2D} and p^{2D} (see footnote). Carrier lifetime is reduced as a result meaning the efficiency of radiative recombination is increased. Of course increasing the efficiency radiative processes is essential for increasing overall device efficiency, and as such the engineering of quantum wells to best do this is discussed later.

[1]The bimolecular radiative recombination coefficient,B,can depend on the strength of the local electric field, especially in quantum wells and quantum dots, which in turn depends on the distribution of the excess densities of electrons and holes

1.2.2 Non-radiative Recombination

Non-radiative recombination occurs when an electron-hole pair recombine to produce a phonon (lattice vibration) or cascade of phonons, meaning that heat is generated. A number of mechanisms cause it to occur, the most common of which involve point defects. These are locations at which free electrons and holes can be captured into one or more localised energy states lying in the forbidden energy gap between the valence and conduction bands. However defects can take a number of forms such as dislocations, intrinsic point defects and impurities. These will be discussed further in the next chapter. Defects make for particularly efficient recombination centres within the bandgap and as such can be detrimental to device performance.

Shockley-Read-Hall (SRH) recombination is the name given to non-radiative recombination via defects. This occurs when a charge carrier is trapped by an energy level (caused by a defect) within the bandgap. An oppositely charged carrier then moves to the same energy level causing the pair to annihilate and release one or more phonons [11] [12].

Whilst this process is generally non-radiative, luminescence has been observed in deep level transitions [13], but this radiation occurs at longer wavelengths which are usually regarded as non-optimal for LED performance.

The rate of non-radiative recombination at a trap of energy E_T is given by:

$$R_{SR} = \frac{p_0\Delta n + n_0\Delta p + \Delta n\Delta p}{(N_T\mu_p\sigma_p)^{-1}(n_0 + n_1 + \Delta n) + (N_T\mu_n\sigma_n)^{-1}(p_0 + p_1 + \Delta p)} \tag{1.15}$$

Where μ_p and μ_n are mobilities of the holes and electrons respectively. σ_p and σ_n are the trap's capture cross sections. If the Fermi energy corresponds to the trap level then n_1 and p_1 are the electron and hole concentrations and are given by:

$$n_1 = n_i exp\left(\frac{E_T - E_{Fi}}{kT}\right) \tag{1.16}$$

$$p_1 = n_i exp\left(\frac{E_{Fi} - E_T}{kT}\right) \tag{1.17}$$

E_{Fi} is the Fermi level.

The rate of Shockley-Read recombination is limited by the rate at which

minority carriers are captured, which leads to the implication that that majority carriers are more likely to be captured. Further, the capture rates of defects lying close to the middle of the band gap tend to be simultaneously high, with the effect that R_{SR} is large and LED efficiency reduced. On the other hand, defects with single energy states lying close to the conduction or valance band edges usually only capture one carrier type efficiently and quickly saturate and thus have little effect on LED efficiency.

1.2.3 Auger Recombination

Auger recombination occurs when the energy from the recombination of an electron and hole, is transferred to a third carrier i.e. a second free electron is excited to a higher lying energy state in the conduction band or a hole is excited into a deeper lying (electron) energy state in the valence band. These carriers will lose their additional energy in the form of phonons until an energetically favourable level is reached near their respective band edges. The Auger recombination rates are given below, with the first having a higher probability of occurring in p-type material and the second in n-type:

$$R_{Auger} = C_p n p^2 \tag{1.18}$$

and

$$R_{Auger} = C_n n^2 p \tag{1.19}$$

Where C_p and C_n are the Auger coefficients. This process requires high carrier concentrations, and so is not observed in low level excitation.

1.3 LED Efficiency

There are many factors which impact on the overall efficiency of an LED, not just recombination.These happen at various stages of photon generation. This section will provide a brief overview of these.

Probably the most intuitive and practical of these is the External Quantum Efficiency (EQE). This describes how efficiently the device converts injected charge carriers into photons which escape the dielectric chip into free space. It

is a product of injection efficiency, Internal Quantum Efficiency (IQE) and light extraction efficiency; i.e.

$$\eta_{EQE} = \eta_{inj}\eta_{IQE}\eta_{ext} \tag{1.20}$$

The injection efficiency(η_{inj}) is used to determine what percentage of injected carriers reach the active region. Some of the current supplied to a device will not recombine at all and will simply pass through the material from electrode to electrode. In conventional pn junction diodes this is termed the diffusion current. QW structures are employed to reduce this effect as they are more effective at trapping carriers and so enhancing radiative recombination.

Carriers which occupy energy levels greater than the confinement energy of the active region can easily escape without recombining. This effect becomes more prominent as injection current is increased because the quasi-Fermi levels also increase in energy and so more carriers have sufficient energy to escape the QWs. At high injection current sometimes there is not sufficient time for recombination and so the well fills and carrier overflow becomes more probable than radiative recombination. To counter this multiple quantum wells are used to recapture lost carriers. Also in GaN-based LEDs a thin layer ($\sim$ 15nm) of wider bandgap semiconductor is usually inserted between the emissive QW or QWs and the p-layer of the pn-junction. This provides an energy barrier that acts to impede diffusion of the more mobile electrons into the p-type layer where they recombine non-radiatively. Such layers are commonly known as electron blocking layers (EBL).

Internal Quantum Efficiency is the term used to describe the proportion of charge carriers which recombine radiatively in the active region to the carriers which recombine radiatively and non-radiatively. IQE is impacted upon by a number of processes, the most obvious being non-radiative recombination. Charge separation arising from piezoelectric polarisation fields can also be detrimental to IQE especially in QWs, as is illustrated in 1-2. As indium content increases (to achieve longer wavelength emission) there is a substantial decrease in IQE. This phenomenon contributes to what is famously known as the "green gap", i.e. the significant reduction in η_{EQE} of green/yellow/orange LEDs compared with blue and red emitting devices.

Extraction Efficiency (η_{ext}) describes the ratio of photons able to escape the

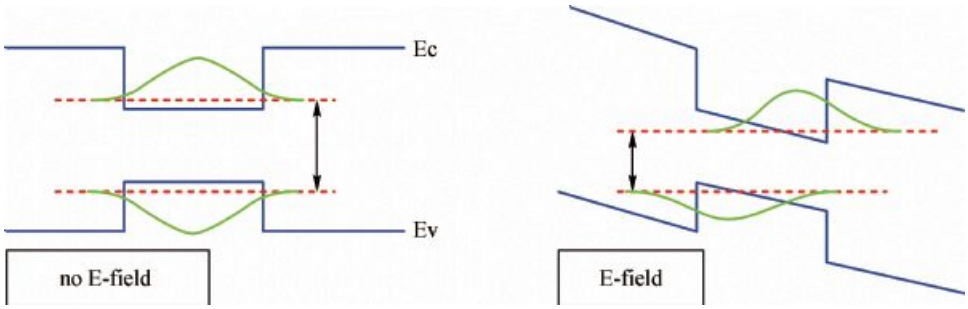

Figure 1-2: Energy band diagram of a quantum well (QW) structure with(right-hand of figure) and without (left-hand of figure) an applied electric field. [14]

device to the number of photons created in the active region [15]. Total internal reflection and photon absorption are the main causes of diminished extraction efficiency, especially in planar devices. Device geometry, surface roughening, etching or growing surface structures and encapsulation can help overcome these problems, to increase η_{ext}.

1.4 III-nitride Semiconductors for Light Emission

Gallium nitride (GaN) is a direct bandgap semiconductor and is ideal for light emitting devices because, via its alloys AlGaN and InGaN, the bandgap can be tuned for emission across the entire visible spectrum and into the ultraviolet. The development of the blue LED paved the way for the first white light LED and thus general lighting applications. White light emission is achieved either by three or four colour mixing (RGB or RGYB), or by coating a blue LED with a colour converting phosphor with the latter generally employed in low cost light bulb replacement units. Whilst the technology is fairly recent, the advantages offered by this material system have long been acknowleged. In 1969, some 30 years after GaN was first synthesised [17], the first crystalline layers were grown epitaxially [2] on sapphire [18]. This material was of very poor quality but interestingly it

[2]Epitaxy comes from the Greek, epi which means "above", and taxis which means "an ordered manner".It is the noun used to describe a crystalline layer grown over another crystalline material, known as the substrate. The former will adopt the crystal structure of the latter even if its planes of atoms have to be stretched (termed tensile strain)or compressed(termed compressive strain)to create the fit.

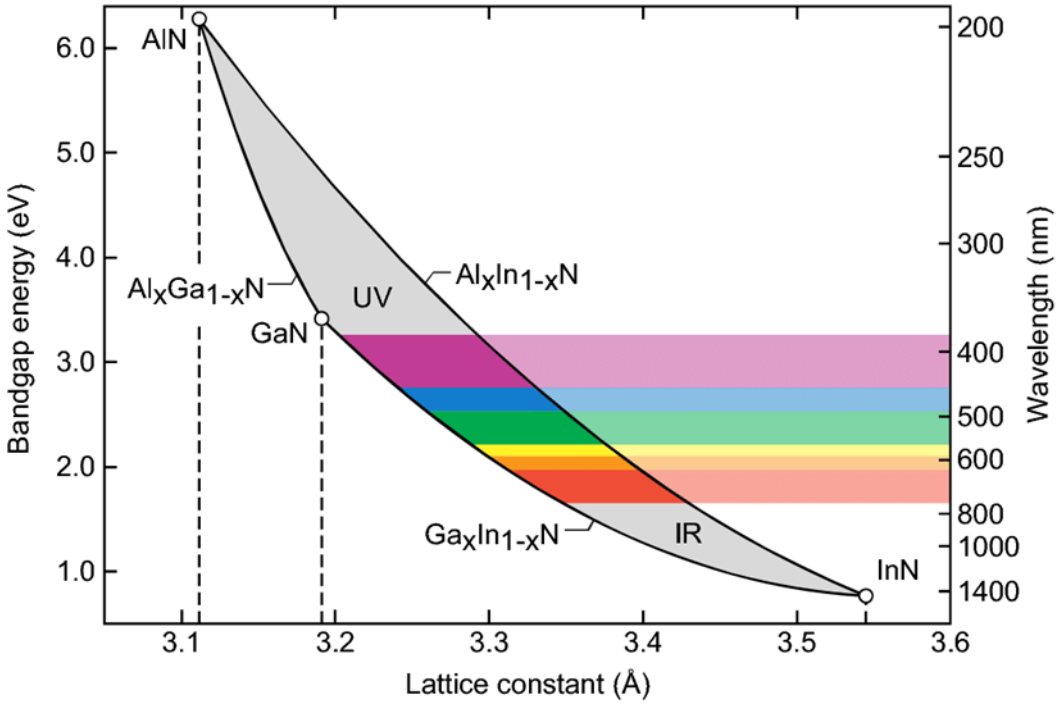

Figure 1-3: Bandgap and corresponding wavelength against lattice constant for the III-nitride material system. Replicated from [16].

was found that the material was inherently n-type. A few years later the first light emitting devices emerged [19] [20] and soon after the first Mg doping was reported [21]. However the poor quality of the material and inconsistent results hindered progress. The development of molecular beam epitaxy (MBE) and metal organic chemical vapour deposition (MOCVD) led to significant improvements in crystalline quality [22] [23].

As its name suggests MBE is the process in which thin-layers are deposited by beams of gaseous elements directed towards the substrate where they condense. This process does not use carrier gases and requires an ultra high vacuum. MOCVD employs the use of chemical reactions for deposition, in contrast to MBE which directly deposits material. These reactions occur at high temperature and usually under low pressure, the value of which is dependent on the material grown and will impact upon the crystalline quality. MOCVD will be discussed further in 1.4.2.

The next significant development came in the late 1980s and 1990s and was the ability to p-dope the material. This was especially challenging due to the

inherently n-type nature of GaN with p-type layers tending to be highly resistive and insulating. Substantial effort saw the realisation of Mg-doped layers resulting in increased luminescence [24] [25]. Progress accelerated and saw the realisation of commercial blue and white LEDs.

1.4.1 Structure of III-Nitride Semiconductors

Alloys in the $Al_xIn_yGa_{1-x-y}N$ system can have either a Wurtzite or zinc-blende crystal structure, however the former is thermodynamically the more stable. When describing a Wurtzite crystal a number of parameters need to be defined; the atomic separation within a plane is termed a and the periodicity of the atoms,termed c. These are shown below in Figure 1-4.

GaN lacks a suitable substrate so is typically grown on sapphire, although much work is now being done using silicon substrates [26]. Only sapphire substrates are considered here. The large lattice mismatch between GaN and sapphire causes the material to become strained, and also introduces dislocations. GaN and sapphire also have different thermal expansion coefficients, so as the epitaxy cools post growth, dislocations and cracking can occur [27]. Figure 1-3 shows that a lattice mismatch also exists between GaN and InN, so this too introduces strain into the epitaxy.

GaN in its hexagonal crystalline form experiences a spontaneous polarisation which arises because the Wurtzite crystal is intrinsically asymmetrical. Light emitting devices are typically grown in the c-plane direction (see Figure 1-4), meaning that each surface of layer has a polarisation charge resulting in an internal electric field directed upwards or downwards along the c-axis depending on the sum of the spontaneous and piezoelectric polarisation. Added to this spontaneous polarisation, a piezoelectric polarisation occurs as a result of the lattice mismatch strain with the substrate, and is either positive or negative depending on the direction of growth and whether the semiconductor is experiencing tensile or compressive strain.

If QWs are present, internal electric field causes charge separation by forcing electrons and holes to opposite sides of the QW, which causes poor electron-hole wavefunction overlap, an essential requirement of recombination. This is known as the quantum confined Stark effect (QCSE) and is particularly marked for wide

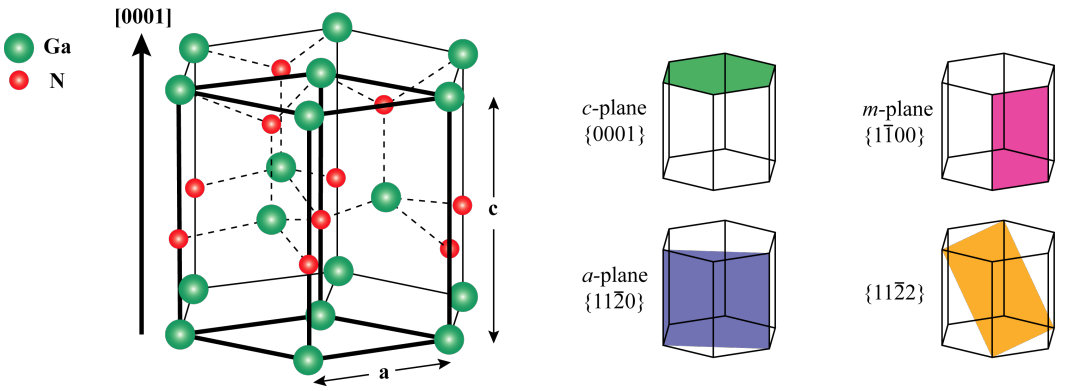

Figure 1-4: Structure of Wurtzite GaN and directions of each plane. Lattice constants for GaN are $a = 3.186$ Åand $c = 5.186$ Å [28]. Replicated from [29].

QWs with high In contents, and therefore is detrimental to longer wavelength emitters, for example green-to-orange LEDs. The QCSE describes how the emission spectrum (or absorption spectrum) of a QW is effected by the presence of an external electric field. When no external electric field is acting on a QW then charge carriers can occupy certain discrete energies. However if an electric field is applied this causes electrons and holes to move to lower and higher energies respectively, resulting in a reduction in allowed emission frequencies. The recombination efficiency is hindered due to electrons and holes moving to opposite sides of the QW i.e. reducing the wavefunction overlap.

1.4.2 Growth of III-Nitrides

III-nitride semiconductors can be grown using a number of methods, including MBE, MOCVD [30] [31] and hydride vapour phase epitaxy (HVPE). MOCVD is most frequently used to grow LEDs structures. The substrate (e.g. sapphire) is placed in the reactor on a heated stage. Precursor chemicals trimethylindium(TMI) and trimethylgallium (TMG) and ammonia (NH_3) are used as sources for In, Ga and N respectively and are carried in hydrogen or nitrogen gas.

Layers are doped by including silane and bis(cyclopentadienyl)magnesium in the aforementioned precursor chemical mixture to achieve n-type doping (by Si) or p-type doping (by Mg). The gaseous molecules decompose to create a local atmosphere of In, Ga, Al and N over the substrate from where atoms are deposited to evolve the epitaxial layer. These atoms may either adhere directly

on the surface of the latter, as in the case of N, or diffuse across the surface to reach the edge of a laterally expanding added plane of the crystalline alloy. The substrate temperature is controlled throughout growth depending on alloy composition. The flow rate of the chemicals can be varied in order to achieve abrupt interfaces. These allow for the growth of doped layered structures as required in pn junction diodes.

1.5 The Green Gap

Although called the"green gap", it actually covers the green, yellow and orange wavelength regions of the visible spectrum. Specifically it describes a wavelength region between 520nm and 635nm , in which LEDs do not reach a satisfactory external quantum efficiency. A comprehensive understanding of the structural and material issues which affect these long wavelength InGaN LEDs is necessary in order to realise their potential. Optimum performance for RGB display applications requires devices emitting at 540nm and 622nm, however the biggest drive comes from the desire to produce high quality, high efficiency white light systems. Currently white light LEDs make use of a blue LED covered in a phosphor. Whilst many advances have been made in the development of these phosphors, this system suffers from a number of issues. White light rendition by mixing three, or even four, separate colours is known to improve not only the colour rendering index but also the luminous efficacy [32], [33]. The green gap problem arises from a number of issues which include reduced crystal quality due to indium segregation and lower growth temperature [34] [35], the larger lattice mismatch and consequent stronger quantum confined Stark effect (QCSE) in InGaN/GaN multiple quantum wells (MQWs) with the higher InN mole fraction needed to shift the emission to longer wavelengths [36]. A further discussion of this and approaches to overcoming it can be found in 2.1.2.

It should be noted that emission in the ultraviolet region, which uses AlGaN, is also inhibited in a similar way. Higher aluminium contents are used to shorten the emission wavelength but as the Al content increases efficiency drops off rapidly. There is an in intense interest in realising efficient emission at such wavelengths (100nm - 400nm) for germicidal and curing applications.

1.6 Aims and Objectives

The research described in this thesis aims to characterise the inefficient nature of LEDs emitting in the long wavelength visible region of the spectrum. The aim of the research is to investigate the contributions of non-optimum GaN/InGaN semicondutor layers, including defect related effects, to degrading the efficiency of LEDs.

The work also aims to confirm the viability of Al:ZnO (AZO) as an alternative to Indium Tin Oxide (ITO) for use as a current spreading layer, as well as addressing some of the practical engineering questions related to that.

Finally the research looks at the use of alternative structures as a potential for realising high efficiency UV emission by omission of the problematic p-layer.

This chapter is adapted from the author's confirmation report [37].

Chapter 2

Literature Review

This chapter will discuss the literature surrounding the key challenges facing AlGaN/InGaN/GaN based LEDs, especially those emitting in the green - orange and UV regions (non-standard wavelengths). There are a number of approaches which can be used to improve the efficiencies of LEDs operating at non-standard wavelengths. These could involve structural cures such as improved chip geometry, the growth or etching of nanostructures, surface roughening or surface microstructures. Such cures aim to aid light extraction and in the case of forming nanostructures alleviate some of the strain induced effects. Improved epitaxial structure design could increase radiative recombination rates (thus increasing IQE). This could include the use of prelayers, electron blocking layers (EBL)and optimisation of the active region. Improved contact technology and fabrication techniques (e.g. reduced etch damage) would benefit injection efficiency.

Meeting the challenges posed by the drop in efficiency outside the blue region requires steps to be taken at all stages of device design and production. A vast body of literature exists on such topics and therefore a brief overview is presented with the focus being increased IQE, process enhancement and optimisation of the transparent conducting layer.

2.1 Efficiency issues in III-Nitride LEDs

This section aims to put into context the efficiency challenges faced by III-nitride LEDs.

2.1.1 Efficiency Droop

Efficiency droop is a significant issue in InGaN/GaN LEDs. It is a phenomenon in which a decrease in IQE is observed as injection current increases. Droop in InGaN LEDs is observed at all wavelengths however it does tend to increase with increasing emission wavelength. It is also observed in arsenide/phosphide based devices which operate in the red - yellow part of the visible spectrum, and is known to be a result of self-heating. So when it was seen in nitride based devices it was originally thought to have the same origin. However when pulsed measurements were performed (in order to prevent the device from heating), droop still occurred. Nakamura suggested that indium (In) clusters in the QWs were the cause [38]. Light and dark areas in the QWs were seen using a transmission electron microscope. X-ray diffraction experiments determined that these corresponded to In-rich and In-poor areas respectively. It was proposed that these In-rich areas were defect-free and thus would trap electrons and holes, giving rise to bright emission. Then as current increased these regions would become saturated and so charge carriers would be pushed to defect rich areas which would lead to non-radiative processes dominating. Therefore, this saturation was the proposed origin of droop. A number of groups carefully measured the variation of In composition in InGaN Qws using low-voltage imaging. No significant In clustering was observed and therefore it can be concluded that they are not critical for substantial light emission [39], [40].

A number of papers published around 2007 offered different explanations, including Auger recombination [41], carrier leakage [42], quantum well width [43] and Fermi level dependent non-radiative recombination via defect states [44]. Of these, Auger recombination has drawn the most attention. It was Lumileds who brought this interpretation into the spotlight [41]. Photoluminescence was measured over a range of intensities and it was shown that its variation fitted well with the equation describing Auger recombination. This was further reinforced by the theoretical work of Van de Walle et al which suggested that an indirect, phonon-assisted Auger process could be the cause [45]. In 2013 teams from UCSB and CNRS-Ecole Polytechnique reported that they had directly measured Auger electrons using electron emission spectroscopy from an InGaN/GaN LED under forward bias [46]. However many still argue that Auger recombination does not account for the efficiency loss seen in many LEDs and that carrier

leakage mechanisms must also be included [47]. Existing LED structures are quite complex, their fabrication and characterisation have many variables therefore reaching definite conclusions on the origin of droop remains both challenging and controversial. It is also probable that different droop mechanisms dominate in different structure types.

2.1.2 The Green Gap

Perhaps the greatest challenge in realising high efficiency green - orange LEDs is the rapid decrease in IQE as the In composition (and thus wavelength) in the QWs increases.

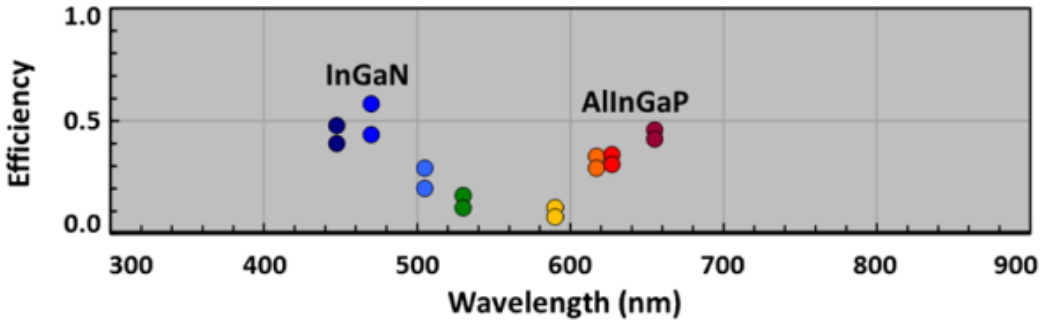

Figure 2-1: Power conversion efficiency with wavelength [9].

As is mentioned in section 1.5 a number of factors contribute to this. These include difficulty in growing active regions arising from the required reduced growth temperatures [48] and the limited solubility of In [49]. Large lattice mismatch between not only the material and substrate but also between GaN and InN [50] and the lower surface mobility of In atoms compared with Ga on the growing epitaxial surface can give rise to high defect densities in the material. Built-in spontaneous and piezoelectric polarisation fields [51], the origins of which are noted in section 1.4.1, can have a significant impact on the IQE. They are responsible for the QCSE, the effect of which is that there is reduced overlap in the electron and hole wavefunctions, which in turn results in a lower matrix element for radiative recombination. Both polarisation fields lead to charge separation effects which affect the dynamics of carriers in the QWs [52]. These also have the effect of broadening EL-spectra [53].

A number of actions have been proposed to counter the issues detailed above. These include modification of the active region, surface structures, the inclusion of underlayers (i.e.layers beneath the emissive MQW region in the LED epitaxial structure) for possible strain relaxation, advantageous electric field distribution or for improving the supply of injected electrons. The use of cubic GaN has drawn interest as a possible green gap solution, although currently is challenging to grow. It removes the issue of internal electric fields and thus the QCSE so increases the radiative recombination efficiency. Additionally it has a smaller bandgap than hexagonal GaN which results in less indium being required to achieve longer wavelengths [54].

2.1.3 Defects and their effects

Gallium nitride heteroepitaxy, inherently has a high density of defects, arising mainly from a lack of suitable substrates with the effect that the substrates employed have rather different lattice parameters resulting in the epitaxy becoming strained and forming defects. Many methods of reducing these issues result in more complex growth processes. However there have been many recent developments on the growth of device structures on bulk GaN substrates [55]. Lattice matched GaN substrates have seen considerable improvement and are now commercially available. The use of such substrates negates the negative results of growth on foreign substrates and an improvement in device performance has been demonstrated [56].

Abrupt extended changes within the crystal are known as threading dislocations(TDs). They arise because of vacancies or misalignments of atoms and cause the interatomic bonds to become distorted or break, which in turn causes distortions in the crystal lattice. Generally speaking, TDs found in GaN are comprised of components of both edge and screw dislocations. The probability of carrier tunnelling is thought to increase around TDs since leakage current significantly increases as TD density increases. A decrease in luminescence due to current leakage is observed. However carriers are still more likely to move towards QWs, the latter effect being offset by the greater thermal energy needed for carriers to escape the deeper wells. Reduced carrier mobility, due to electron scattering, can be attributed to the presence of such defects in the material [57].

Point Defects can be generalised into three categories; vacancies, interstitial atoms and substitutional atoms or combinations of these different sorts. A vacancy is an unoccupied site in the crystal lattice. Interstitial atoms are atoms which occupy a site between regular sites, however such atoms must maintain sufficiently low energies in order to remain there. Substitutional atoms are impurities which occupy regular sites within the lattice. Such defects can act as carrier traps.

Grain boundaries are the interfaces between regions of different crystallographic orientation and the bulk material. It is thought that these form potential barriers, thus limiting carrier transport [58]. Dislocations occur at these grain boundaries, in fact defining their position.

Inversion domains are regions which are opposite in polarity to the bulk semiconductor. III-nitride material is typically strained, so when inversion domains are present, the direction of the piezoelectric polarisation field will be reversed [59]. Stacking faults are disruptions to the sequence of the stacked lattice. In the case of Wurtizite structures these can be subdivided into two categories; basal stacking faults (BSF) and prismatic stacking faults (PSF). The former tends to occur in polar, c-plane GaN as this requires the least amount of energy.

As their name implies, nanopipes are pipe like structures, aligned in the direction of crystal growth and are related to dislocations and oxygen impurities [60].

Defects are known to introduce strain in III-nitride films which results in additional polarisation which can negatively impact radiative recombination. Defects can also introduce energy levels to the forbidden region which may then act to scatter carriers or as non-radiative recombination centres thus decreasing efficiency. They can, however, result in radiative recombination often observed as yellow band emission in n-type GaN [61]. InGaN based LEDs frequently possess high densities of threading defects, the origins of which are described above, and it has been demonstrated that leakage current increases exponentially as threading dislocation increases [62]. It has been reported that current-voltage measurements on InGaN/GaN LEDs grown on sapphire show that tunnelling mechanisms can be dominant over a large bias range [63]. However, this is not the case for devices grown on bulk GaN substrates as the material tends to contain fewer dislocations [64]. These results indicate that defects have a significant impact on current paths through the active part of the LED, namely the QWs.

GaN grown on sapphire has a relatively high concentration of dislocations due to the large lattice mismatch. Clearly the growth of low defect density material is a likely requirement for the development of devices with high IQE. A detailed review of the effect of defects can be found in review by Reshchikov [65].

2.1.4 Epitaxial layer engineering

Quantum well structures

A quantum well (QW) is a thin layer of semiconductor material which acts to confine charge carriers. Such regions are sandwiches between layers of wider bandgap material which act as energy barriers, preventing carrier escape. A number of different approaches have been used to improve QW efficiency.

Staggered QW structures are comprised of so called sub-layers which have different In contents and are sandwiched between barrier layers. They have been shown to enhance spontaneous emission and thus radiative recombination rates resulting in increased optical output power [66], [67] [68], [69], [70], [71], [72]. This is attributed to the increased electron and hole wavefunction overlap and improved carrier confinement [67], [70], [68]. Improved overlap comes from spreading the wavefunction of the lighter effective mass particle (the electron) towards the centre of the QW. However the centroid hole wavefunction remains unchanged [67]: Figure 2-2. The abruptness of sub-layer interfaces has been shown not to effect the spontaneous emission and therefore allows for the use of graded growth temperature, making manufacturing practical [73].

Graded QWs (GQW) are structures in which the In composition is linearly graded or well thickness is increased along the direction of growth. It has been reported that these both cause a suppression of the quantum confined stark effect (QCSE)(see discussion in previous chapter, Section 1.4.1) and Auger recombination. [74]. In addition, those with increasing well thickness demonstrate significantly improved hole distribution [75], that is QWs are more uniformly populated, as opposed to the default where most holes are in one QW closest to the p-type side. These effects result in decreased efficiency droop, making this technique promising for all InGaN based light emitters, not just those in the green gap [74] [75] [76] [77].

Chirped MQW LEDs contain an active layer comprising of thick QW with

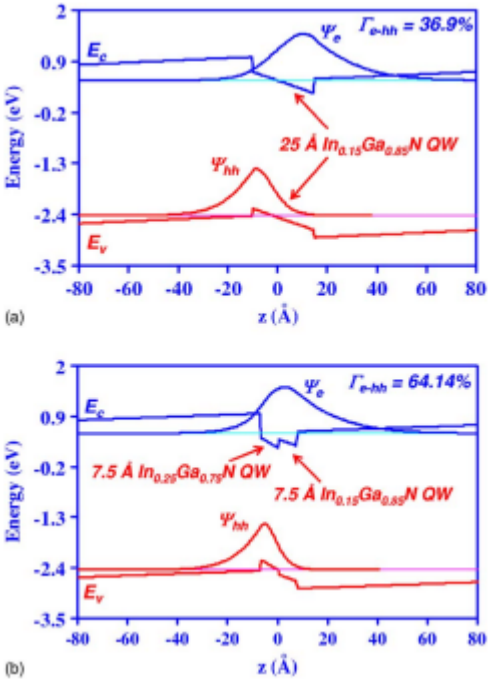

Figure 2-2: Figure shows (a) A conventional QW structure (b) Staggered QW structure [67].

low In content close to the p-side layer and thin, high In content QWs on the n-side. [78] [79] Such structures have exhibited improved carrier injection into active region and therefore an increase in radiative recombination.

Electron-hole overlap can be increased by inserting an ulta thin InN or AlGaN layer (δ layer) in the InGaN QW [80]. In fact the overlap increases with increasing wavelength and the insertion of this layer can increase the emission wavelength as the average well depth is increased [81] [80].

Strain compensated QWs [82] InGaN/GaN substrates eliminate the issues of substrate-epitaxy lattice mismatch and thus cause a reduction in strain leading to a reduction in internal polarization fields. However a mismatch still exists between GaN and InN giving rise to polarization.

Lumileds and several others have proposed the use of thick QWs, (9nm and 13nm) [83], which would be less susceptible to Auger recombination due to the reduction of carrier density in the active region.

Usually "thin" quantum wells are adopted to improve the quality of the material and prevent severe reduction in the overlap integral arising from the QCSE.

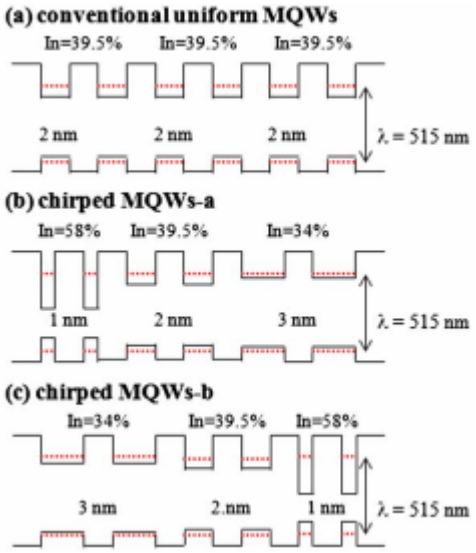

Figure 2-3: Figure shows (a) A conventional QW structure (b) Chirped QW(c) Chirped QW of opposite polarity [78].

The trade off comes when volume averaged carrier density increases which will make Auger recombination ever more likely. The inclusion of a shallow QW before the active QW has been shown to increase efficiency by reducing the lattice strain in the active region [84].

Quantum dot structures

Quantum dots (QD) have been proposed as an alternative active layer to quantum well structures as they have shown increased efficiency in the green gap region [85]. In rich regions in InGaN active region layers exhibit localised increases in radiative recombination due to the formation of potential minima. Both self-assembled methods and MOCVD have been used to create QD active layers. These structures have shown a reduction in the strain induced piezoelectric polarisation [86]. Wavelength shifts are observed as injection current increases because of the QCSE, so clearly growth optimisation is required before the potential of QD active layers is realised.

Blocking layers

Many InGaN based LED structures include an AlGaN electron blocking layer (EBL) as a means of improving carrier confinement, however such layers, whilst reducing electron overflow into the p-layer, can also inhibit hole injection into the active region [87]. Whilst EQE does improve with the inclusion of an EBL at moderate current density, as this is increased the EQE suffers due the reduction in hole injection efficiency [88].

The use of an InAlN EBL has been shown to suppress droop and improve emission intensity [89] [90] [91]. Such results are indictive of the need for improved carrier confinement to the active multiple quantum well (MQW) layers and reduced leakage for realising high power high efficiency green gap region LEDs [90] [91]. High In contents in the active region make green gap region emitters more vulnerable to thermal damage, therefore the lower growth temperature needed for InAlN EBLs may facilitate increased quantum efficiency [91]. Additionally InAlN is preferable as it offers reduced lattice mismatch compared to AlGaN.

Improving light extraction

One of the most fundamental hindrances to light extraction is that InGaN has a high refractive index (n = 2.4). However other factors also impact the optical properties of LEDs these include impurity and free carrier absorption, metal contacts, active layer reabsorption and low bandgap layers [83]. Owing to its high refractive index a significant proportion of the light generated within the device remains trapped within it by total internal reflection. Naturally this leads to the development of methods for increased extraction of this light. This can done in a number of ways; enhanced chip shaping, growing or etching nano structures, surface roughening, employing the use of surface structures and improved transparent current spreading layers (these are layers which ensure that the injected current is distributed as uniformly as possible across the active area of the device (current spreading) and are optically transparent to allow for light extraction).

Chip structures and geometry

A number of chip structures can be employed. Conventional structures have the n-layer grown first, on top of the substrate. The active layer lies on top of this, and the p-layer above that with or without an intervening electron blocking layer. The p-layer and active region must be etched in order to access the n-layer for contact deposition.

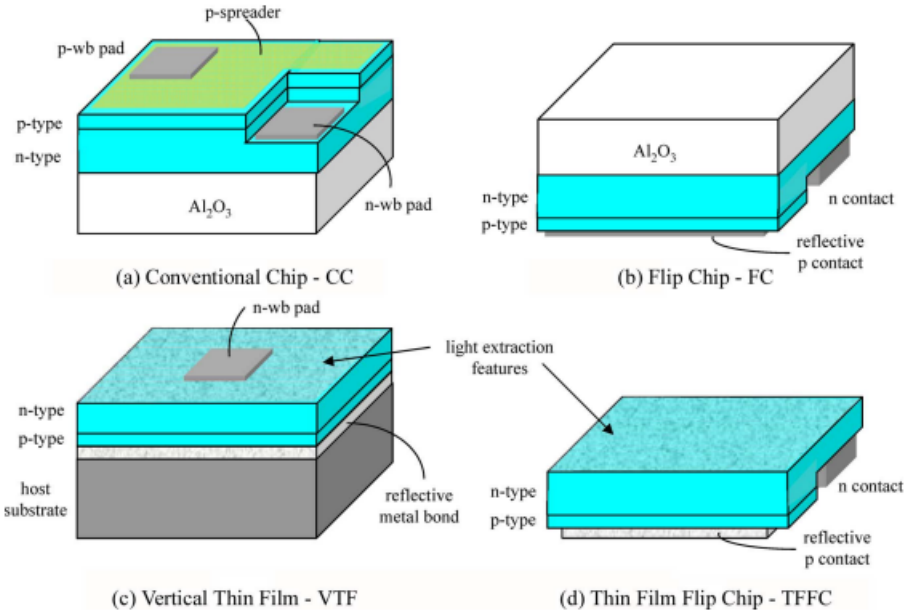

Figure 2-4: Different device structures [83].

P-side down structures

P-side-down LED structures can be grouped into two distinct types; the first being conventional [0001] oriented pn-LED's, in which final stage of growth is the p-GaN layer which is later wafer bonded to a carrier substrate in order to create a vertical LED structure with the lower contact acting as a mirror. The second type is a simple heterostructure which consists of the p-GaN layer grown first and the n-InGaN layer grown on top, oriented along [0001]. The latter is not favoured owing to the tendency for the Mg acceptors to become de-activated during epitaxial growth.

Both of these p-side-down structures bring their own advantages to device performance; the vertical LEDs have a reflective p-contact which increases light

extraction, and the carrier substrate improves heat extraction at high current operation. The devices whereby the p-GaN layer is grown first have shown improved performance due to a reduction in the hole injection barrier. In addition, an enhancement in the electron barrier has been reported, negating the need for an electron blocking layer [92] [93]. Novel low temperature growth has been reported by Meaglow [94]. Such a technique avoids acceptor deactivation and could be used in developing LEDs with this structure.

Chip geometry

It has been shown that the shape of a device has a significant impact on the light extraction efficiency [95] [96]. Increased light extraction is seen in non-conventional geometries when compared with conventional rectangular devices [95] [97] because of total internal reflection on neighbouring sidewalls. Hexagonal chip geometries not only show greater light extraction but also make the most efficient and practical use of the epitaxy. Whilst the optimum LED shape is recognised as spherical with a point-like active region [10], these and similar "dome-like" structures are not practical and or cost-effective. The rectangular/square chip shape is the most practical geometry when fabricating on a wafer-scale, with such a shape allowing for individual devices to be easily cut from the wafer. The practicalities of device fabrication and manufacturing processes of packaged devices are critical in determining the widespread adoption of a particular technology.

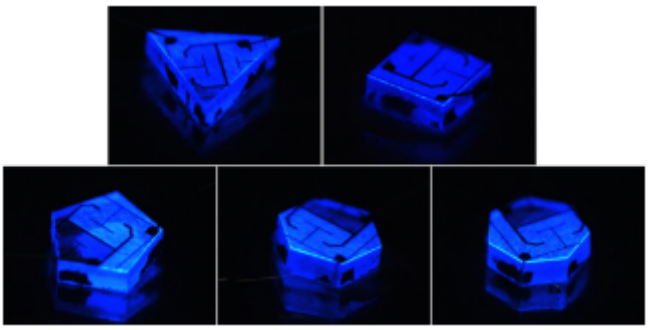

Figure 2-5: Different chip geometries [95]. Devices shown have an emission area of $0.57mm^2$.

Nanorod LEDs

Devices which incorporate nanorod arrays offer several advantages over the traditional planar LEDs: (i) The structure gives rise to lateral strain relaxation which, in narrow nanorods(¡ 250nm diameter)can extend virtually all the way through the nanorod [98], with the effect of reducing the QCSE and increasing IQE. (ii) The light extraction efficiency is improved via the moth-eye effect [99] and emission pattern control made possible for an ordered nanorod array which acts as a diffraction grating, coupling trapped guided modes in the planar regions to radiation modes. (iii) Light extraction efficiency is improved due to increased surface area and (iv) nanorods can potentially reduce the number of dislocations [100].

Surface Patterning

The surface of an LED plays a critical role in whether light is emitted or internally reflected. These can be divided into two distinct categories; large facets which reduce the trapping of light and sub-wavelength texturing which increases light extraction (see previous section). Surface roughening via wet chemical etching (e.g.KOH etch) is known to increase light extraction [101]. Nano roughening of the p-GaN surface has been shown to increasing efficiency and also significantly reduce series resistance [102]. The transparent contact layer can also be roughened [103] to increase light extraction.

Graded refractive index (GRIN) LEDs employ microstructures grown on the top surface of the device. The microstructures are comprised of a number of layers of material with different refractive indices. Devices which include such structure offer the possibility of controlling the far-field emission pattern and enhancing light extraction [104], making them useful for etendue-limited applications such as projection systems and automotive headlights [105].

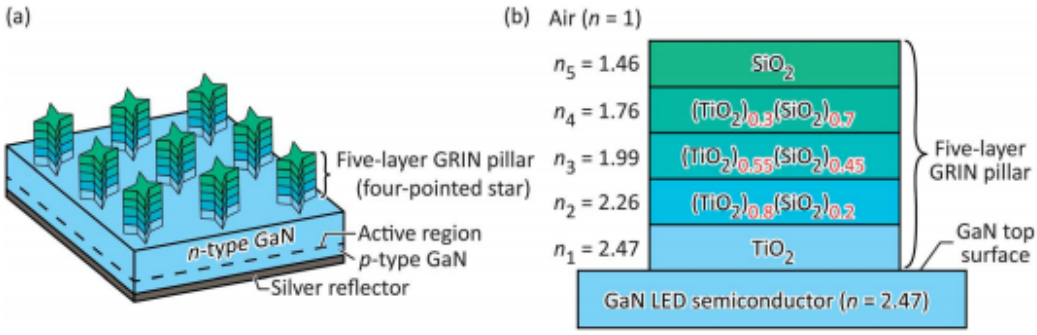

Figure 2-6: P-side down LED structures showing graded refractive index (GRIN) microstructures fabricated on the n-GaN. These microstructures are typically several microns in diameter. See [106].

2.1.5 Non-polar and Semi-polar GaN

GaN/InGaN based LEDs grown on non-polar or semi-polar orientations have demonstrated or are predicted to demonstrate, increased IQE, improved In incorporation into the QWs, reduced or eliminated internal polarisation fields and reduced efficiency droop, as thicker QWs can be used (although this does assume that Auger recombination is the dominant cause of droop) [107]. However, such systems currently suffer from poor crystalline quality, small substrate area, as well as high cost. As noted earlier(see 2.1.3), the most straight forward way to grow device structures is on bulk GaN substrates.

2.2 Fabrication Considerations for GaN based LEDs

The method for the fabrication of InGaN based LEDs in this work is described in the next chapter. Optimised fabrication processes are essential in ensuring maximum efficiency and reliability are achieved.

2.2.1 Etch damage

GaN/InGaN based LEDs usually adopt a "mesa diode" structure (see 3-2. Mesas are typically dry etched using a chlorine based inductively coupled plasma (Cl_2

or BCl_3). This process provides good surface morphology, process control and stable etch rates. However the plasma can damage the semiconductor, either by leaving the surface nitrogen depleted or by leaving dangling gallium bonds which then bond with oxygen. Both the N vacancies and the O impurities result in the formation of shallow defect levels which may be detrimental to device performance and reliability. It is possible to use a N_2 plasma treatment to recover the surface of n-type material [108]. P-type material can also be recovered by removing the surface oxide layer (caused from the Cl_2/Ar O_2 etch) using a buffered oxide etch [109], a step which could be critical in avoiding device failure. No steps to remove etch damage were undertaken in this work.

2.2.2 The formation of Ohmic contacts with GaN based materials

Here the mechanisms for forming ohmic contacts with GaN based materials are discussed. A metal/semiconductor interface with no potential barrier for carrier tunnelling is an Ohmic contact [110]. They provide the essential link between the device and the external circuitry, making their optimisation critical [111].

The total resistance of this interface is known as the contact resistance (see 3). From this, the more useful, specific contact resistance,ρ_c, can be determined [112]. It is one of the fundamental parameters determined when characterising any semiconductor device. Poor contacts are detrimental to efficiency and can result in device failure.

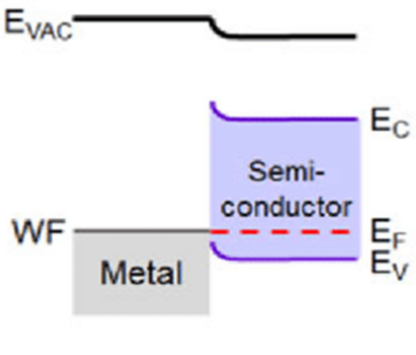

Figure 2-7: Energy level at metal/semiconductor interface for an Ohmic contact [113].

Due to the wide bandgap of GaN, the formation of Ohmic contacts is difficult [114]. Typically Ti/Al/Ni/Au is used to form such contacts on n-type GaN, and Ni/Au [115] on p-type. The specific contact resistance is dependent on the metal/semiconductor Schottky barrier height Φ_B and the semiconductor's doping concentration,N_D [116].

Interface carrier transport mechanisms are dependent on N_D. For lightly doped ($N_D < 1 \times 10^{17} cm^{-3}$), thermionic emission is the dominant mechanism. In this instance ρ_c does not depend on N_D, as carriers require thermal excitation over the barrier due to the large space charge region . In material with doping in the region of $1 \times 10^{17} < N_D < 1 \times 10^{19} cm^{-3}$, the dominant transport mechanism is thermionic field emission. This means that carriers require thermal excitation to a level where tunnelling is permissible. In heavily doped semiconductors ($N_D > 1 \times 10^{19} cm^{-3}$), carrier transport is dominated by field emission. Here electrons can tunnel through the interface due to the small barrier height, so Schottky barrier and doping concentration have significant influence on the specific contact resistance [114].

Temperature is the determining factor for transport mechanisms in instances when the carrier concentration and barrier height are static. At low temperature the primary mechanism is field emission. At intermediate temperatures thermionic field emission dominates. Thermionic emission is responsible for electron transport at high temperature [111].

These allow for the deduction of suitable materials for good Ohmic contact formation. For n-type GaN Ti and Al provide a low Schottky barrier height [117] [118] [119]. The consensus is that TiN (a metallic conductor) is formed at the interface upon annealing. The GaN at the interface becomes nitrogen deficient and develops a high free electron concentration and gives a suitable quasi-ohmic contact. P-type GaN is more challenging due to the difficulty in obtaining low barrier heights [120]. However it is found that metals with a high work function Ni, Au, Pt and Pd are the most suitable candidates [121]. The table below gives the work functions of metals commonly used to form contacts on GaN.

Metal	Work Function (eV)
Ag	4.26 - 4.74
Al	4.06 - 4.26
Au	5.10 - 5.47
Ni	5.04 - 5.35
Pd	5.22 - 5.60
Pt	5.12 - 5.90
Ti	4.33

Ohmic contacts on p-type GaN

Work functions of metals are generally in the range of 4-5eV and the bandgap of GaN is 3.4eV. Thus making obtaining a small Schottky barrier at the metal/p-GaN interface inherently challenging [120]. The p-type doping of GaN has been a long standing focus of research [21] [25]. Whilst many advances have been made, many problems still exist. One such problem, which affects the specific contact resistance, is the concentration of free holes. The free hole concentration in p-GaN is an order of magnitude (or more) lower than the doping concentration. It is possible to, at least to some degree, remedy these issues by using metal alloys and by optimising the annealing conditions.

Current spreading layer

All devices discussed in this work were grown on insulating sapphire substrates. This means that current mostly flows laterally within the device. This structure requires current to be injected via an electrode on top of the p-GaN layer. To counteract the impact this will have on light extraction, a current spreading layer is employed. It is a transparent conducting film that distributes current to areas not covered by the electrode. Such layers increase light extraction and ensure uniform emission. Poor carrier distribution in the active layer is thought to arise due to low hole mobility, causing an increase in current density at QWs on the p-side layer of the junction, and thus resulting in a reduction in the IQE at high current density [122]. Theoretical studies show that improved current spreading can be used to induce a more uniform distribution of carriers into these active layers and therefore decrease efficiency droop at high current density [123].

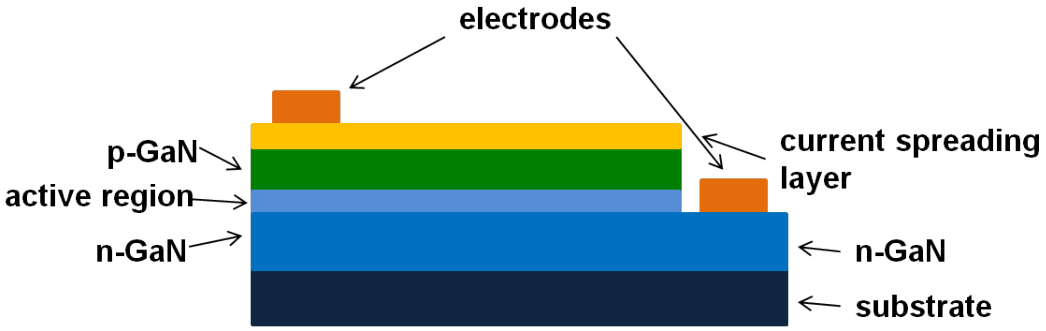

Figure 2-8: Simplified LED structure.

There are various approaches when trying to improve such layers and are discussed in this section. The use of thin metal layers underneath a thick transparent conducting oxide (TCO) is explored experimentally in later chapters.

Thin Ni/Au is the most common current spreading layer employed in GaN based light emitters. It is annealed in O_2 post deposition causing oxidisation, resulting in the Ni being converted to NiO, which is itself a p-type semiconductor.

Improved light extraction due to reduced absorption of emitted light, by use of a mesh transparent contact layer has been demonstrated [124].

Graphene is a promising material in many fields, and has been successfully used as a transparent contact layer in III-nitride based LEDs. Such devices show improved optical power and low contact resistance [125].

Indium Tin Oxide (ITO) is commonly used as an alternative to Ni/Au due to it's enhanced transparency and better thermal stability. Improved Ohmic behaviour (compared to Ni/Au) has been demonstrated for contacts employing an interlayer/ITO system. A number of metal interlayers have been investigated, including Ni,Ni/Au and Ag [126]. The motivation for the inclusion of Ni is the formation of interfacial NiO and thus improved specific contact resistance [127]. However other interlayers exhibit encouraging behaviour. Ag/ITO contacts have been demonstrated to have a specific contact resistance comparable with Ni/Au, but having an increased transmittance [128]. Therefore such devices will have an increased light output. The improved electrical characteristics are attributed to the formation of Ag-Ga, which produces Ga vacancies underneath the contacts, thus increasing the carrier concentration at the surface [129]. Al doped ZnO (AZO) shows promise as a replacement for ITO, with equal or even improved

transmittance however higher sheet resistance. Ni and NiO interlayers with AZO have been investigated and shown an increased light output for UV GaN LEDs compared to those using Ni/Au [130].

Clearly the transparent contact layer makes a vital contribution to the overall efficiency of the device so the optimisation of this is essential in realising efficient green gap emitting LEDs.

2.3 Summary

Overcoming the issues faced by green gap region InGaN based devices can be done in a number of ways such as improving IQE, lowering droop, increasing light extraction. However optimisation of the metal/semiconductor contacts is also of critical importance. The realisation of these are key to the development of the most efficient white light emitting devices.

This chapter is adapted from the author's confirmation report [37].

Chapter 3

Experimental Methods

This chapter aims to introduce the reader to the numerous techniques used throughout this work to fabricate, characterise and analyse the LEDs in this work. With the exception of the devices discussed in chapter 7, all devices were fabricated, characterised and analysed in-house. The samples in chapter 4 were generously provided by IQE plc. The transparent contact layers discussed in chapter 5 and chapter 6 were kindly deposited by Sarah Thornley at Plasma Quest Ltd, as part of the INREP project. INREP was funded by the European Union via the Horizon 2020 research and innovation programme (grant agreement No 641864).

3.1 Device fabrication

This section summarises the techniques used to fabricate the LEDs presented in this work. A diagram of the 'standard' fabrication [131] is included, with any deviations from this procedure detailed below. The devices discussed in Chapter 7 fabricated at Imperial College London and a description of this included at the beginning of that chapter.

3.1.1 Etch mask

In order to etch device geometries in to a wafer an etch mask must first be created. This acts to expose certain areas whilst protecting others (in this case the p-GaN layer). The mask material itself is chosen so that it will be resistant

to the GaN etch. This can either be 400 nm of either SiO_2 or SiN_x deposited by plasma enhanced chemical vapour deposition (PECVD). However, hydrogen silsesquioxane (HSQ) has successfully been used instead, it is an inorganic, low viscosity, essentially liquid, glass that has the advantage of being deposited by spin coating, making processing much quicker. Hard glassy layers of essentially SiO_2 can be formed by subsequent curing using heat or ultra-violet light. SiO_2 or SiN_x layers can be readily removed in hydrofluoric acid (HF) based wet etches which do not attack III-nitride semiconductors.

3.1.2 Photolithography

Photolithography is used to pattern the sample or protective etch mask layer. It allows device shapes to be etched in to the wafer, transparent contact layers and metal contacts to be deposited.

A thin film of positive or negative photoresist is applied by spin coating, following this the sample is usually baked. The desired photomask(see 3-1) is used to transfer the pattern to the photoresist by exposing unmasked areas to UV light. The pattern shown in Figure 3-1 is $5mm \times 5mm$, with the largest devices measuring $1mm \times 1mm$. The $5mm \times 5mm$ pattern was repeated over a 5" mask.

The following relationship is used to calculate the time for which the resist should be exposed: Exposure time = Dose ($mJ.cm^{-2}$)/ Intensity ($mW.cm^{-2}$). After exposure the photoresist must be developed in a developer solution.

3.1.3 ICP Etch

Inductively coupled plasma (ICP) etching is a process which involves the employment of a high energy, chemically reactive plasma to remove unwanted material from a wafer.

An ICP etch is used to remove layers in order to expose the n-GaN to create a mesa structure and also to isolate each device. Layer removal is necessary for depositing metal contacts. A number of different plasmas are used to remove different materials. An oxygen etch is used to remove any excess resist left. This is followed by a CHF_3 etch, used to etch windows into the protective layer. CHF_3 will etch both SiO_2 and HSQ.

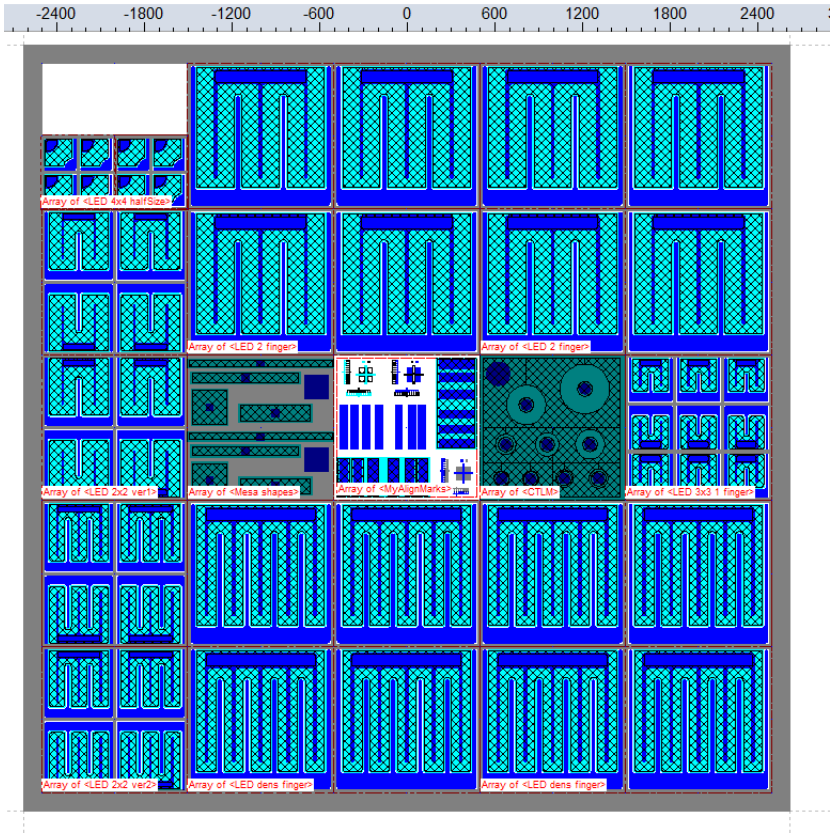

Figure 3-1: Photomask (5mm x 5mm) with different device sizes and test patterns.

Finally the n-layer is exposed and the device isolated by using a Cl_2/Ar plasma. However a BCl_3 plasma can also be used and has been shown to lower series resistance and leakage currents [132] [133].
After etching the remaining photoresist is removed in a resist stripper. The protective etch mask is removed in buffered oxide etch (BOE). BOE is a solution comprising of hydrofluoric acid (HF)and ammonium fluoride (NH_4) in a ratio of $1:5 = HF:NH_4$.

3.1.4 Contact Formation

A number of techniques are used to deposit both the transparent contact and the metal pads. These are discussed below.

Electron beam evaporation

Electron beam evaporation is a common deposition technique which works by using a beam of electrons to bombard the target material i.e. the material to be deposited. Under a high vacuum (7.5×10^{-5} Torr) a charged tungsten filament is used to to generate an electron beam. This beam is directed toward the target material where the electron's energy is transferred and causes the material to heat and transform into its gaseous phase. This gaseous material then solidifies coating everything within the chamber with the target material.

LEDs require a current spreading layer to ensure uniform current injection into the p-layer, however it is vital that this layer be transparent. A thin layer of Ni/Au (5nm/5nm) is deposited via electron beam (e-beam) evaporation. A lift-off process is then performed before the sample is then annealed in a rapid thermal annealer (RTA) at 500 C in O_2 for approximately 5 minutes. ITO is a common alternative to Ni/Au.

Following this the metal contacts are deposited, also by e-beam evaporation. Typically this are Ti/Al/Ni/Au. Again a lift off step is performed post-deposition. Figure 3-2 shows the structure of the final device. Devices fabricated for this work and discussed in later chapters, ranged in size from 0.25mm - 1mm.

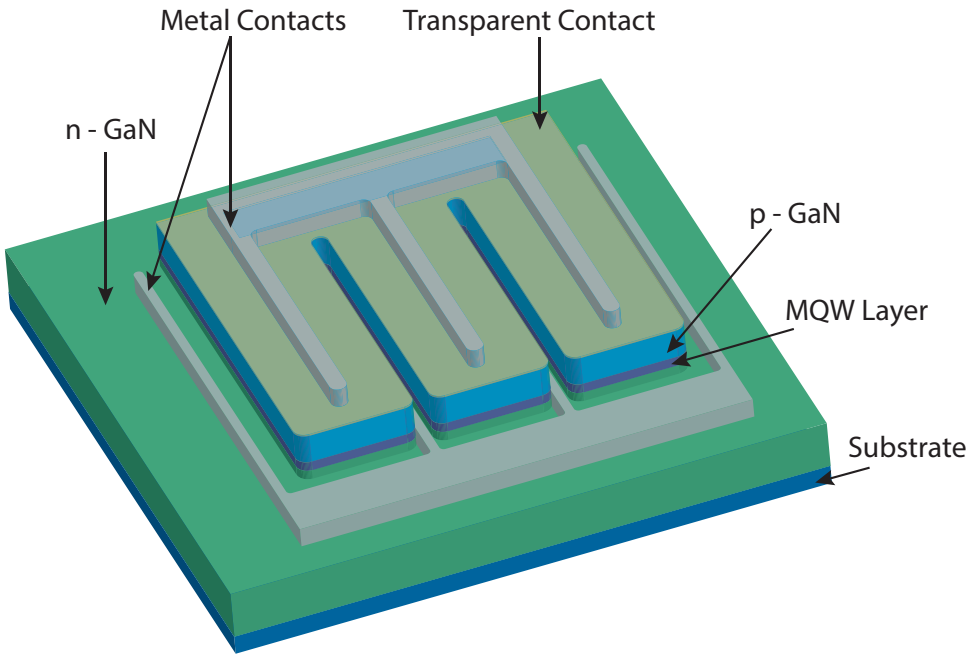

Figure 3-2: Structure of working device.

Sputter Deposition

The LEDs discussed in chapter 5 and chapter 6 required additional processing. The deposition of any interlayer follows a similar procedure to the one outlined in the previous section.

Sputter deposition is a means of depositing a thin film of a material [134]. The process involves the material transitioning from a condensed phase, to a vapour phase [1] and then back to a condensed phase (this is the deposited thin film). The most straightforward method of sputtering uses a plasma (usually generated from a noble gas e.g Ar). The target (which is the source material) is negatively biased, which causes the plasma to bombard its surface, transferring energy and causing the material to be released as a vapour. It is this removing of atoms from the surface of the target that is known as sputtering. This vapour can then re-condense on the substrate. The substrate is often positively biased. It is this bias between target and substrate that is used to generate a plasma. However

[1] Hence sputter deposition is a type of Vapour Phase Epitaxy (VPE) and is done under high vacuum conditions.

the sputtering method used to deposit the thin films examined in later chapters does not employ a biased substrate as the plasma is generated remotely. Further information on this can be found on the Plasma Quest website.

Those presented in chapter 5 had the metal interlayer deposited as above, but prior to the lift-off step, an indium tin oxide (ITO) or aluminium zinc oxide (AZO) layer is deposited by low temperature sputtering (the substrate is not heated or biased). The lift-off step is then carried out. It was found that this technique does not work well. Whilst it is somewhat uncertain it is likely to be the case for several reasons. These layers are relatively thick, making it more difficult for the solvent to penetrate. A thicker resist and a greater undercut may help ease this, but another technique is outlined below.

The LEDs detailed in chapter 6 have the lift-off step performed post interlayer deposition. The AZO layer is then blanket deposited on top of the samples. This is followed by a further lithographic step using a positive resist and the transparent contact mask. The AZO is then etched using a 500:1 $H_2O : HCl$ solution. The HCl used was 12M, 37 %. Time for etching can be quite variable, so samples are checked every 20 seconds until etched.

3.2 Device Characterisation

LEDs are characterised by first using a CCD camera mounted on a microscope to image the device at both high and low magnification, and allows for the distribution of light emission to be measured over a range of drive currents. This reveals any issues arising from poor electrical contacts giving rise to the presence of intermittent series resistance which reduces the proportion of the applied voltage being dropped across the active region of the LED, to reduce locally the intensity of the emission. A neutral density filter may be required to avoid saturating the CCD.

Pulsed light - current - voltage (L-I-V) measurements are then performed in a dark box (to screen from any stray light), using short ($\sim 1 - 10ms$) pulses on a long duty cycle ($\sim 1s$) in order to minimise the effects of device heating.

The electroluminescence spectrum measurements are taken over a range of drive currents to determine if a Stark shift occurs or if parasitic emission (from defects) is present.

3.2.1 Material Characterisation

Scanning Electron Microscopy

Scanning Electron Microscopy (SEM) is a high resolution imaging technique. A focused beam of electrons (from a thermionic emission source) moves across the sample surface [135]. These electrons interact with the sample and produce an array of signals (secondary electrons, backscattered electrons and x-rays) which can be used to determine composition and topographical information. The resolution is determined by the electron spot size and the interaction volume, with some systems being able to achieve sub-nanometre resolution (although atomic resolution is not achievable). The penetration depth of the beam is dependent on a number of variables such as the accelerating voltage and the density of the material being penetrated. Field Emission Scanning Electron Microscopy (FESEM) uses a field emission electron source, as opposed to a thermionic emission source used in SEM. Thermionic emitters heat up a filament with a current, which will emit electrons once a certain temperature is reached. Field emission differs in that the filament is placed in a large potential gradient in order to generate a beam of electrons. Electron beams generated in this way have smaller diameters and are more coherent than those generated by thermionic sources, resulting in enhanced resolution and signal-to-noise ratio.

Atomic Force Microscopy

Atomic Force Microscopy is a characterisation technique which can be used to provide a variety of information about the sample under investigation, including three-dimensional topography of the sample's surface [136]. The resolution of such images is tens of nanometres in the horizontal but down to a tenth of a nanometre in the vertical direction. A cantilever with a sharp tip is used to scan the surface. Measuring the force between the sample and tip allows for the determination of mechanical properties such as Young's modulus or stiffness. Topographical images are constructed by measuring the sample's position with respect to the tip. Such images can be seen in later chapters.

3.2.2 Electrical Characterisation

Careful and detailed electrical characterisation plays a vital role in determining material quality and device reliability. These characteristics are also indicative of the quality of processing techniques used. Low forward and subthreshold leakage currents, as well as large breakdown voltages, are required in order to ensure extended device lifetime and tolerance of electrostatic discharge. It is known that threading dislocations increase the reverse leakage current, however they do not appear to effect the forward voltage [62]. Increased reverse leakage has also been correlated with diminished light output. A number of conduction mechanisms may contribute to carrier leakage and are discussed in 3.2.2.

Theory

A pn-junction is an interface p-type and n-type semiconductor material. Electrons from the n-type side will diffuse into the p-type side and holes will do the same in the opposite direction. These carriers recombine, leaving the vicinity of the interface depleted of free electrons and holes, which is known as the depletion region. A space charge region is formed because as carriers diffuse they leave behind ions, which gives rise to the diffusion voltage, V_D, this is the barrier that must be overcome in order for carriers to reach the opposite side of the depletion region. When an external bias is applied this barrier will change, that is it will decrease when a forward bias is applied and increase when a reverse bias is applied. A forward bias (see figure 3-4) will cause carriers to be injected into the depletion region, they will then diffuse towards the regions of opposite conductivity and recombine. See [111] for a comprehensive discussion on the theory of semiconductor devices and [10] for a discussion of LEDs specifically.

The Shockley equation describes the I-V relationship of a pn-diode with a cross-sectional area, A:

$$I = qA\left(\sqrt{\frac{D_p}{\tau_p}}\frac{n_i^2}{N_D} + \sqrt{\frac{D_n}{\tau_n}}\frac{n_i^2}{N_A}\right)(e^{qV/kT} - 1) \tag{3.1}$$

Where D_p and D_n are the hole and electron diffusion coefficients respectively. When the device is under forward bias the Shockley equation, (3.1), can be expressed as follows:

$$I = qA\left(\sqrt{\frac{D_p}{\tau_p}}N_A + \sqrt{\frac{D_n}{\tau_n}}N_D\right)e^{q(V-V_D)/kT} \tag{3.2}$$

This can also be done for reverse bias conditions:

$$I = I_0(e^{qV/kT} - 1) \tag{3.3}$$

Where I_0 is the reverse saturation current, which can be expressed as follows:

$$I_0 = qA\left(\sqrt{\frac{D_p}{\tau_p}}N_A + \sqrt{\frac{D_n}{\tau_n}}N_D\right) \tag{3.4}$$

Equation (3.2) shows that as applied voltage gets close to the diffusion voltage, the current begins to increase rapidly, this is known as the threshold voltage, V_{th}.

A modification of the Shockley equation is required for non-ideal diodes. The inclusion of the ideality factor,n_{ideal}, acts to compensate for the deviation away from ideal behaviour where $n_{ideal} = 1$.

$$I = I_0 e^{qV/(n_{ideal}kT)} \tag{3.5}$$

The presence of parasitic resistances is frequently observed in LEDs, these can be categorised as series or parallel resistances. The former originates in the bulk semiconductor, processing induced damage or contact resistances and the latter from parasitic conducting pathways.

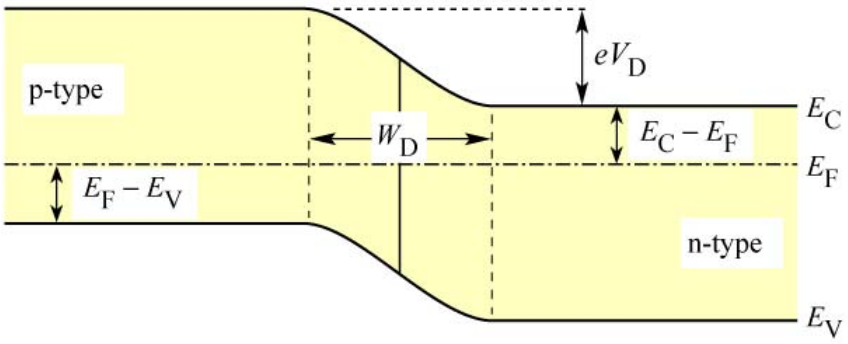

Figure 3-3: A pn junction at zero bias [10].

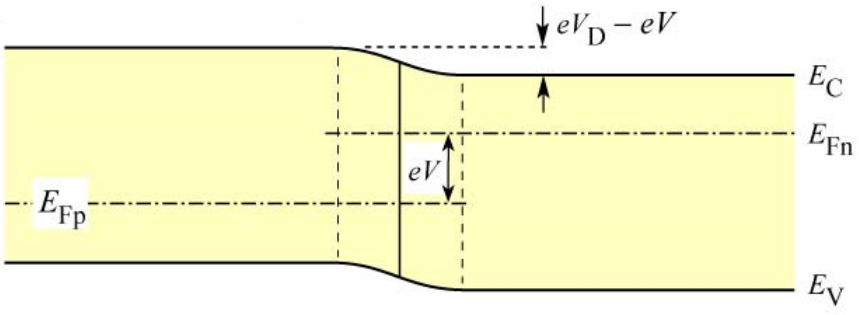

Figure 3-4: A pn junction in forward bias [10].

Leakage Current

LED leakage current is comprised of both the reverse leakage current and the subthreshold forward leakage current. The latter is sometimes observed in the form of a "soft turn on" which presents itself in the IV characteristic as a gradual increase in current when compared with sudden increase seen in diodes exhibiting ideal (or almost ideal) behaviour). Reverse leakage current, $I_{leakage}$ can be written in terms of its components [137]:

$$I_{leakage} = I_{drift,diffusion} + I_{generation,recombination} + I_{interband,tunnelling} + I_{thermally,assisted,multistep,tunnelling} + I_{surface,leakage} + I_{other} \quad (3.6)$$

The first three terms of (3.6) have been shown to be too insufficient in accounting for the magnitude of measured leakage currents [137], [138] [139], [140].

GaN is known to have a high density of defects (compared with other semiconductors e.g. GaAs), which induce deep levels within the bandgap. Carriers are then able to tunnel between such levels (thermally assisted multi-step tunnelling) [138]. Significant polarisation fields are know to exist in GaN and may result in the coloumbic potential barrier of deep level traps being lowered, resulting in the enhancment of the thermal emission of carriers from these deep levels (Poole-Frenkle emission) [141], [138]. Carrier leakage is known to be dependent on temperature so thermally assisted tunnelling and Poole-Frenkle emission are likely to dominate at room temperature, however at low temperatures, variable range hopping is thought to dominate the reverse leakage [137] [111].

P-contact Resistance

Circular transmission line patterns were fabricated and were used to determine the p-contact resistance as seen in 3-5.

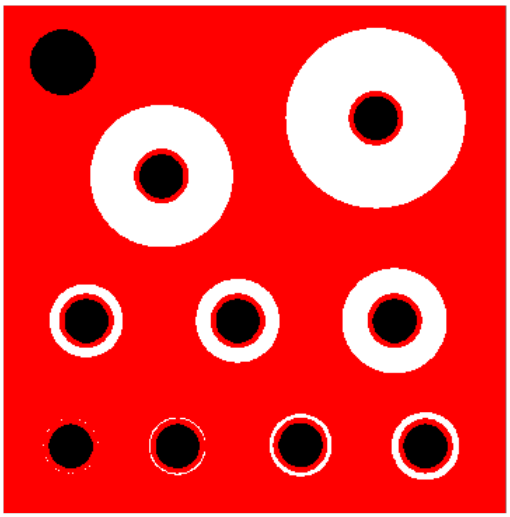

Figure 3-5: Circular transmission line test pattern

The pattern consists of nine circular electrodes with varying separations. A probe is placed on the pad which can be seen in the upper left-hand corner. A second probe is then placed on one of the nine electrodes and an IV measurements made. This is then repeated for each of the electrodes. The resistance for each can then be determined and plotted against the corresponding separation.

$$R = \frac{R_{sh}}{2\pi}\left[ln\left(\frac{d+r}{r}\right) + \sqrt{\frac{\rho_c}{R_{sh}}}\left(\frac{1}{d+r_o} + \frac{1}{r}\right)\right] \tag{3.7}$$

Where R_{sh} is the sheet resistance of the p-GaN, ρ_c is specific contact resistance of the p-type contact, r is the radius of the inner contact and d is the separation of the inner and outer contact. R is the sum of r and d.

Equation (3.7) can be rewritten as shown below:

$$R = \frac{R_{sh}}{2\pi}\left[ln\left(\frac{R}{r}\right) + L_T\left(\frac{1}{R} + \frac{1}{r}\right)\right] \tag{3.8}$$

Where L_T is the transfer length. The total resistance can then be plotted against the separation width. Non-linear fitting can then be undertaken(this was

done using our in-house LabVIEW contact resistance software). The gradient of this line is equal to $\frac{Rsh}{2\pi r}$. The x-axis intercept gives $2L_T$. Finally the y-axis intercept is equal to $2L_T\frac{R_{sh}}{2\pi r}$. From the intercepts and the gradient, the contact resistance $R_(c)$ and the specific contact resistance ρ_c can be determined using the equations shown below.

$$R_c = R_{sh}L_T \tag{3.9}$$

$$\rho_c = R_{sh}{L_T}^2 \tag{3.10}$$

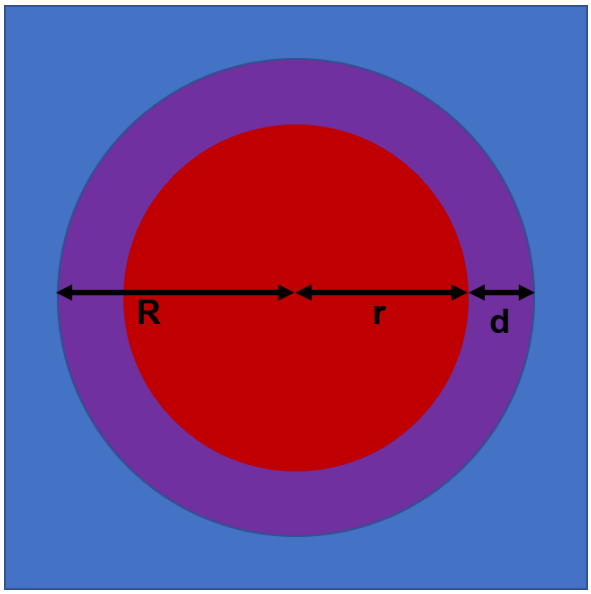

Figure 3-6: CTML test pattern showing parameters R, r and d

Secondary Ion Mass Spectrometry

Secondary ion mass spectroscopy (SIMS) is a characterisation technique, preformed under high vacuum ($x10^{-6}$ torr), used to determine the composition of surfaces [142]. It works by using an ion beam to sputter (see 3.1.4) the surface in question and employs a mass spectrometer to measure the mass/charge ratio of the ejected ions. The composition can be determined to a depth of 1nm-2nm. The majority of particles being emitted from the test sample are not the ions being analysed. The sample is undergoing a sputtering process and as such the surface morphology is being altered. The impact of this is dependent on the dimensions of the ion beam and whether the current is continuous or pulsed.

In this work SIMS measurments were used to characterise interlayers deposited underneath a thick transparent contact (ITO or AZO).

Electron Beam Induced Current

Electron beam induced current (EBIC) [143] is used to identify barriers or defects in semiconductors and is similar to cathodoluminescence measurements. An electron beam is used to create electron-hole pairs. If there is an inbuilt electric field (e.g. from the depletion region of a p-n junction), the separation of the pair will cause a current to flow (EBIC current). This can then be used to build up an image, allowing for the identification of barriers (these glow brightly) or defects (dark spots) within the structure. Minority carrier characterisation can be preformed using the shape, size and contrast of any barriers. In this work they are used to better understand the nature of TCOs using thin interlayers.

3.2.3 Optical Characterisation

Ideally all recombination would be radiative and all light would escape from the device, but in reality of course neither happens. Determining the optical properties of LEDs is essential in understanding the physics of the device and diagnosing issues with the material, especially in the active region e.g. regions in which non-radiative processes dominate.

Emission Spectrum

The most fundamental measurement when characterising an LED is the emission spectra, which allows the peak wavelength of the emitted light to be determined. These measurements will also reveal the presence of any parasitic emission, which is highly indicative of defect states. The electroluminesence (EL)spectrum is often measured over a range of bias levels in order to assess any shift in the peak emission wavelength, which is a signature of a strong quantum confined stark effect (QCSE).

Photoluminescence (PL) employs an intense light source (i.e. a laser) to generate excess carriers which then recombine, either radiatively or non-radiatively. This technique is useful when assessing the optical properties of a material, however its strong PL emission does not always correlate with strong EL emission.

Light output

Light output measurements are essential in examining the efficiency of an LED. This is often measured with a photodetector over a range of bias levels. The relationship between the two can then be analysed to determine the quantum efficiency (η_{QE}) and any factors which limit it. The injection current can be related to the carrier density in the QW,n, by the following relationship:

$$I = qV_{QW}(An + Bn^2 + Cn^3) \tag{3.11}$$

The coeffiecients are defined in the first chapter. The photocurrent is measured by the detector and can be written as follows.

$$I_p = \frac{Bn^2}{k} \tag{3.12}$$

The ratio between the photocurrent, I_p and the injection current gives η_{QE}.

$$\eta_{QE} = \frac{I_p}{I} \tag{3.13}$$

Figure 3-7 shows how the non-radiative, radiative, Auger and other higher order terms impact on the efficiency of the device, and allow us to determine which processes dominate and when.

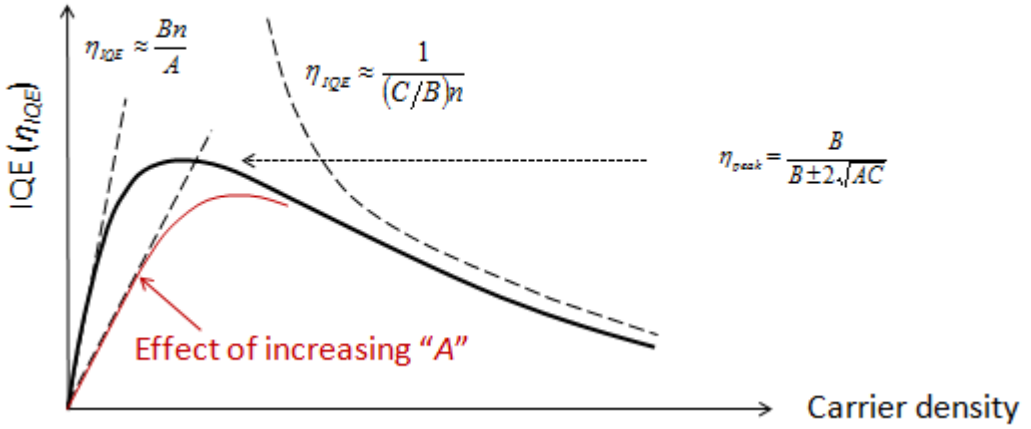

Figure 3-7: The effect of changing parameters in the ABC model on the efficiency of an LED

3.3 Characterisation setup

The first system shown in (Figure 3-8) consists of a CCD camera, connected to the control computer, mounted on to a microscope. A source measure unit (SMU) is used to drive the device under test (DUT). A DC current (or voltage) can be applied and then images taken via the software supplied with the camera. The SMU is controlled using LabVIEW and can be used to take I-V measurements.

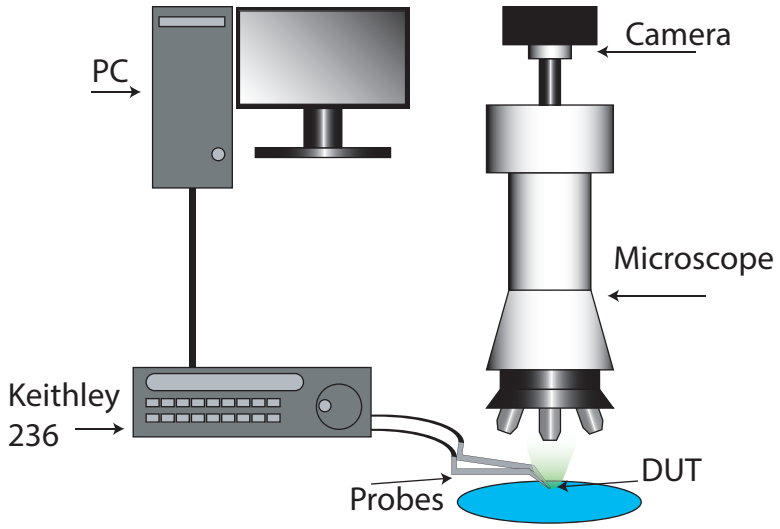

Figure 3-8: System used for CCD imaging and I-V measurements

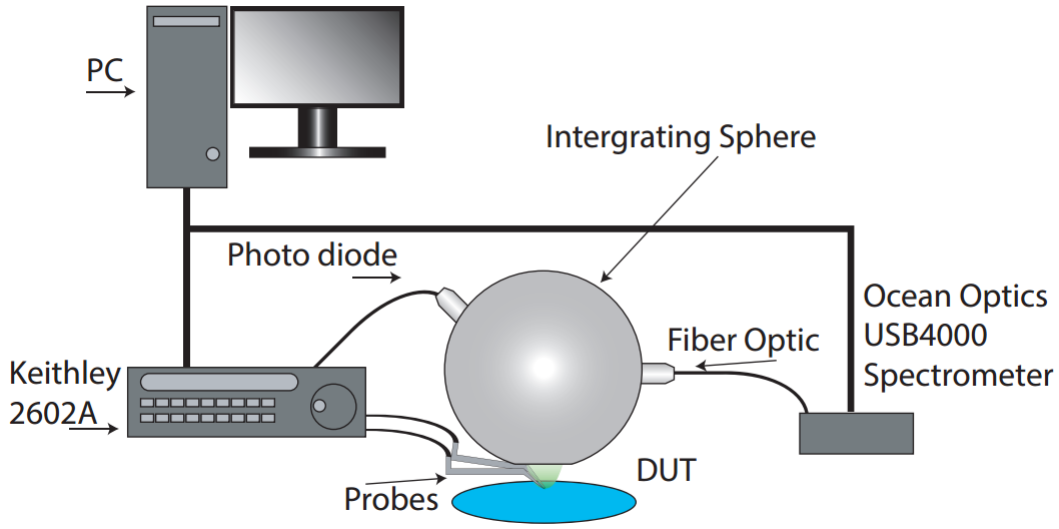

Figure 3-9: Schematic of the integrating sphere system

The second system (Figure 3-9) consists of an integrating sphere [2] connected to a SMU and spectrometer. A dual channel SMU is used, with one channel used to drive the DUT and the second used to measure the photocurrent from the integrating sphere. The software used to control these measurements was written in-house specifically for this application. The SMU is also used to drive the device whilst the spectrum is measured using manufacturer supplied software. Unfortunately it is not possible for the device to sit inside the integrating sphere, so the opening sits as close to the device as possible. This leads to the integrating sphere slightly underestimating the emitted optical power.

[2] An integrating sphere is a device which spatially integrates radiant flux.

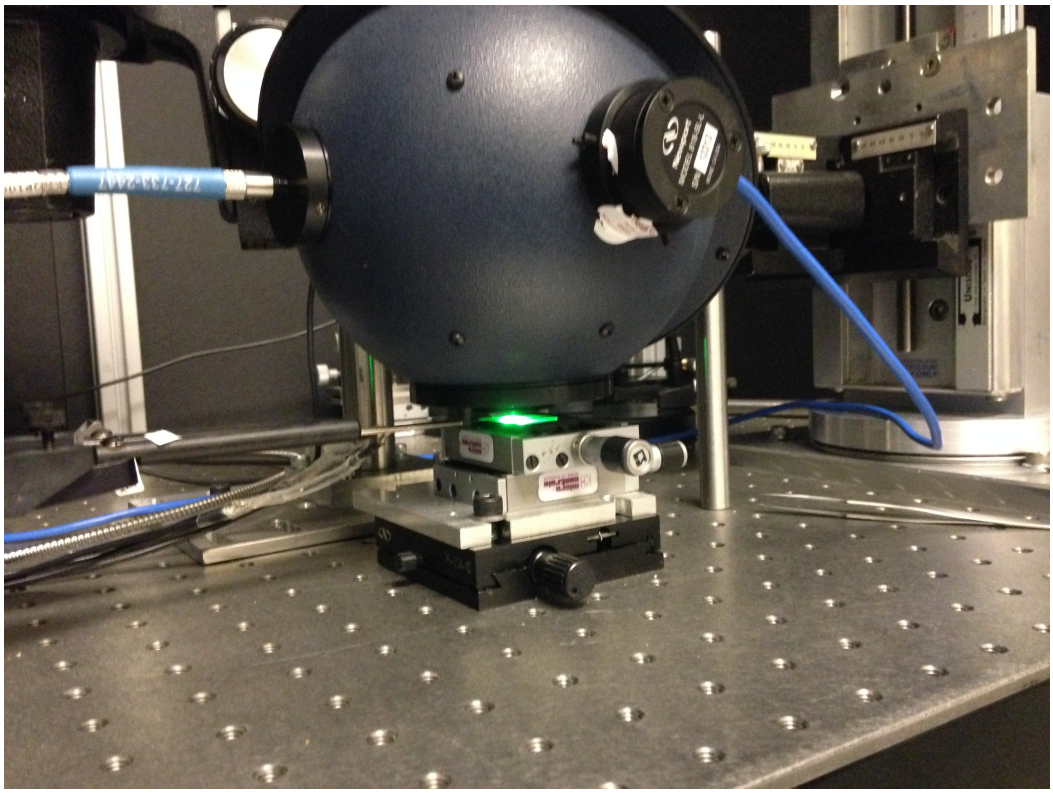

Figure 3-10: The integrating sphere system and illuminated LED

This chapter is adapted from the author's confirmation report [37].

Chapter 4

Long wavelength LEDs

The efficiency of GaN based LEDs reduces as wavelength increases (see 2.1.2). This chapter presents the results on LEDs emitting within the green gap region and explores the mechanisms that lead to reduced performance. All samples were fabricated and characterised in-house. Temperature dependent measurements were performed on samples 1 and 2 only. Samples 2 and 4 were comparable in behaviour and thus conclusions about both could be drawn from measurements on sample 2 only. Sample 3 was omitted as this sample had a very high rate of device failure, which made measuring the same device at many temperatures impossible.

The work contained in this chapter was presented at the International Conference on Advanced Semiconductor Devices & Microsystems [144].

4.1 LEDs emitting in the green gap

A number of samples with varying In content were kindly provided by IQE [1]. Overall they possess a similar structure but there were changes to the number and growth method of the QWs, namely differences in temperature ramp rates and interruption times during growth. Whilst the observed results inevitably arise due to these differences, details of growth recipes are commercially sensitive and are therefore not discussed. A commercially grown sample was used as a control, it's structure can be seen below, Figure 4-1.

[1] IQE Europe ltd. Pascal Close, St. Mellons, Cardiff, South Glamorgan CF3 0LW

Sample numbers, their corresponding emission wavelengths and approximate In content of QWs are shown in the table below.

Sample	1	2	3	4
Emission λ	500nm	550nm	500nm	600nm
Approx In %	47%	65%	47%	85%

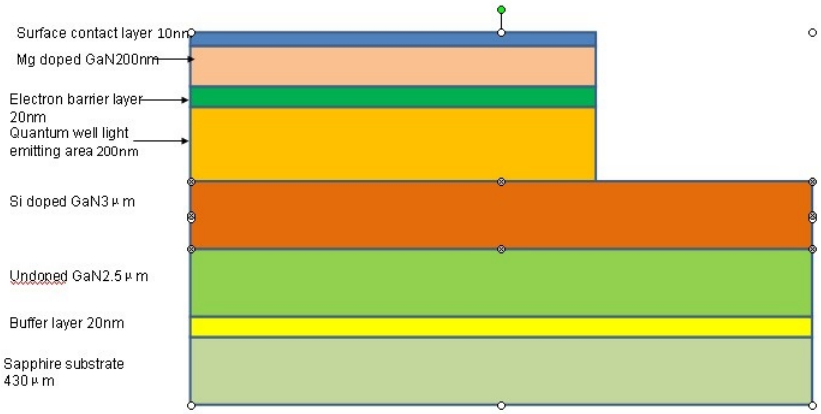

Figure 4-1: Epitaxial structure of the commercially grown control sample.

4.1.1 CCD images of devices under bias

CCD images are made of illuminated LEDs to check the uniformity of light emission from a single chip. Non-uniform emission is indicative of non-uniform current density and hence poor current spreading. Poor current spreading occurs if the chip design is non-optimum or the device fabrication, notably the contact resistance, is unsatisfactory.

Control Sample

CCD images of the control sample can be seen in Figure 4-2. The uniformity remains consistent regardless of injection current.

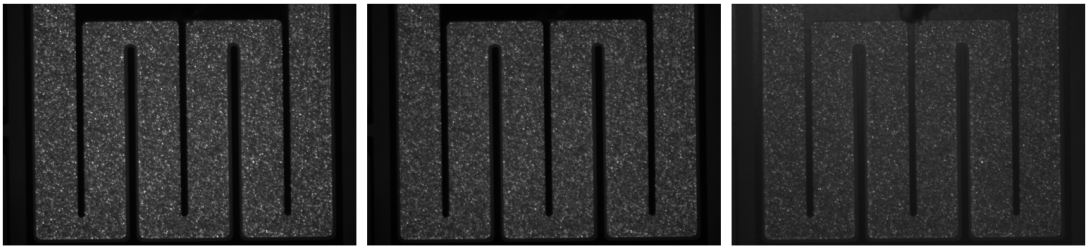

Figure 4-2: Control device at different injection currents. Device shown is $500\mu m \times 500\mu m$.

Sample 1

Sample 1 exhibits dark patches which are independent of injection current (see Figure 4-3). Correlated electron beam induced current (EBIC) and cathodoluminescence measurements of similar dark patches in blue LEDs have revealed that excessive non-radiative recombination occurs in these dark patches [145], indicating a material non-uniformity, possibly indium segregation occurred under the MQW growth conditions used for this samples.

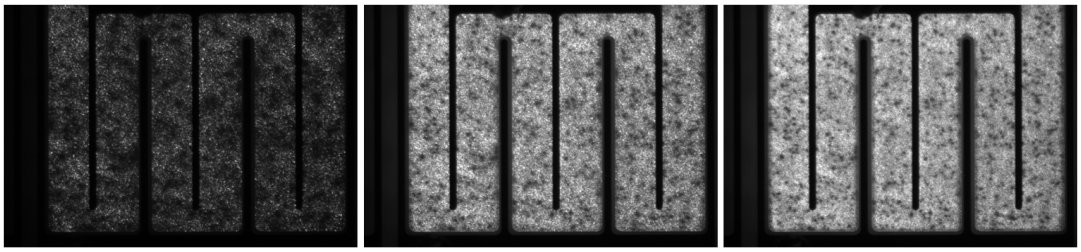

Figure 4-3: Sample 1 at different injection currents. Device shown is $500\mu m \times 500\mu m$.

Sample 2

Sample 2 remains relatively uniform regardless of injection current, although evidence of current crowding can be seen in Figure 4-4 (c). This is seen in the image as areas that are brighter (lighter) around the outside of the illuminated device, beside the outer electrode.

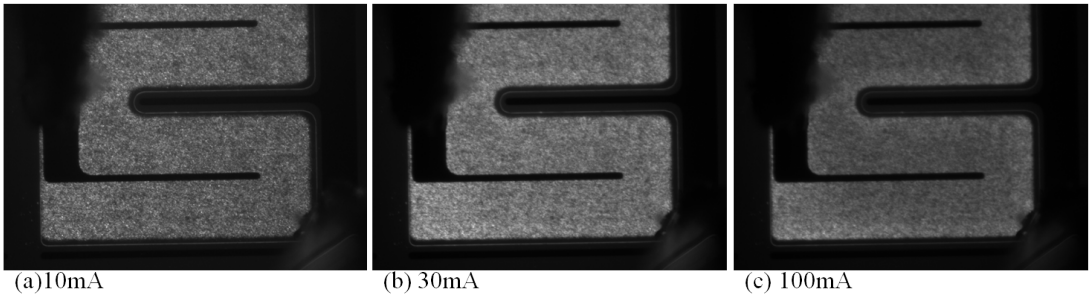

Figure 4-4: Sample 2 at different injection current.Device shown is $500\mu m \times 500\mu m$.

This sample, as well as sample 4, exhibited luminescence in reverse bias as seen in Figure 4-5. Although a detailed analysis of this has yet to done, it is thought that this may arise from defects within the active region.

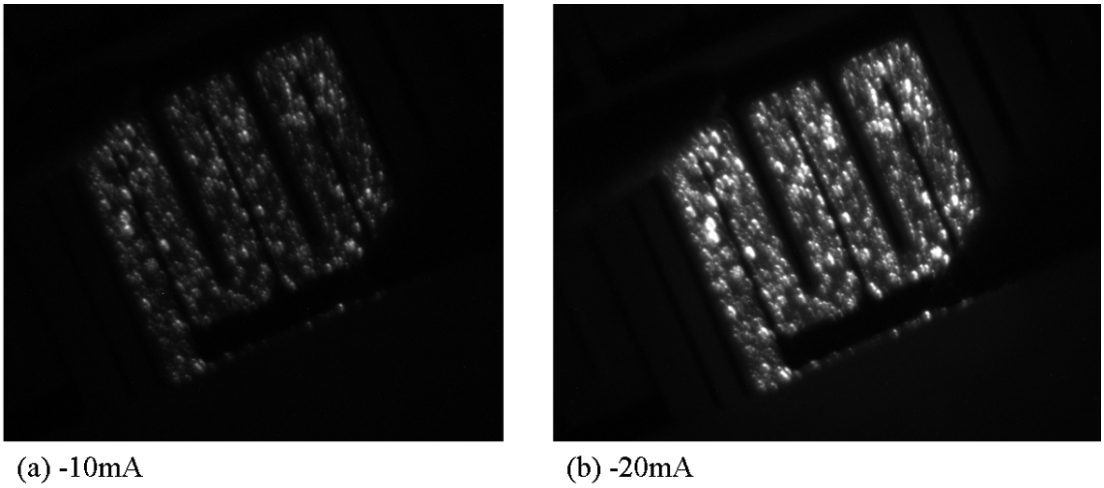

Figure 4-5: Sample 2 in reverse bias. Device shown is $500\mu m \times 500\mu m$.

Sample 3

The emission from sample 3 is particularly non-uniform (see Figure 4-6). The aligned bright patches seen in this sample are symptomatic of an off axis substrate [146] and step flow epitaxial growth [147]. This sample also had a high turn on voltage, suggesting substantial series resistance. Devices on this wafer also had a very high failure rate once the injection current was greater than approximately 50mA, a further indication of non-optimum epitaxial growth.

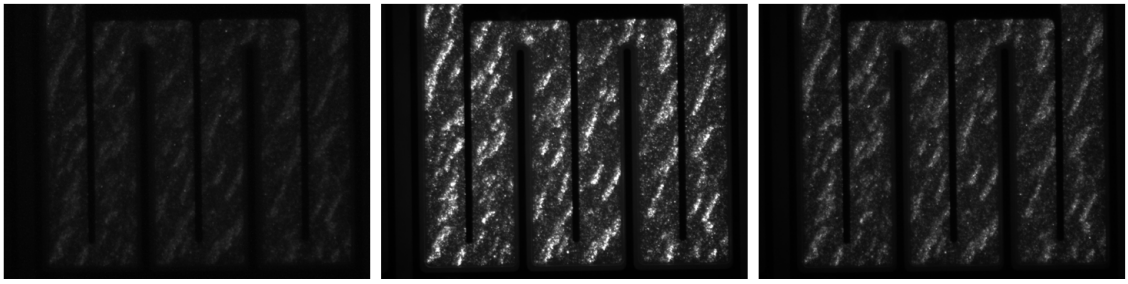

(a) 300uA (b) 1mA (c) 20mA

Figure 4-6: Sample 3 at different injection current. Device shown is $500\mu m \times 500\mu m$.

Sample 4

Like sample 2, sample 4 remains relatively uniform regardless of injection current and also exhibits current crowding although it is seen at lower current densities. This sample also exhibits reverse bias luminescence.

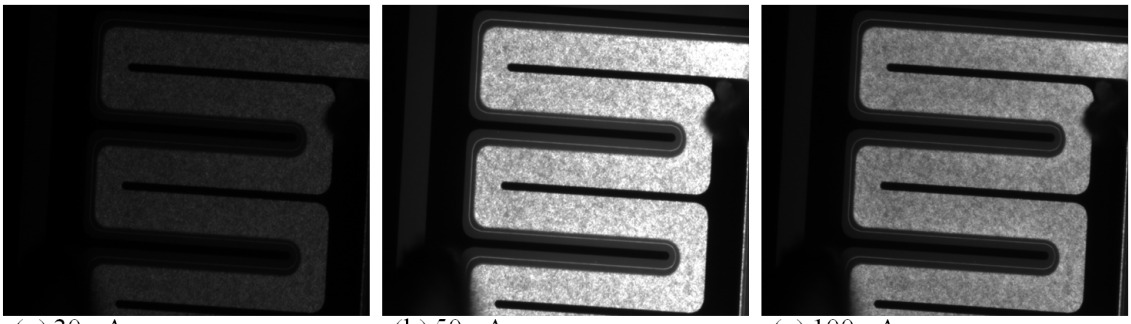

(a) 30mA (b) 50mA (c) 100mA

Figure 4-7: Sample 4 at different injection current. Device shown is $500\mu m \times 500\mu m$.

4.1.2 Electrical Characteristics

This section will present the main results of the electrical characterisation.

I-V Characteristics

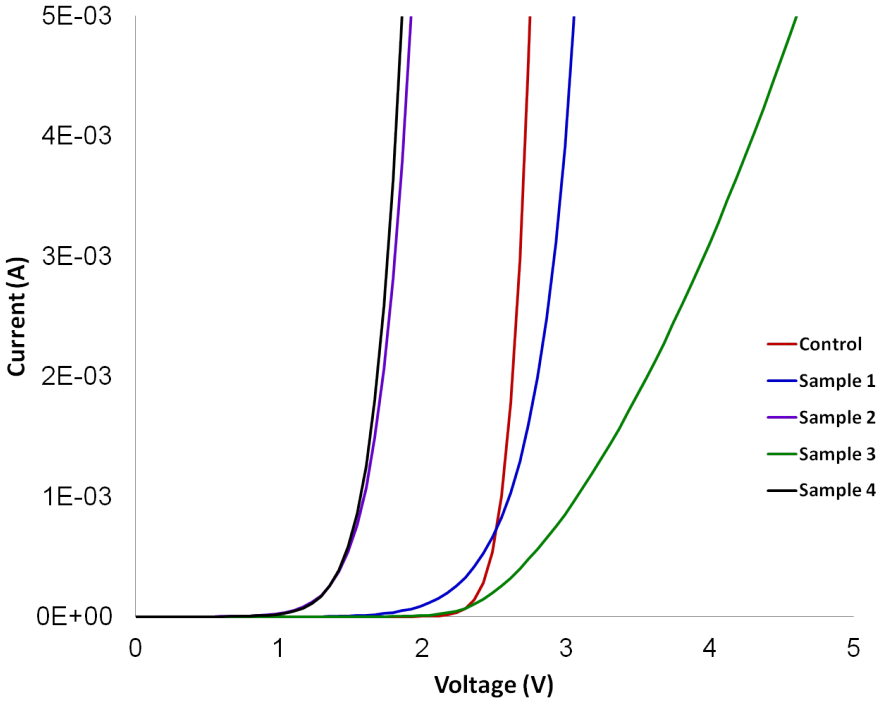

Figure 4-8: Forward I-V characteristics.

The forward bias I-V relationship shown in Figure 4-8. For a good quality device, the approximate turn-on voltage is numerically equivalent to the bandgap of lowest bandgap component [10]. For the devices discussed here these should be 2V - 2.5V. The deviation from this, especially for samples 2 and 4, is indicative of poor device quality. The control sample however, is within reasonable agreement with this approximation of turn-on voltage.

Figure 4-8 clearly shows that sample 3 has a large series resistance, evidenced by the less rapid rise in current for applied voltage > 2.3V. All samples, except the control, exhibit sub-threshold turn-on, which is highly indicative of the existence of defect states. The control sample has a sharp turn on and steep gradient after it has passed the threshold voltage. This suggests that the control sample is low

in defects and has a small series resistance.

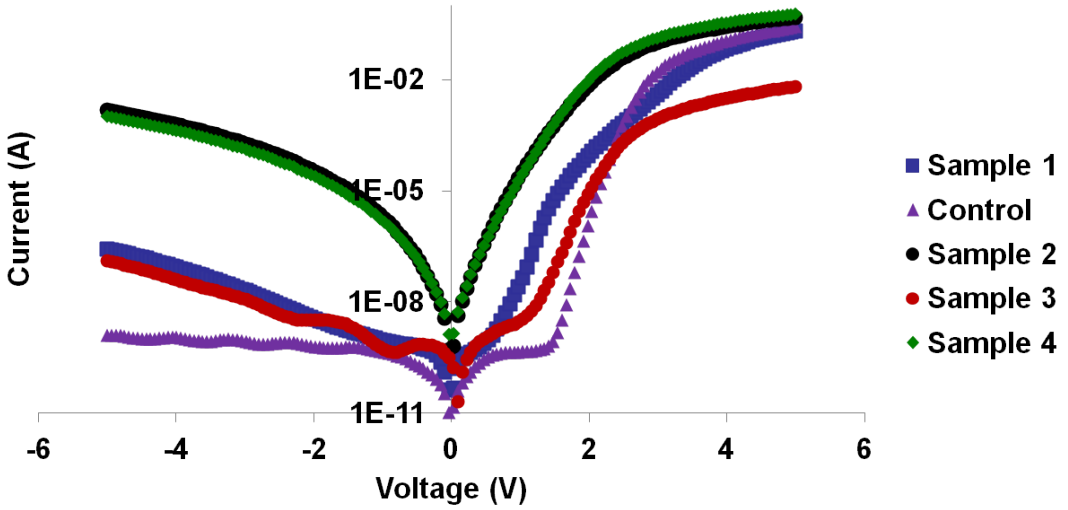

Figure 4-9: Forward and reverse I-V characteristics plotted on a semi-log scale.

Replotting the I-V characteristics on a semi-log scales allows for greater insight into the processes which may be effecting device performance. The reverse leakage current of the control sample is very small ($\sim nA$), and little forward leakage is observed. Samples 2 and 4 clearly exhibit dramatic subthreshold and reverse bias leakage. This is not surprising given that these samples also emit light in reverse bias.

Identifying leakage mechanisms

There are a number of ways that I-V characteristics can be replotted in order to try to diagnose the mechanisms behind the observed leakage currents. Replotting using the method devised by Missous and Rhoderick [148] allows an accurate determination of the saturation current, I_o, from the intercept of the y-axis (this is only valid for the linear region). This is representative of the minority carriers diffusing in the opposite direction to the majority carriers. The control sample exhibits a saturation current in the order of tens of picoamps, which is consistent with what would be expected of a GaN LED. This is due to its wide band gap and so there is a decreased likelihood of electrons being excited to the conduction band and therefore there are fewer minority carriers. The saturation

current for samples 1 and 3 is an order of magnitude higher than the control sample. The saturation current of samples 2 and 4 is an order of magnitude higher again. This suggests there are a greater number of minority carriers in these samples.

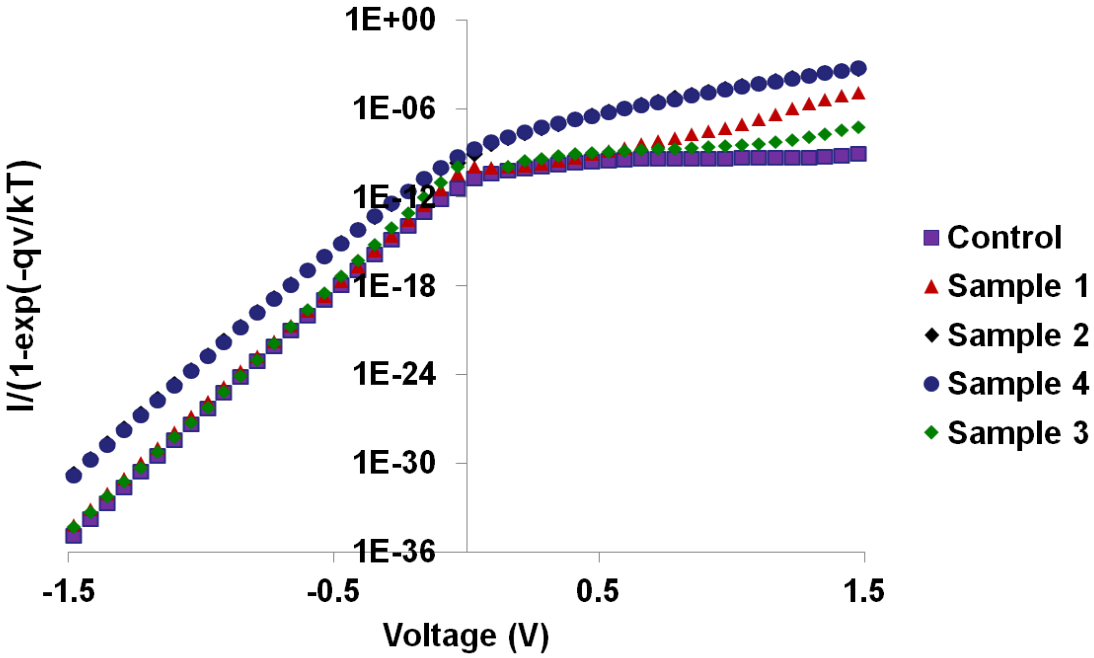

Figure 4-10: IV characteristic can be plotted according to Missous and Rhoderick [148].

The I-V characteristics can be replotted as shown in Figure 4-11. The linear relationship exhibited by sample 2 in forward bias is indicative of the presence of Poole-Frenkle emission in this sample, however this is not seen, at least not so obviously over an extended voltage range, in the other samples.

Poole-Frenkle emission describes the process by which trapped carriers are excited to the conduction band in the presence of an applied or internal electric field. The field acts to reduce the barrier height and so reduces the amount of thermal energy required to excite the carrier. Thus this becomes a mechanism for the current flow. Trap depth (for those with coulomb potentials) is equivalent of the barrier height.

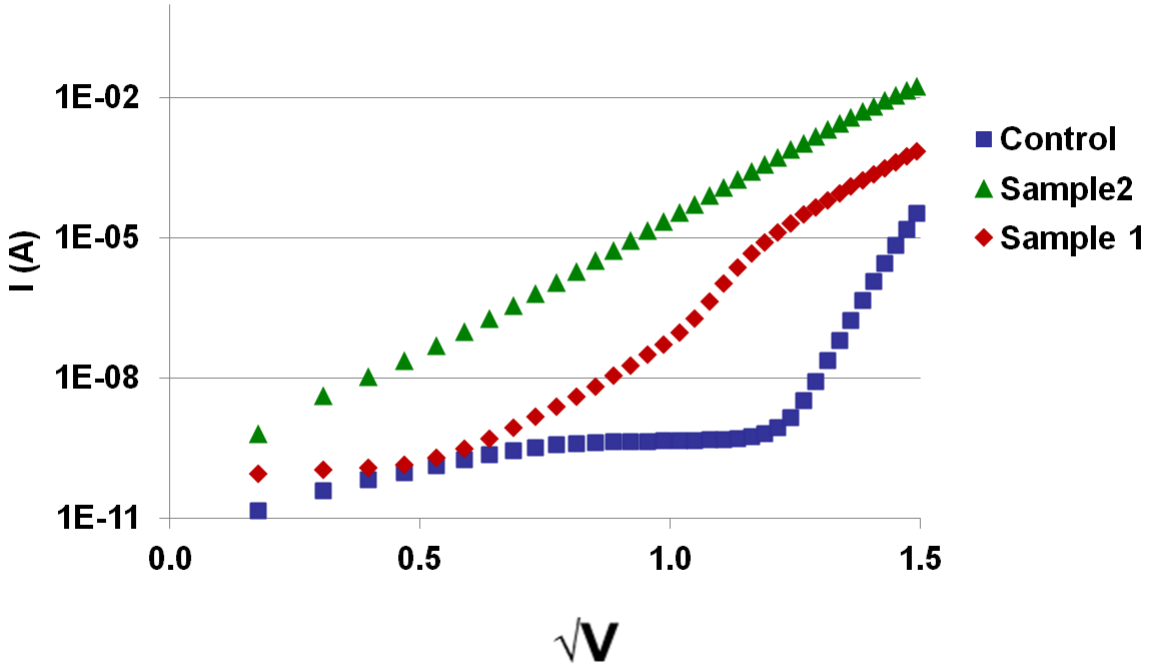

Figure 4-11: Carrier mechanisms can be determined by replotting the IV characteristic as $sqrt_V$ against current on a semi-log scale.

It is evident from Figure 4-12 that a linear relationship exists at lower temperatures, although this breaks down at higher temperature. This relationship suggests that Poole-Frenkle emission is present in this sample.

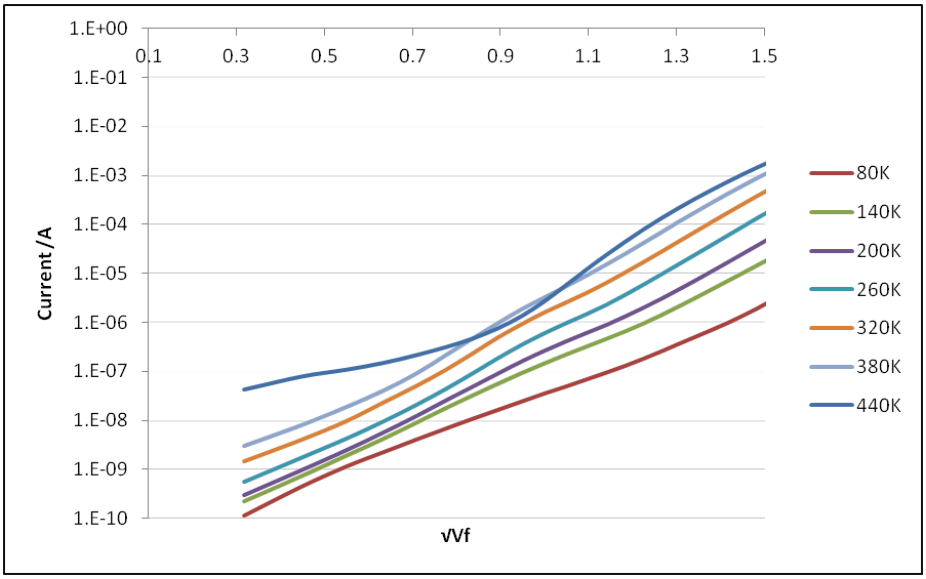

Figure 4-12: Replotted IV characteristic for Sample 1 at different temperatures.

Sample 2 very clear exhibits evidence of Poole-Frenkle emission being the dominant conduction mechanism at sub-turn-on voltages.

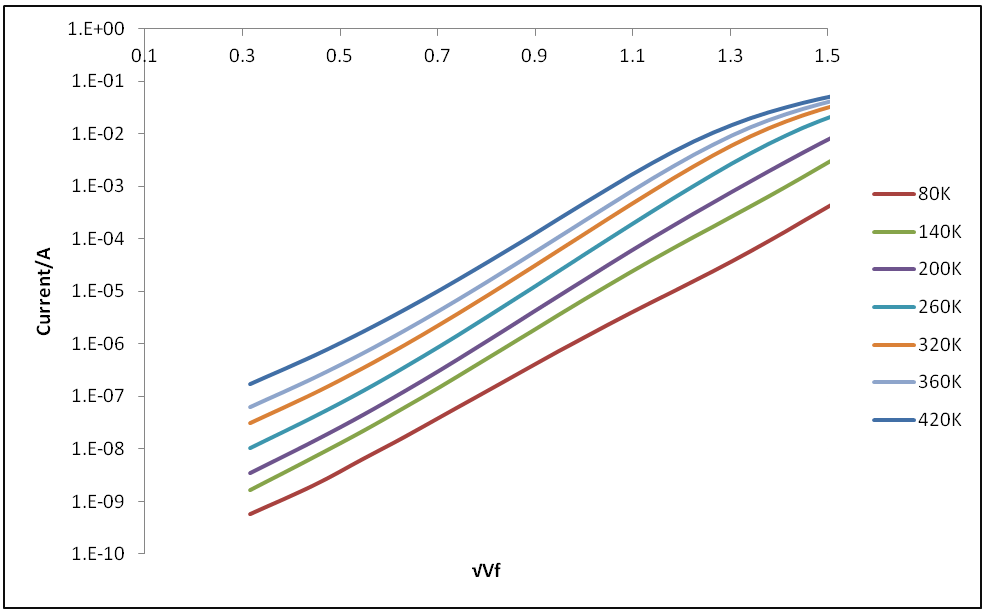

Figure 4-13: Replotted IV characteristic for Sample 2 at different temperatures.

Sample 2 has a higher indium content than sample 1, so is likely to have higher internal electric fields due to the increase in strain, so it follows that this

has a marked effect on carrier transport mechanisms.

Temperature Dependent I-V Characteristics

IV measurements were taken over a range of temperatures between 440K - 80K. This allows for a more comprehensive analysis of the mechanisms of carrier transport within the device.

The IV characteristics of sample 1, at different temperatures are shown in Figure 4-14. The slow turn-on of the device is indicative of a high series resistance, even at high temperature [149]. This originates from both the material itself, as well as the contact resistances. The p-contact resistance for this device was high compared to the control, so it is likely that both contribute to the high series resistance. A slow sub-threshold turn on is clearly seen at all temperatures indicating that carriers are being transported via defect states arising from the high indium content [10].

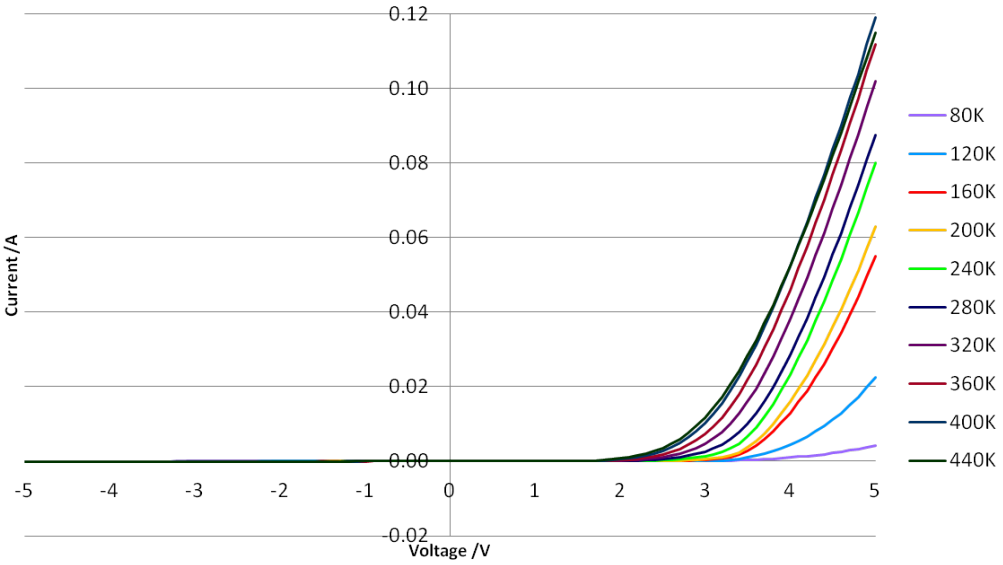

Figure 4-14: Temperature dependent IV characteristics of sample 1.

The IV characteristic shown for sample 2 in Figure 4-14 indicates there are several mechanisms for carrier transport in sample 2. This occurs for a number of reasons; the growth conditions leading to sub-optimal crystal quality, high indium content also giving rise to defects and the significant lattice mismatch giving rise

to high strain induced piezoelectric fields. It is highly probable that traps in the depletion region cause carriers to be generated which then recombine resulting in surplus current. In forward bias minority carriers recombine and at low applied biases this is a significant transport mechanism. The clear sub-threshold leakage is indicative of a parasitic pathways via defects. This sub-threshold turn on is especially pronounced at low temperature which indicates the presence of a parasitic diode. Carriers move via defect states which have lower barrier height than the primary device. This is seen in the IV characteristic as sub-threshold turn on. Figure 4-15 shows the equivalent circuit of the primary p-n junction (diode 1) and the parasitic diode (diode 2). The threshold voltage and area of diode 2 are less than that of diode 1.

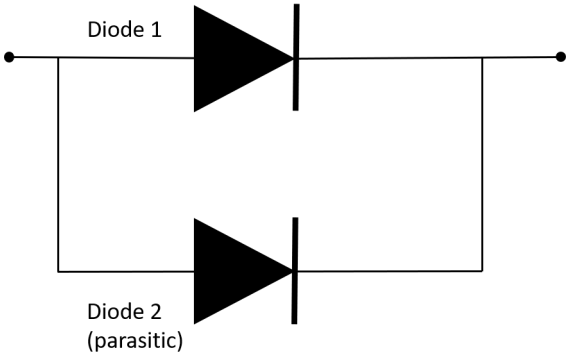

Figure 4-15: Equivalent circuit of a diode and a parasitic diode [10].

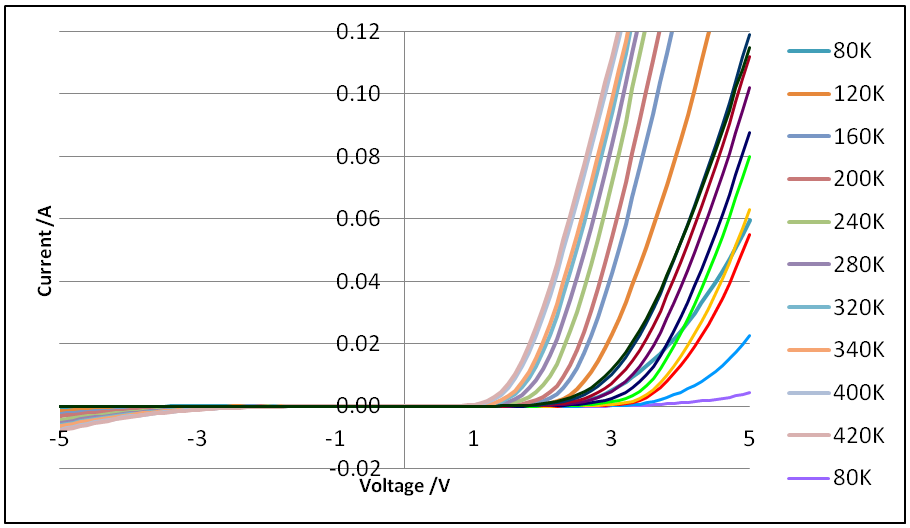

Figure 4-16: Temperature dependent IV characteristics of sample 2.

Plots of the reverse bias IV characteristic are shown in Figure 4-17 and Figure 4-18. These are plotted on semi-log scales as the reverse bias leakage current varies by several orders of magnitude as temperature changes and this method of plotting illustrates these most clearly. Both samples exhibited significant leakage, even at low temperature.

The reverse leakage current of sample 1 increases by an order of magnitude as the temperature increases, but does start to converge. The magnitude of this leakage at -5V is still considerably less than the forward current. This suggests that significant parasitic pathways do exist in this device.

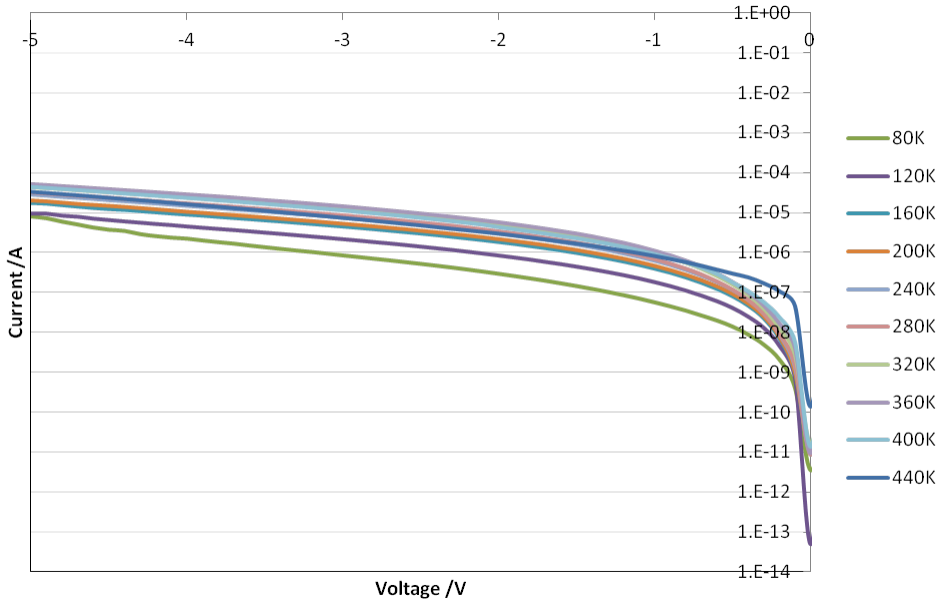

Figure 4-17: Temperature dependent reverse bias IV characteristics of sample 1 plotted on a semi-log scale.

The reverse leakage current of sample 2 increases by more than an order of magnitude as the temperature increases and there is less convergence than is seen in the previous sample. The magnitude of this leakage at -5V is in the order of mA - 10's of mA, which is similar to the operating current in forward bias. This suggests the presence of parasitic diodes which operate in the reverse direction to the main device. Further evidence of this was discussed earlier, in which light emission is observed from this device. However it does have a broad emission spectrum, suggesting it arises from defects in the material.

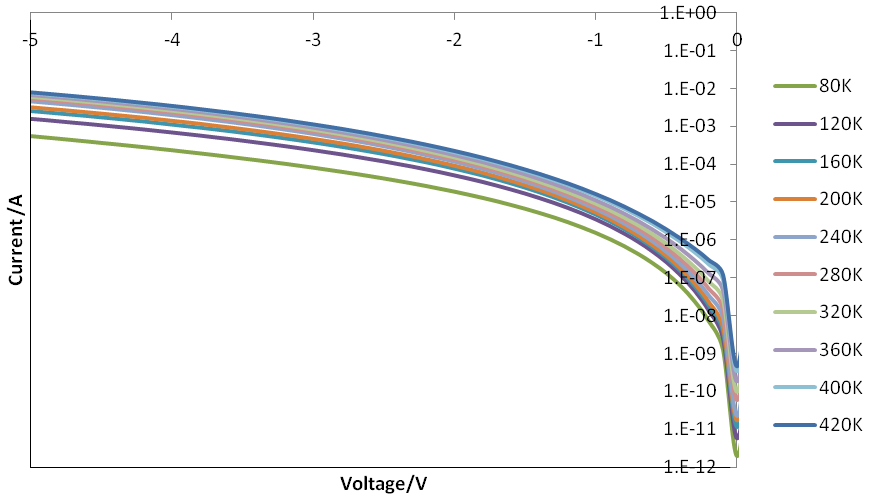

Figure 4-18: Temperature dependent reverse bias IV characteristics of sample 1 plotted on a semi-log scale.

The voltage at 20mA is then plotted as a function of temperature. As discussed previously sample 2 shows significant sub-threshold leakage. Both devices show there are two pronounced regions (highlighted by the red lines in Figure 4-19) and Figure 4-20) which are indicitive of different mechanisms dominating in the cryogenic region and then at higher temperatures. This is especially pronounced in sample 1.

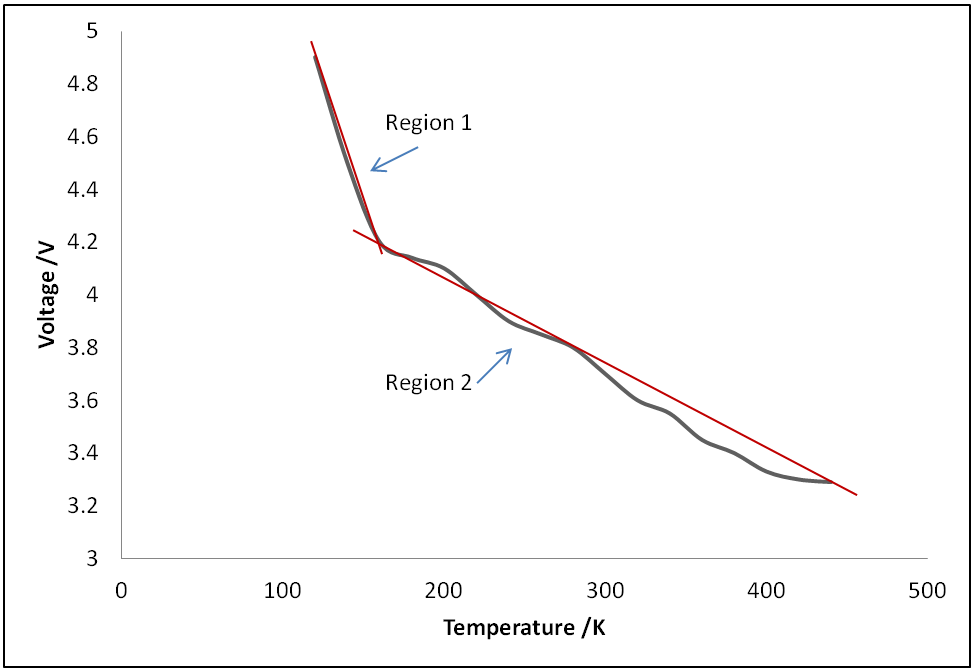

Figure 4-19: Variation of 20mA Voltage with Temperature for Sample 1.

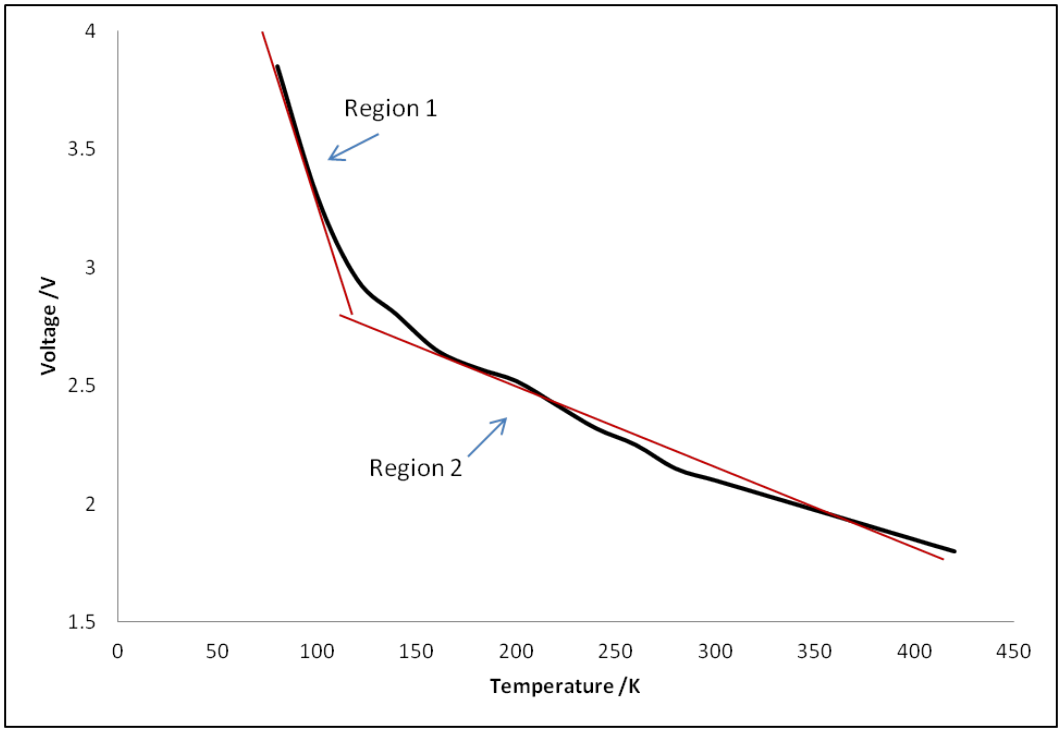

Figure 4-20: Variation of 20mA Voltage with Temperature for Sample 2.

The reverse leakage current and how it varies with temperature is plotted in both Figure 4-21 and Figure 4-22. There is less variation with sample 1 and the leakage begins to saturate. However sample 2 exhibits a linear relationship with no sign of saturation, indicating the presence of parasitic diodes operating in the reverse direction.

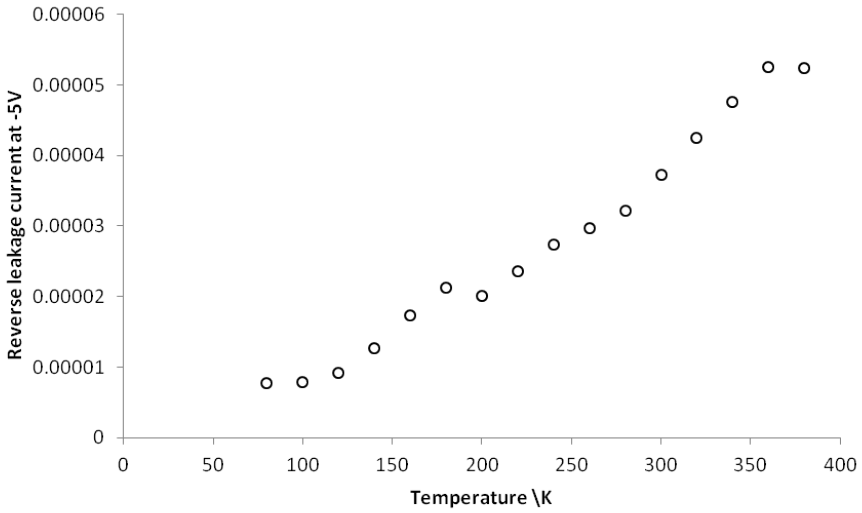

Figure 4-21: Reverse leakage current at -5V as a function of temperature for sample 1.

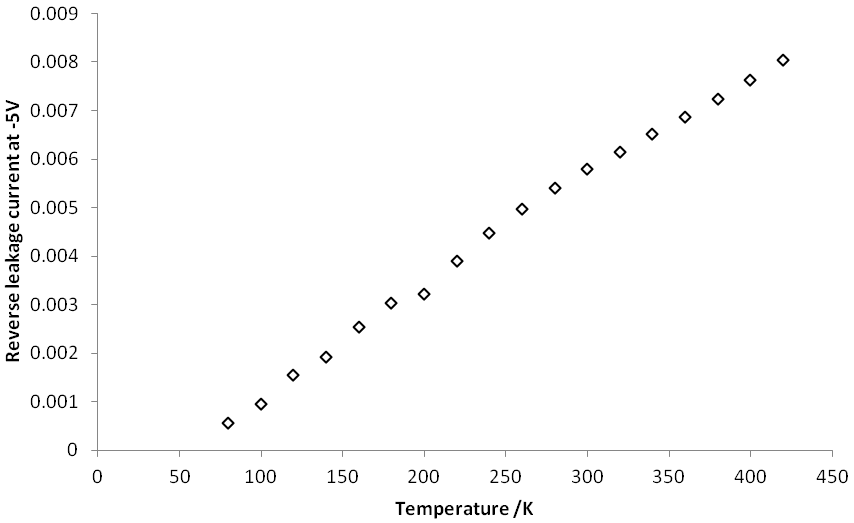

Figure 4-22: Reverse leakage current at -5V as a function of temperature for sample 2.

The temperature dependent measurements show that as indium content is increased the device behaviour rapidly deteriorates, with leakage mechanisms dominating in reverse bias and at sub-threshold voltages.

4.1.3 Optical Characteristics

Light output

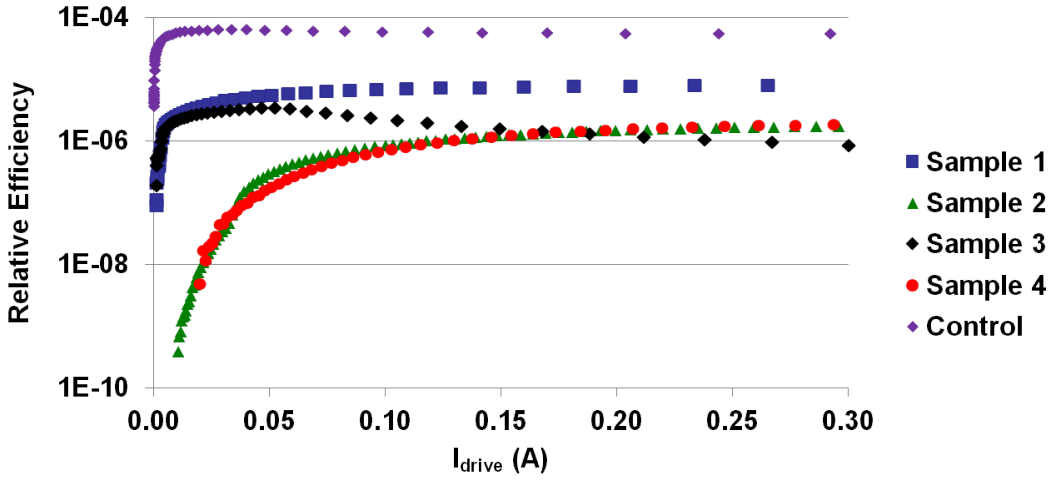

Figure 4-23: Relative efficiency against drive current. Samples measured were $500\mu m \times 500\mu m$.

Figure 4-23 shows the relative electrical to optical power conversion efficiency curves of the five epitaxial structures considered. The two lowest efficiency structures also show the lowest increase in efficiency for drive currents <50mA. The slope of this region of the efficiency curve is determined by the magnitude of the non-radiative recombination rate: the more shallow the slope (i.e the more gradual the rise in efficiency with injection current) the higher the non-radiative recombination rate. The leakage current in this current regime was also high for the lowest efficiency samples, indicating that SRH recombination centres, related to both the degraded I-V behaviour and low power conversion efficiency at low LED drive current.

Electroluminesence spectra

Figure Figure 4-24 shows for each structure the measured blue-shift in the peak wavelength with increasing drive current. The samples with largest blue shift (sample 2 and sample 4) were also the leakiest devices and had a greater In content (i.e. longer wavelength). The cause of this blue shift could be attributed to an increased strain as lattice mismatch increases due to the greater In content.

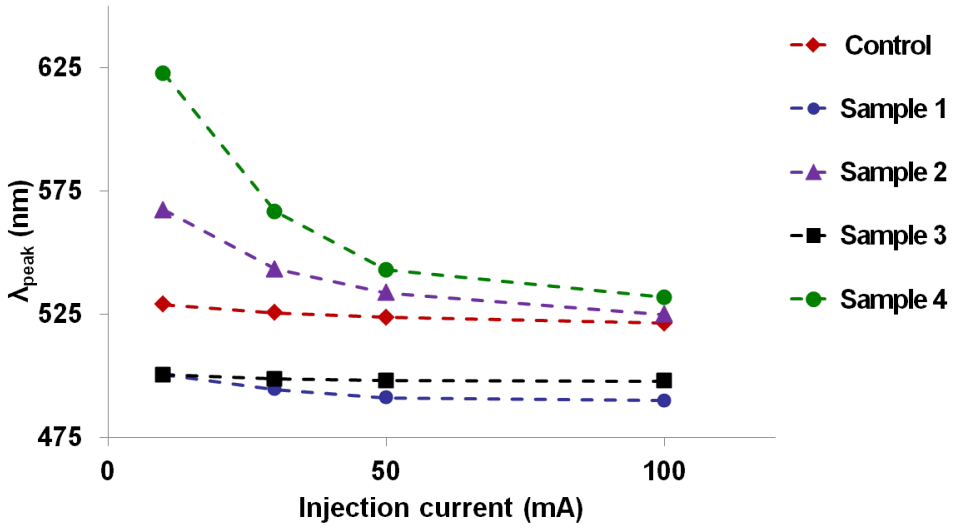

Figure 4-24: Blue shift of samples with increasing current.

A large QCSE will arise from the strain induced polarisation [150]. A large QCSE indicates that the electron and hole wave functions do not overlap significantly for injection currents <50mA, with the consequence that radiative recombination rate is lower in these samples, increasing the relative likelihood that non-radiative recombination rate is higher in these samples.

Parasitic emission has been reported in InGaN based LEDs. This undesired emission has been attributed to a number of causes such as tunnelling assisted radiative recombination [151] or radiative transitions related to defects [152].

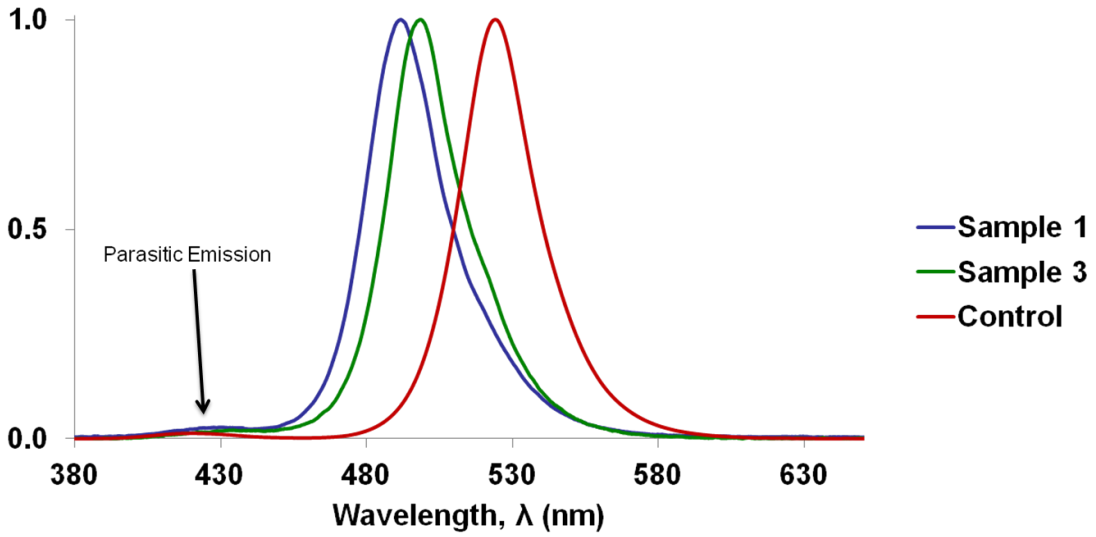

Figure 4-25: Normalised EL spectra with parasitic emission.

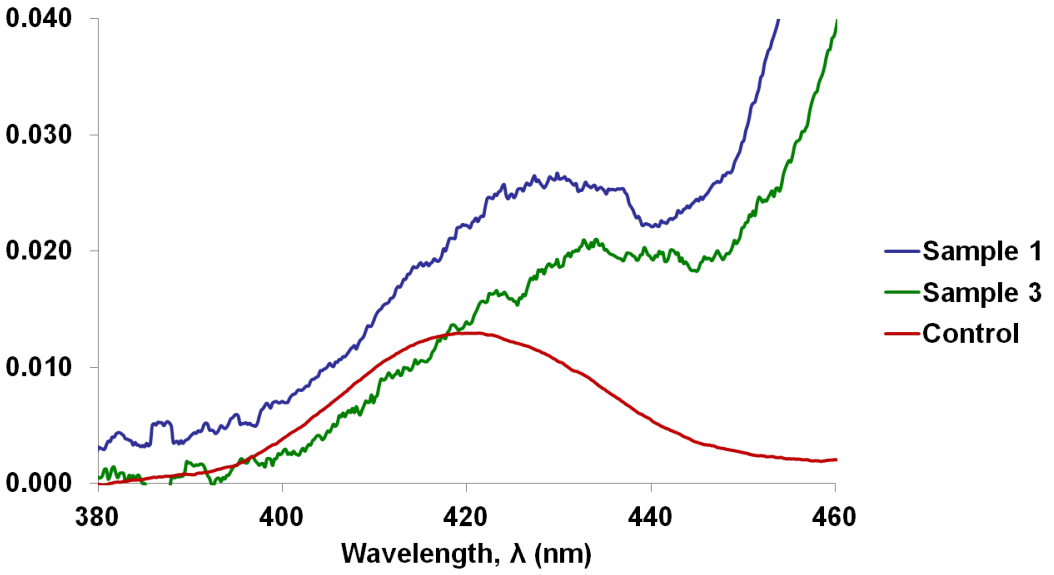

Figure 4-26: Parasitic emission observed in EL spectra

The emission observed in these devices is around 420nm, however it is weak and doesn't have a significant impact on the spectral purity. It is indicative of the presence of channels for recombination outside of the active area. Similar parasitic emission has been observed and attributed to transitions between the conduction

band and a Mg acceptor or a transition between a shallow Mg acceptor and a deep level donor. [153] [154]. This indicates that the parasitic emission observed in these devices arises from either the p-type capping layer or as a result of Mg diffusion into, or close to, the QWs. The latter is the more likely explanation if the EBL is effective.

Summary

A procedure for identifying the causes of low efficiency in green LEDs via detailed electro-optic characterisation has been implemented. The leakage current observed in the forward and reverse I-V characteristics of the LEDs can be correlated with increased non-radiative recombination that limits the peak electrical-to-optical power conversion efficiency. Further it can be demonstrated that epitaxial structures that cause a strong QCSE, specifically wider quantum wells result in an increase in the non-radiative recombination rate relative to the radiative recombination rate to impact on the peak power conversion efficiency. This strong QCSE also correlates with Poole-Frenkle emission and degraded device performance. As indium content increases more parasitic pathway are present and are detrimental to both the electrical and optical characteristics.

Chapter 5

Transparent Conducting Oxides

Improving the external quantum efficiency of LEDs is essential for most applications (as discussed in Chapter 1), so optimising the light extraction efficiency is a critical step in realising this. The use of transparent conducting oxides (TCOs) is of interest due to their superior transmittance and current spreading performance, compared to the standard Ni/Au layer used [155] [130]. However, as discussed in Chapter 2 making contact with p-doped GaN is inherently difficult. When deposited directly on to p-type GaN, both indium tin oxide (ITO) and Al-doped ZnO (AZO) form poor contacts. However, the use of thin metal layers (interlayers) deposited before such TCOs has shown to vastly improve the contact resistance.

This chapter presents the results of green LEDs (fabricated from commercial epitaxy) with different transparent conducting layers replacing the traditional Ni/Au layer.

The work contained in this chapter was presented at the European Materials Research Society Fall 2016 meeting and the International Conference on Nitride Semiconductors 2017.

SIMS and EBIC measurements were kindly performed by Dr. Juraj Priesol and Alexander Satka at the Institute of Electronics and Photonics in Slovak University of Technology in Bratislava.

Indium Tin Oxide (ITO) and Aluminium Zinc Oxide (AZO) layers were deposited by low temperature sputtering at Plasma Quest Ltd in Hook.

ITO and AZO were used, along with thin metal interlayers. A sample with a Ni/Au layer was also fabricated alongside as a control. The Ag/AZO sample

was omitted from SIMS and EBIC characterisation due its especially poor performance. The table below lists the samples fabricated.

Sample	Metal	Thickness(nm)
1	Ni/Au	5/5
2	ITO	315
3	Ni/ITO	1.2/315
4	Ag/ITO	1.5/315
5	AZO	450
6	Ni/AZO	1.2/450
7	Ag/AZO	1.5/450

5.1 Electrical Characteristics

This sections presents the results and discussion of the electrical characterisation of the device. These include both IV characteristics, sheet resistance and contact resistance measurements.

5.1.1 IV Characteristics

The IV characteristics of all of the samples can be seen in the figure below.

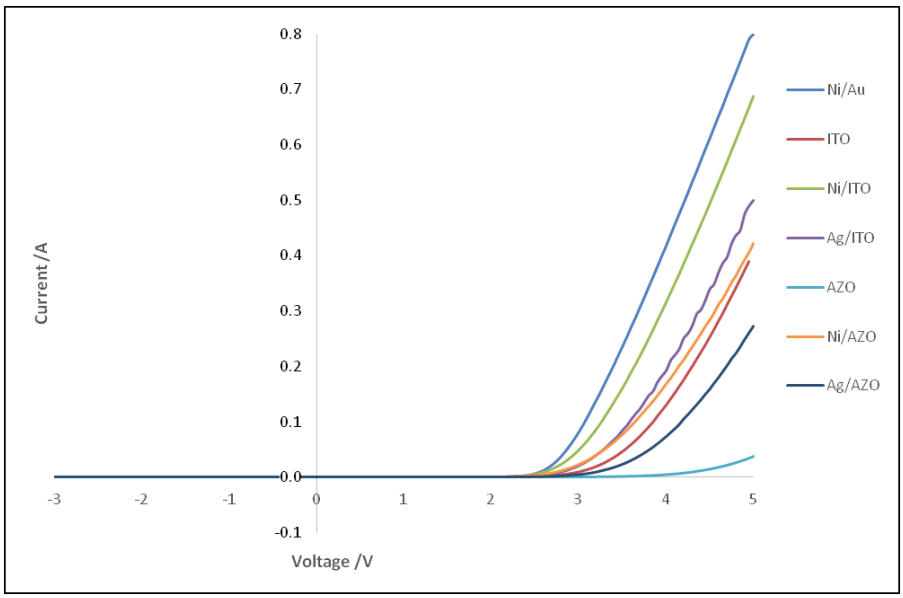

Figure 5-1: I-V characteristics of all samples.

.

The inclusion of interlayers causes a reduction in the turn on voltage with little change in reverse leakage. Whilst the Ni/Au sample still displays the best overall performance the Ni interlayer does show promise when used with either ITO or AZO. ITO does still outperform AZO, however this may be due to there being well established recipes for ITO sputtering, whereas AZO is still in its infancy. Optimisation of deposition may see AZO readily able to compete.

5.1.2 Characterisation of TCO layers

Each of the transparent contacts was deposited on glass in parallel with the deposition on to GaN. This allowed for four point probe measurements to be made for each contact. Results from this are shown in the table below. The inclusion of an interlayer under the ITO layer causes an increase in the resistivity of the layer, however the reverse is seen for the inclusion of interlayers with AZO.

Sample	Thickness(nm)	$R_{sh}(\Omega/\square)$	Resistivity (Ωcm)
Ni/Au	5/5	22.0	2.20×10^{-5}
ITO	315	10.1	3.18×10^{-4}
Ni/ITO	1.2/315	10.9	3.45×10^{-4}
Ag/ITO	1.5/315	14.4	4.55×10^{-4}
AZO	450	19.1	8.6×10^{-3}
Ni/AZO	1.2/450	10.1	1.28×10^{-3}
Ag/AZO	1.5/450	29.1	1.31×10^{-3}

5.1.3 Contact Resistances

The p-contact resistances are shown in the table below. Ni/Au has the lowest resistance by several orders of magnitude. The ITO samples again are better than the AZO samples. The contact resistance for the AZO without an interlayer could not be determined. The Ni interlayer is shown to be a better candidate than the Ag. This can be attributed to the formation of NiO, which is inherently p-type. There may also be some indium diffusion which will assist in the lowering of the contact resistance [156].

Sample	ρ_c (Ωcm^2)
Ni/Au	1.41×10^{-4}
ITO	1.51×10^{-1}
Ni/ITO	1.43×10^{-2}
Ag/ITO	4.53×10^{-2}
AZO	N/A
Ni/AZO	6.98×10^{-2}
Ag/AZO	2.59×10^{-1}

5.2 Optical Characteristics

This section presents and discusses the results from the optical characterisation which includes CCD images,light output measurements and transmittance measurements.

5.2.1 CCD Images

CCD images of the devices being driven at 10mA are shown and discussed here. AZO alone shows dark patches, along with very non-uniform emission. However the inclusion of an interlayer causes an improvement in the uniformity of emission. The sample with the Ag interlayer underneath the AZO does appear to have dark spots.

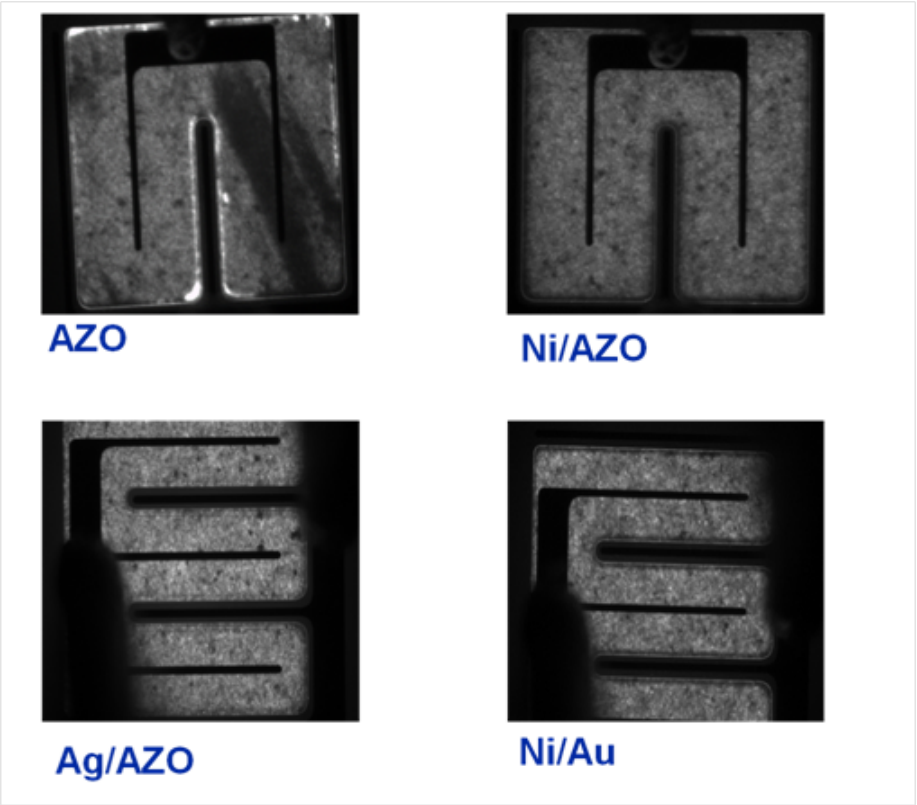

Figure 5-2: CCD images of AZO samples and Ni/Au sample at 10mA drive current. Some parts of bottom images are obscured by probes.

Samples with ITO are more uniform than those with AZO. The inclusion of an interlayer underneath the ITO layer results in only a small improvement in emission uniformity.

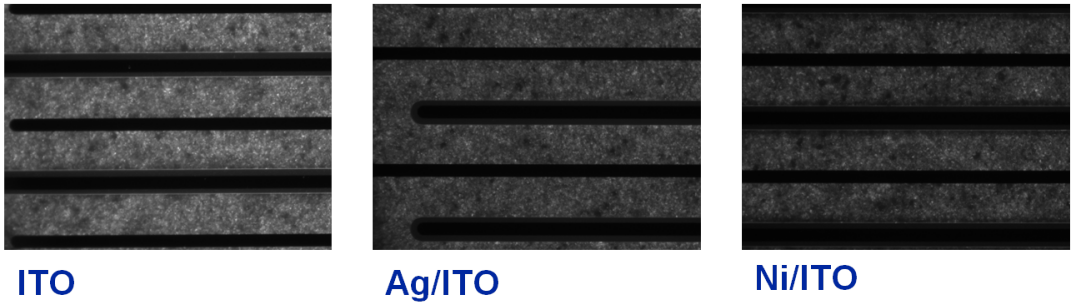

Figure 5-3: CCD images of ITO samples at 10mA drive current.

5.2.2 Efficiency

Light output measurement were taken using an integrating sphere. They are presented in this section in terms of wall plug efficiency. It should be noted that absolute measures of optical output cannot be taken so there may be some output losses that are not quantified.

The AZO sample employing the Ni interlayer achieves the highest efficiency. All samples exhibit some level of efficiency droop.

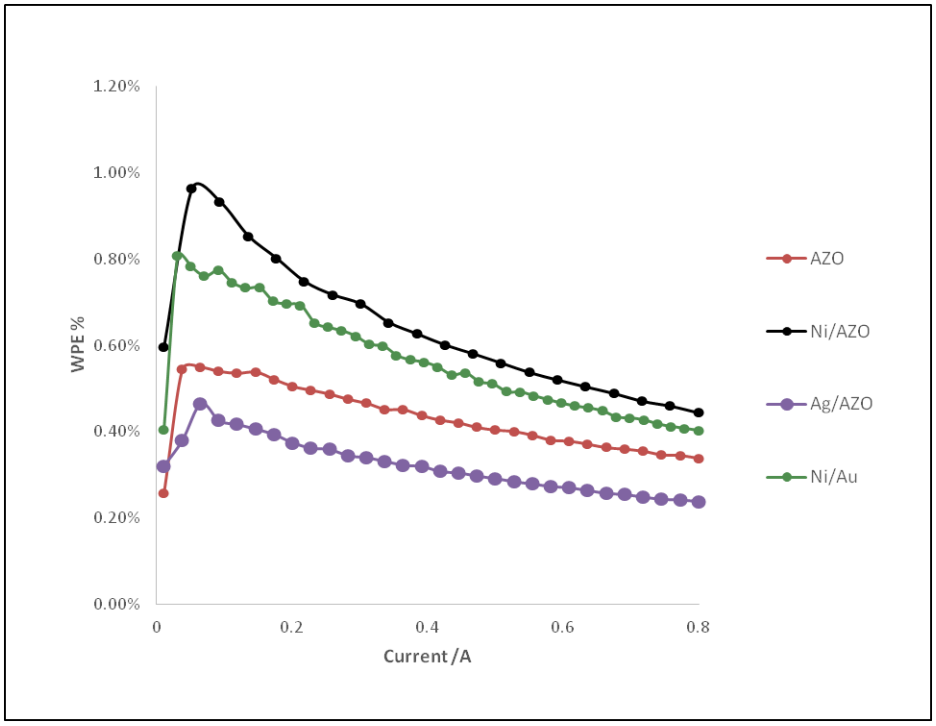

Figure 5-4: Wall plug efficiency of LEDs with AZO. Devices measured where $500\mu m \times 500\mu m$.

The wall plug efficiency of the ITO based contacts is shown below. Again the Ni interlayer gives greatest efficiency.

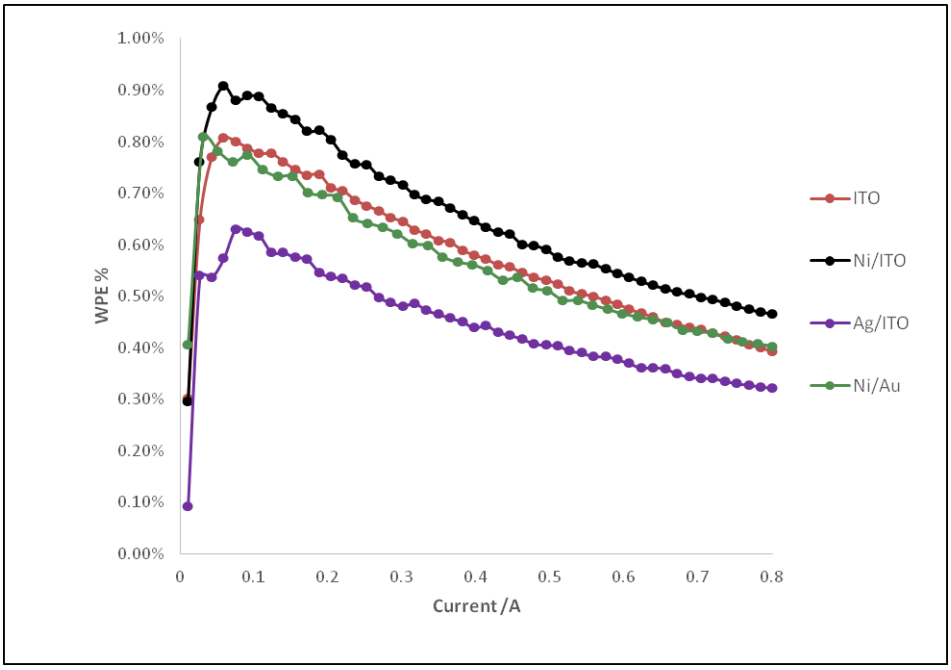

Figure 5-5: Wall plug efficiency of LEDs with ITO

It can be seen that the Ni interlayer is of most benefit, with Ag being detrimental to performance. The Ni/AZO sample is more efficient than the Ni/ITO sample. This is likely due to the enhanced transmission properties of AZO (discussed in the next section).

5.2.3 Transmittance

It is shown that the Ni interlayer does not have a significant effect on transmittance with peak transmittance at 520nm for the Ni/AZO sample. This is an improvement on the transmittance of Ni/Au which is approximately 74% at the same wavelength [157]. The inclusion of the Ag interayer impacts negatively. AZO has better transmittance properties than ITO. The cut-off in transmittance arises from the glass substrates.

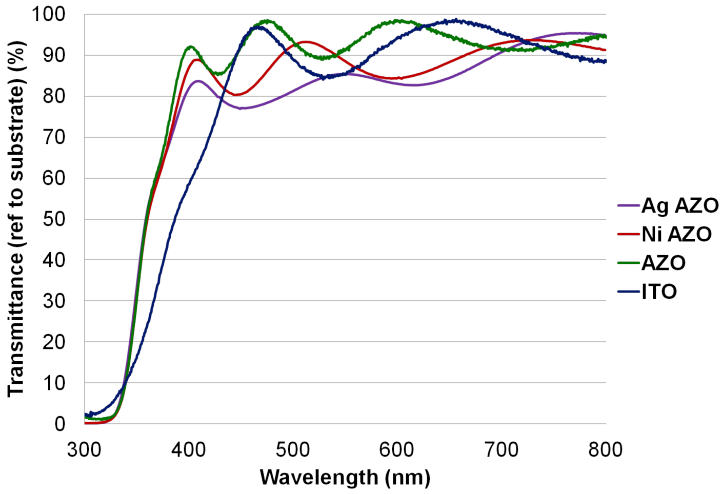

Figure 5-6: Transmittance of AZO samples and reference ITO

.

5.3 SIMS Characterisation

Secondary ion mass spectrometry (SIMS) measurements were used to demonstrate the formation of Ni / NiO and Ag /AgO interlayers and to determine their position in the contact structure. Additionally they provide contamination analysis.

Electron beam induced current (EBIC) measurements were used to detect any barriers or defects.

5.3.1 ITO

It appears that the thickness of the ITO is rather variable. However the depth distribution of the primary constituents (InO, SnO) is consistent across all the samples. SIMS measurements confirm that Ni, NiO, Ag and AgO are present at the GaN interface. Sharp Ni and NiO peaks are indicative that a thin layer has been formed i.e there is no indication of nanoparticles. It is observed that the NiO peak is stronger than Ni peak and Ni and NiO maxima are mutually shifted, with the NiO peak shifted toward ITO which indicates the Ni has partially oxidised.

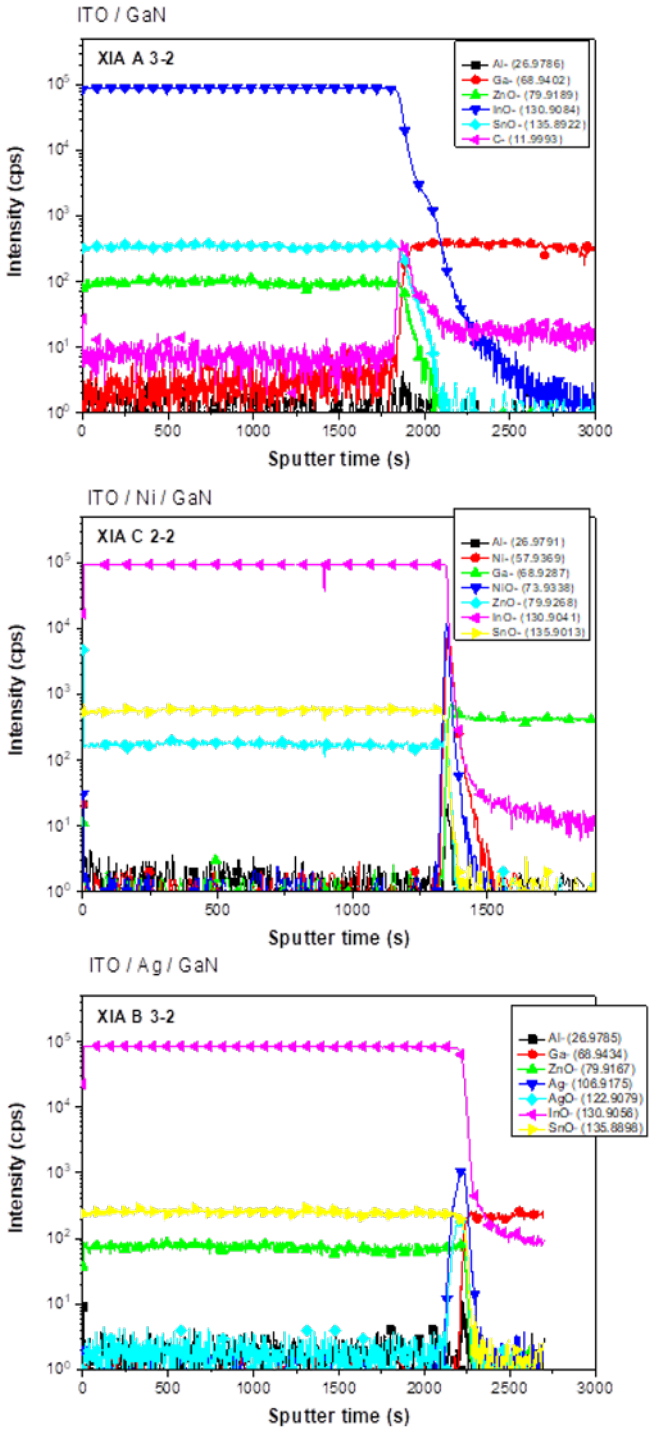

Figure 5-7: SIMS data for ITO/GaN, Ni/ITO/GaN and Ag/ITO/GaN samples.

The Ag and AgO signals peak at the same depth in ITO. With the Ag peak being stronger than the AgO but both possessing the sample shape which suggests the formation of Ag nanoparticles, as well as their partial oxidation. Predicted Ag-Ga is not seen.

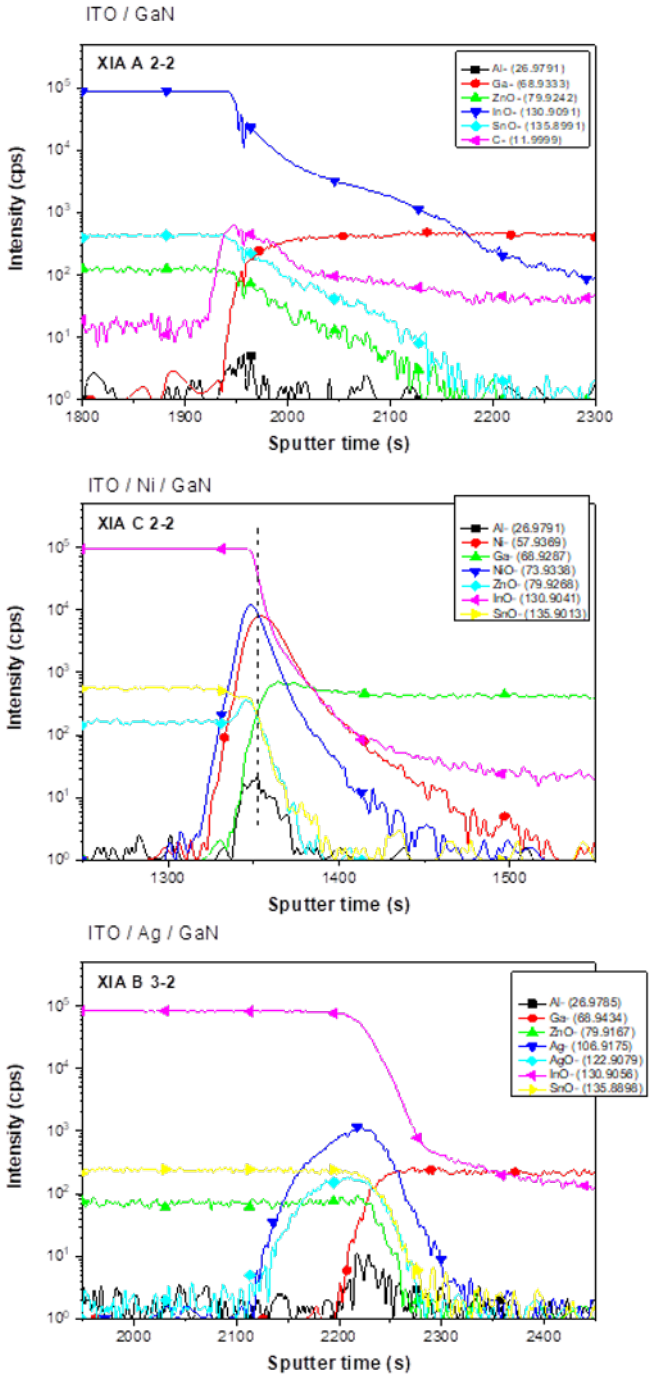

Figure 5-8: SIMS data for interface detail ITO/GaN, Ni/ITO/GaN and Ag/ITO/GaN samples.

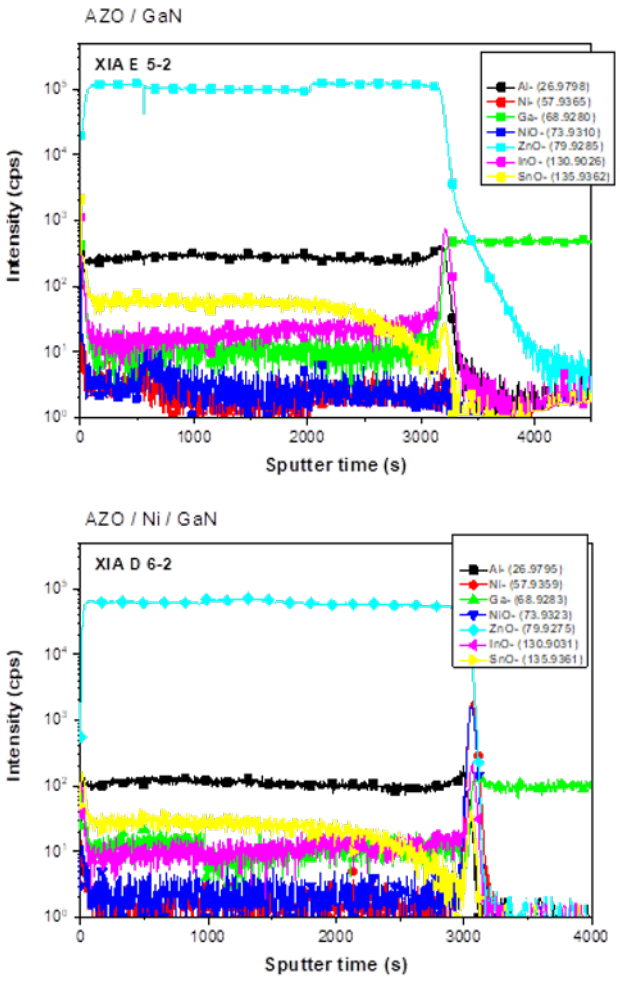

Figure 5-9: SIMS data for AZO/GaN and Ni/AZO/GaN samples.

5.3.2 AZO

The AZO has a more uniform thickness across the samples than the ITO samples. The distribution of the primary constituents, ZnO and AlO is also similar across the samples. As with the ITO sample, sharp Ni and NiO peaks are clearly detected at the interface. The peaks exhibit very similar intensities with the NiO shifted slightly towards the AZO.

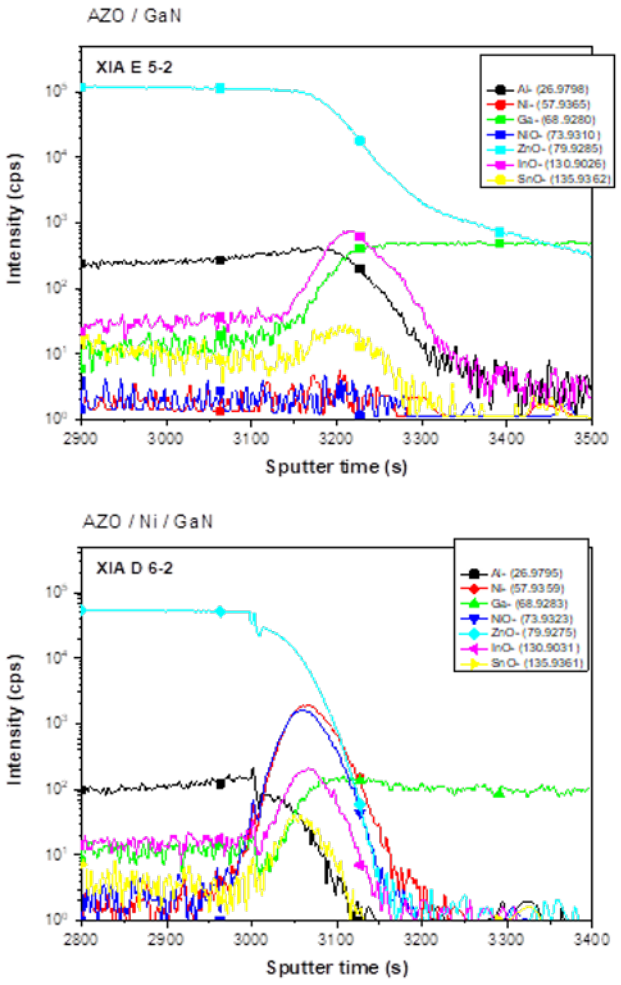

Figure 5-10: SIMS data for interface detail AZO/GaN and Ni/AZO/GaN samples.

5.3.3 Contamination

SIMs measurements allow for the determination of contaminants in the film.

Contamination of the ITO film

All the ITO samples were found to contain ZnO. It is likely that this comes from the deposition chamber, which is used for many different materials. Carbon was also detected at the ITO/GaN interface. This was least in the ITO on GaN sample and the highest with the Ni interlayer. This may arise from the additional

processing step required to deposit the interlayer. Si contamination is also found, and is thought to come from the Kapton tape used to secure the samples during ITO depostion. AgO was also found in the Ni/ITO sample.

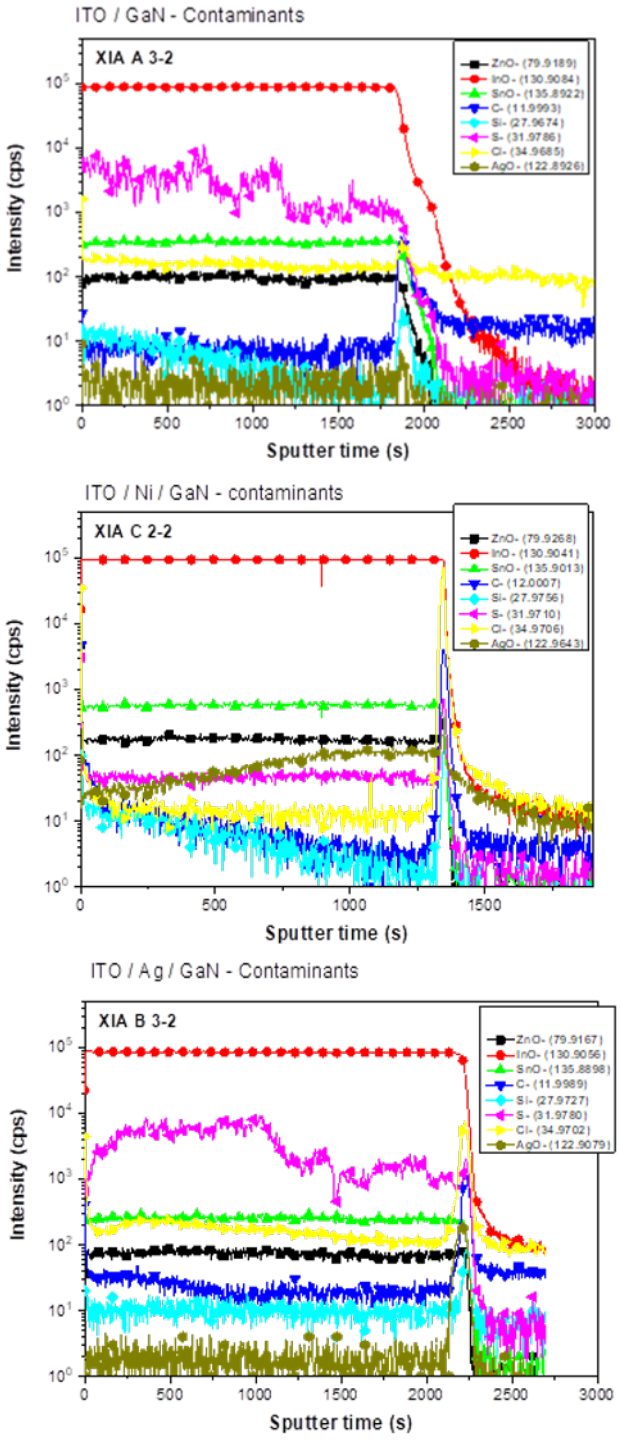

Figure 5-11: SIMS data showing contamination of the transparent contact in the ITO/GaN, Ni/ITO/GaN and Ag/ITO/GaN samples.

Contamination of the AZO film

It was found that there was a very high concentration of Cl at the AZO/GaN interface. This may arise from the mesa etching step. Future fabrication should include a KOH to remove this. This may further help to improve the contact properties. As well as Cl, C, S, and AgO, contaminants were found in the AZO in quantities that were not negligible. Improved deposition techniques will allow the number of contaminants to be reduced and the AZO properties to be improved. As with the ITO, Si contamination is found with its origin believed to be from the Kapton tape used to secure the samples during film deposition.

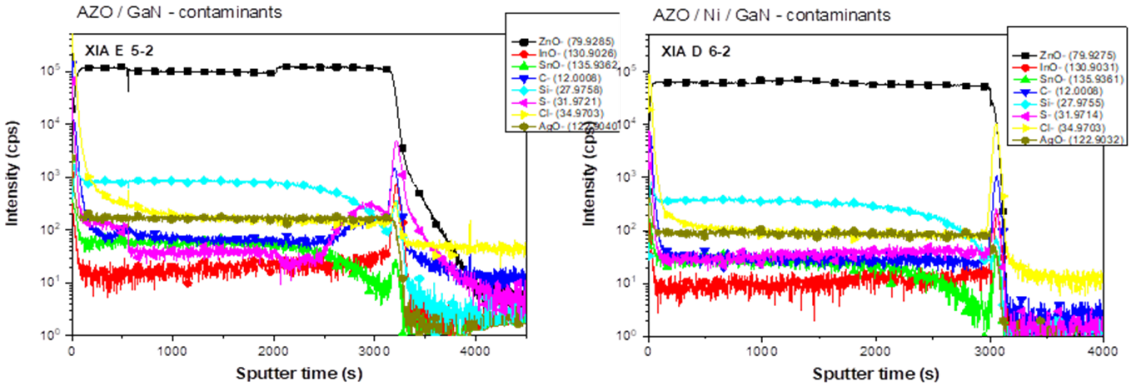

Figure 5-12: SIMS data showing contamination of the transparent contact in the AZO/GaN and Ni/AZO/GaN samples.

5.4 EBIC Characterisation

Pulsed EBIC measurements allow for the visualisation of the effects related to the dynamics within the device structure, which in this instance relate to the current spreading, as well as the trapping and emission of carriers at defects.

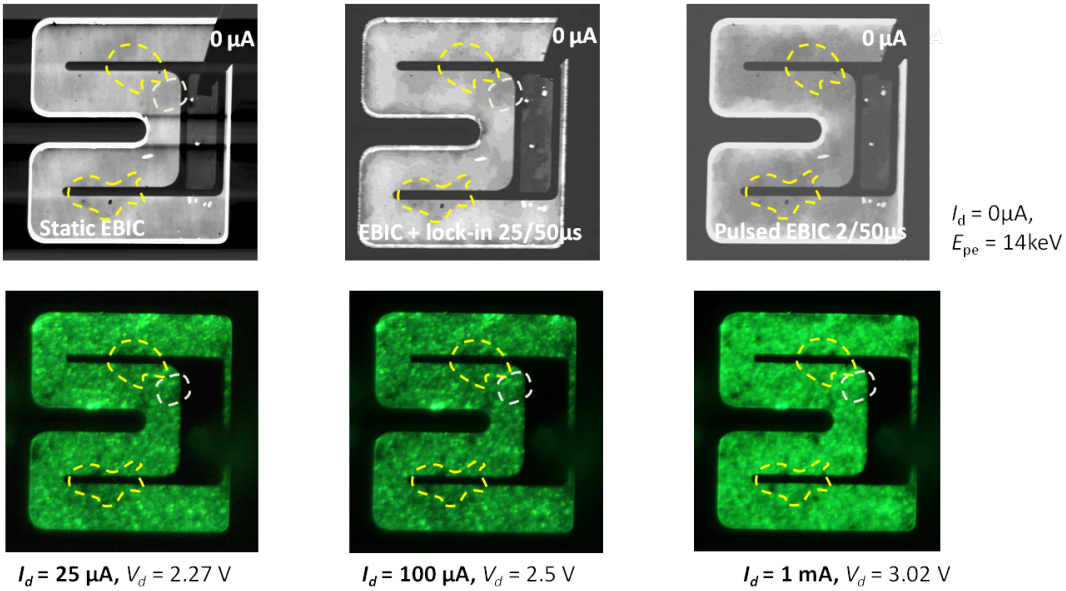

Figure 5-13: Correlation of EL and EBIC maps measured in various modes for ITO/GaN sample

Due to the high resistance of the p-type layer not covered by AZO, the built in electric field in the space charge region at the edge of the mesa is higher relative to forward polarised structure. This results in carriers collecting at the mesa edge and the electroluminescence becoming lower. The inclusion of the Ni interlayer suppresses this effect.

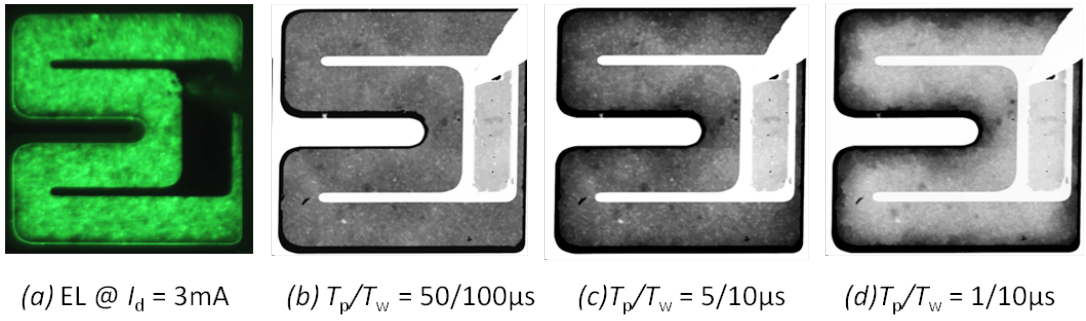

Figure 5-14: Comparison of EL measured at 3mA (a) and inverted pulsed EBIC measured at different pulse conditions at Ebeam = 20keV, for the AZO/GaN samples

EL and EBIC comparison demonstrates the enhancing role of the AZO with

the Ni interlayer on current spreading. The marked areas are defects / device imperfections in the structure which are seen in both EL and EBIC. Results also suggest inhomogeneities in MQW region and p-GaN layer. The EBIC measurements further support the use of thin interlayers in combination with AZO as a promising candidate for indium-free transparent contact technology.

5.5 Summary

The employment of an interlayer causes a decrease in the turn on voltage and improved light output, when compared with AZO only. AgO and NiO are formed at the interface, causing an increase in the hole concentration, helping to overcome the inherent issues with decreased hole concentration in p-type GaN. The presence of these is confirmed by SIMS measurements. The presence of such layers increases the hole concentration due to their interaction with the GaN surface. Various compounds are formed at the interface, which produce Ga vacancies which act as acceptors (and thus increase the hole concentration) [158]. Inclusion of interlayers gives improved current spreading and this is further confirmed from the EBIC results. Interlayers significantly lower the contact resistance compared with samples negating one, although optimisation is required to lower this further. This could include a thicker interlayer or annealing interlayer before and/or after TCO deposition.

Interlayers could provide a means of using AZO to make good contact with p-GaN, without suffering from poor transmittance, and could be a candidate for replacing Ni/Au and ITO based contacts.

The Ni interlayer shows the most promise and further work on this is discussed in the next chapter.

Chapter 6

Interlayer study

Al-doped ZnO has been proposed as an alternative to both Ni/Au and ITO-based transparent contacts for GaN LEDs. Improved transmittance has been observed, which results in improved light output [130]. The rarity and expense of Indium is also a driver in looking for cost effective, sustainable ITO alternatives [159]. AZO alone makes poor contact with p-type GaN, however the inclusion of a thin metal interlayer has shown promise. Ni interlayers have been demonstrated to improve the specific contact resistance (Chapter5).

This chapter presents the results on LEDs with Ni interlayers placed underneath a layer of AZO. The anneal conditions of the Ni interlayer were varied. Additionally a further sample was fabricated to determine if a marginal increase in Ni thickness would impact on the quality of the device. All samples were annealed for 5mins at 500C in either O_2 or N_2. The thickness of the AZO was approximately 450nm. A control sample was fabricated and employed a Ni/Au layer annealed for 5mins at 500C in an O_2 atmosphere. The table below details the samples discussed in this chapter.

ITO and AZO layers were again deposited by low temperature sputtering at Plasma Quest Ltd in Hook.

Unfortunately some issues occurred whilst processing these devices. These issues only impacted on green emitting devices. A more detailed explanation of these issues is presented below.

Sample	Ni thickness	Anneal
1	1nm	no anneal
2	1nm	O_2
3	1nm	N_2
4	3nm	O_2

6.1 Electrical Characteristics

The IV characteristics of the devices can be found in the figures below. Unfortunately issues relating to the AZO layers (see 6.3) meant that contact resistances for the variable anneal samples could not be determined. However the IV characteristics show that annealing the interlayer before AZO deposition is a means of changing the electrical characteristic.

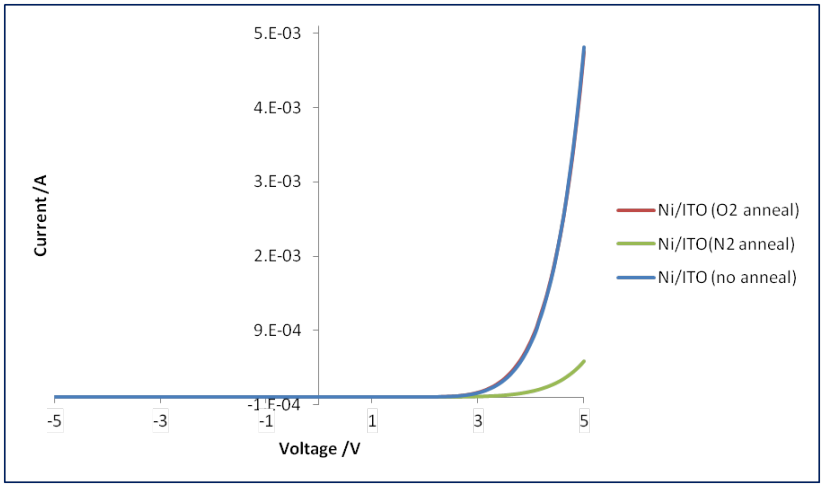

Figure 6-1: IV characteristic at different anneals. Replotted on semi-log scale below.

Whilst the sample annealed in O_2 and the sample which was not annealed appear to have very similar IV behaviour, replotting on a semi-log scale shows an improvement in the device behaviour. This replotting makes the behaviour of each sample more clear, as two of the samples shown in Figure 6-1 (red and blue) superpose each other. Additionally any anneal shows an improvement in the reverse leakage when compared with no anneal.

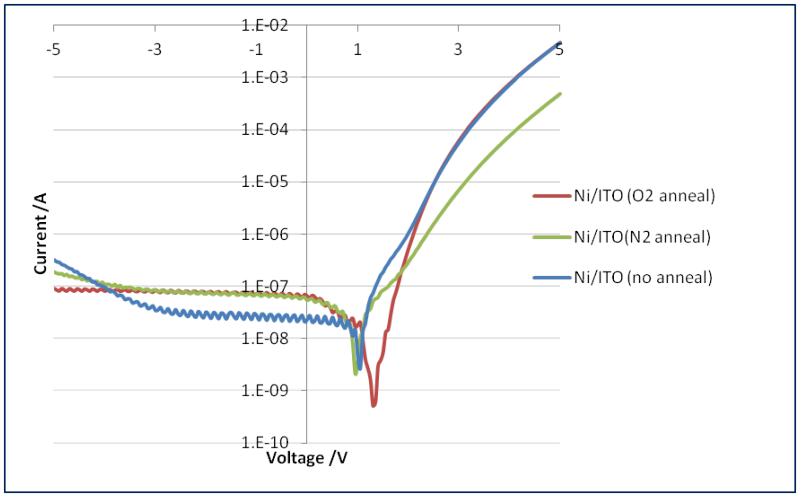

Figure 6-2: IV characteristic at different anneals plotted on a semi-log scale.

The sample annealed in O_2 gave the best performance, so a further sample was prepared with a slightly thicker 3nm Ni interlayer, which was also annealed for 5mins in O_2 at 500C. A further control sample was also prepared with the standard 5nm/5nm Ni/Au layer deposited and annealed in the same way. 450nm of AZO was then deposited on both these samples.

Interestingly the 3nm Ni/AZO gave the best IV characteristic. There was no difference in the reverse leakage current. The contact resistance of the 3nm Ni sample was found to be $4.2 \times 10^{-3}\Omega cm^2$ and the Ni/Au sample was $7.0 \times 10^{-3}\Omega cm^2$. The 3nm Ni sample also has better transmittance the Ni/Au sample.

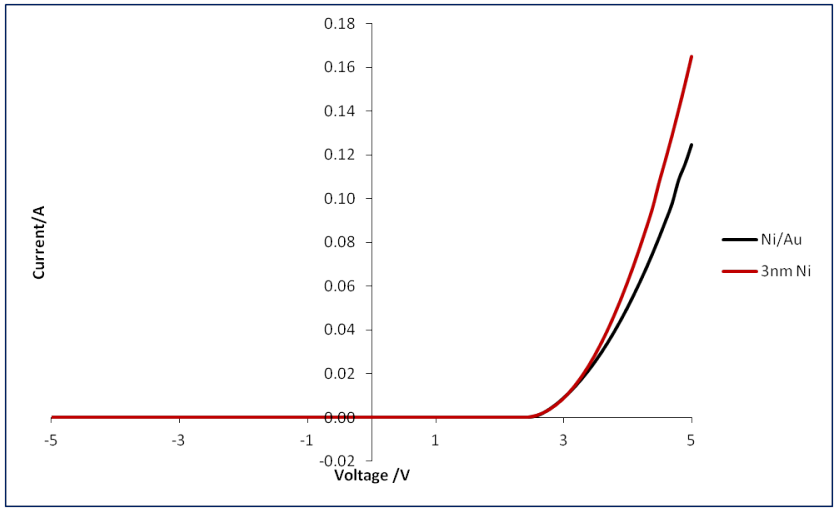

Figure 6-3: IV characteristic of samples with Ni/Au and 3nm Ni interlayers.

6.2 Optical Characteristics

The wall plug efficiency (WPE) is plotted against current. As is usual for nitride LEDs, efficiency droop is observed. The sample with the N_2 anneal has the highest peak efficiency but this does drop off more rapidly than the sample annealed in O_2. Both of the annealed samples have a higher efficiency than the sample with no anneal.

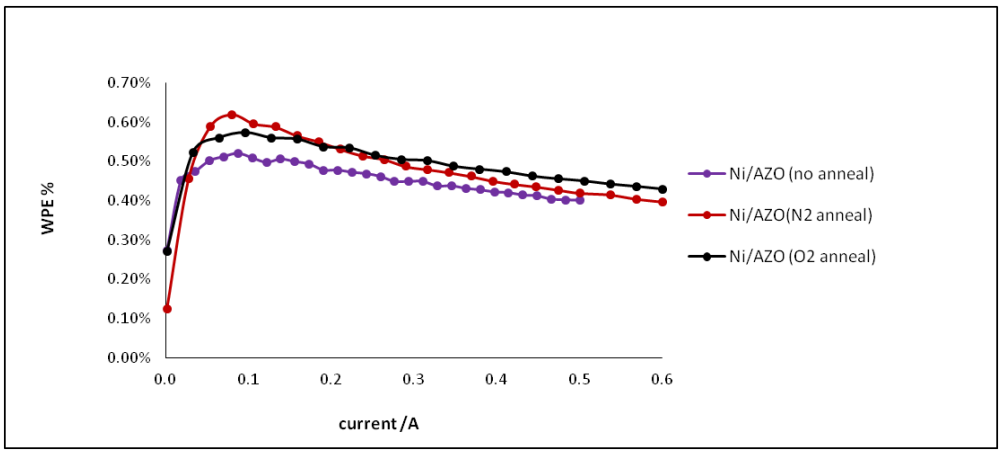

Figure 6-4: Wall plug efficiency of different anneals.

CCD images were taken to compare the uniformity of emission from the 3nm Ni sample and the Ni/Au sample. Whilst there are several dark patches, this does

not vary between samples. This suggests the dark patches arise independently of the interlayer.

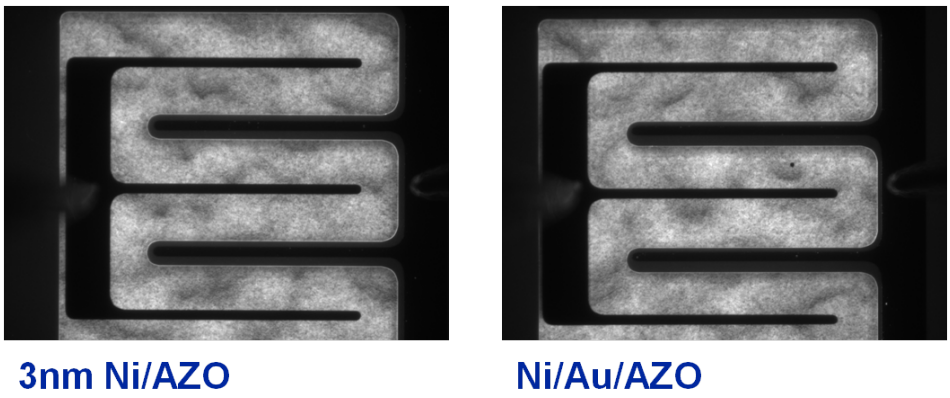

Figure 6-5: CCD images of 3nm Ni/AZO and Ni/Au/AZO operating at 0.4mA.

The wall plug efficiency was also determined and plotted for the thick Ni and Ni/Au samples. Again the 3nm Ni sample out performed the Ni/Au. When compared with the thinner Ni samples, the thicker sample also achieves an improved result.

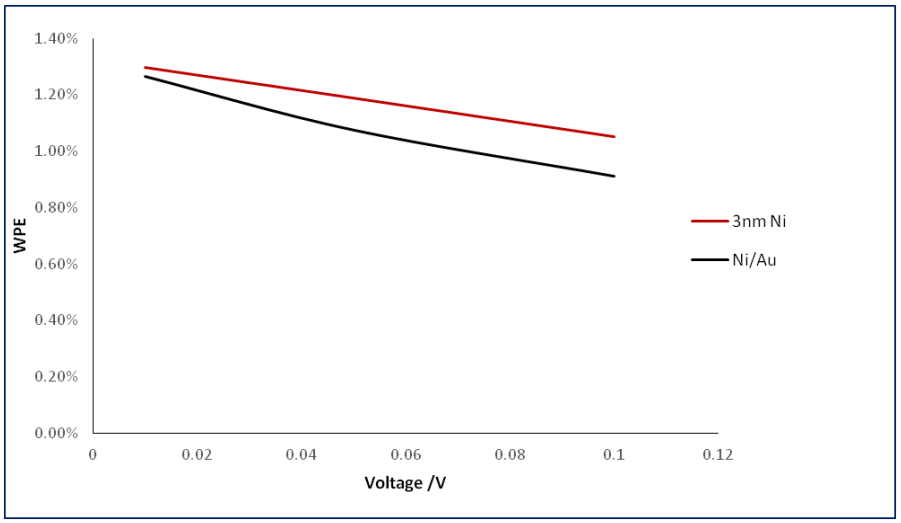

Figure 6-6: Wall plug efficiency comparison with Ni/Au and 3nm Ni interlayer.

6.3 Effects of film quality

The quality of the transparent contact film is of critical importance. This section will demonstrate the effect of degraded films and their impact on device performance.

The devices discussed here were fabricated from commercial green epitaxy. All interlayers and AZO were deposited by the methods outlined previously.

It was apparent that post-processing an unusually high number of the green devices had failed. It was initially postulated that issues were arising due to the post AZO deposition processing. This was shown not to be the case when a number of devices were fabricated from blue epitaxy. All interlayers and AZO were deposited on the same runs.

6.3.1 Electron Microscopy

SEM and FE SEM imaging was used to look at the sample surfaces. Striking differences can be seen between the AZO deposited on green epitaxy (see Figure 6-7) and that deposited on the blue epitaxy (see Figure 6-8). Both samples have Ni interlayers between the p-GaN layer and the AZO. The Ni for both samples was deposited at the same time. The AZO was deposited on the same run and both samples underwent the same processing through to finished devices.

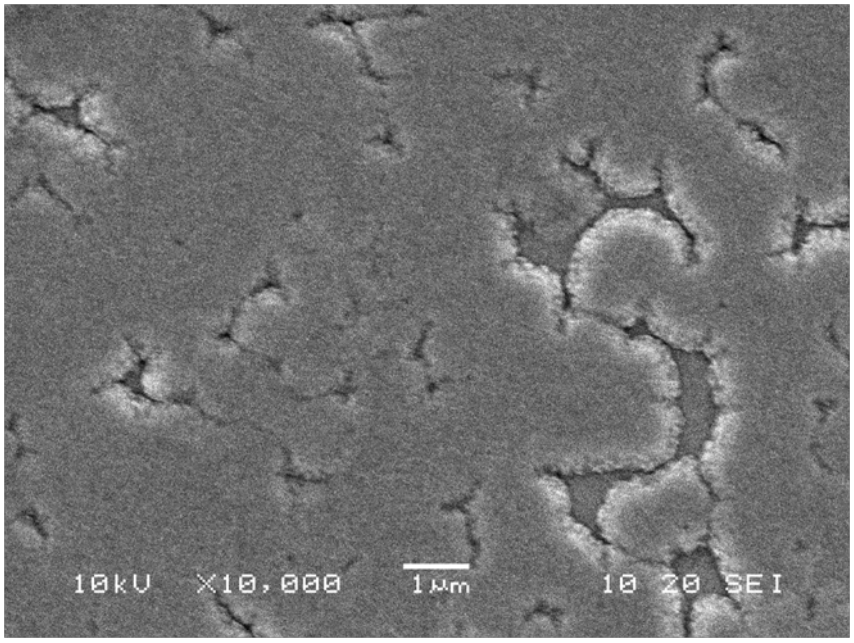

Figure 6-7: SEM image showing 200nm deep trenches in AZO deposited on green LED.

Large trenches can clearly been seen in the AZO on Figure 6-7. EDX measurements show that all of the material is AZO.

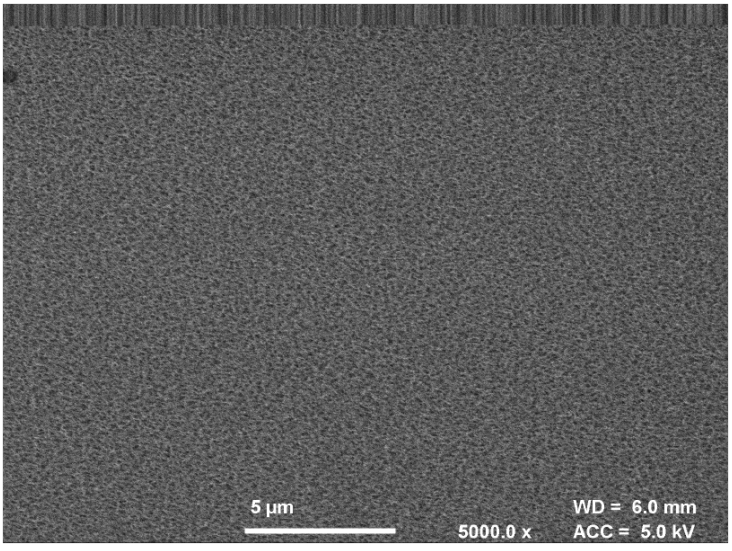

Figure 6-8: FE SEM image showing surface of AZO deposited on blue LED.

No trenches are observed in the AZO deposited on the blue epitaxy shown in Figure 6-8 AZO was also deposited on top of glass slides and is very similar in

appearance to that seen in Figure 6-8. Images of the uncoated LED (not shown) show smooth, clean, uniform surfaces, suggesting that surface features did not influence the deposited films.

6.3.2 Atomic Force Microscopy

Atomic force microscopy was used to characterise the AZO discussed in the previous section. In particular it was used to ascertain how significantly the AZO changed when deposited on the green epitaxy.

Green LED

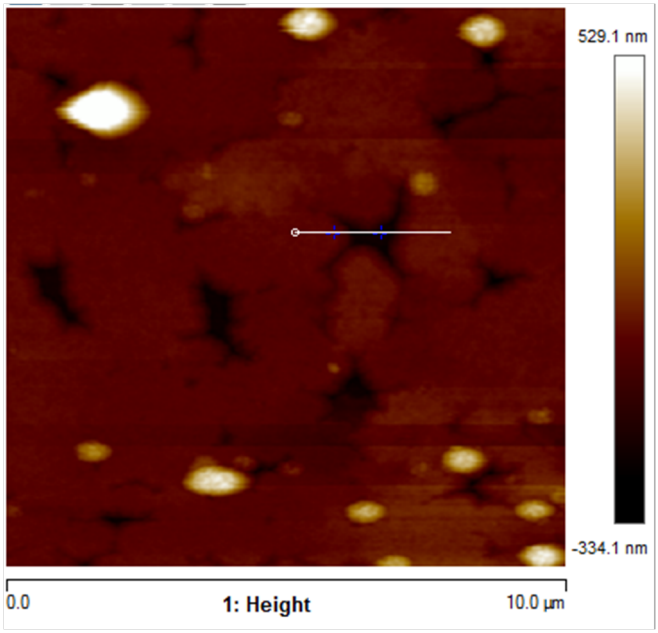

Figure 6-9: 2D AFM of AZO showing 200nm deep trenches.

The large trenches shown in Figure 6-9 were found to be in the region of 200nm deep, almost half the depth of the layer. They were often more than 1um across.

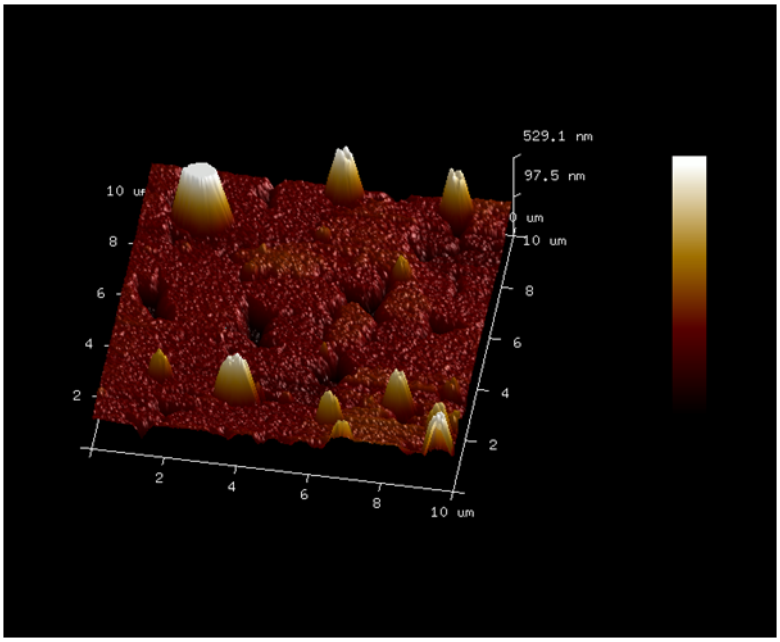

Figure 6-10: 3D AFM of AZO showing 200nm deep trenches. The vertical scale is 550nm.

A 3D plot shown in Figure 6-10 shows not only are there very large trenches but also large lumps of material. These spots were identified as AZO with EDX, however this is probably not a sensitive enough technique to quantitatively say this.

Blue LED

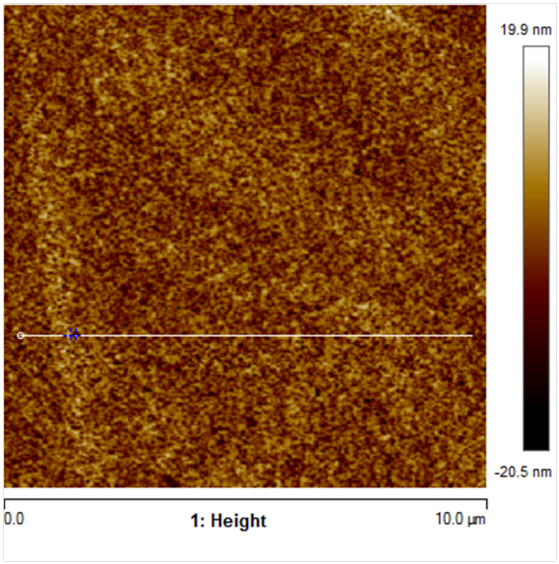

Figure 6-11: 2D AFM of AZO showing 20nm roughness.

The AFM data for the AZO deposited on the blue epitaxy is shown in Figure 6-12. The surface roughness is determines to be approximately 20nm and is uniform across the sample. It is clear from the 3D plot that there is little variation across the sample, and certainly no significant features.

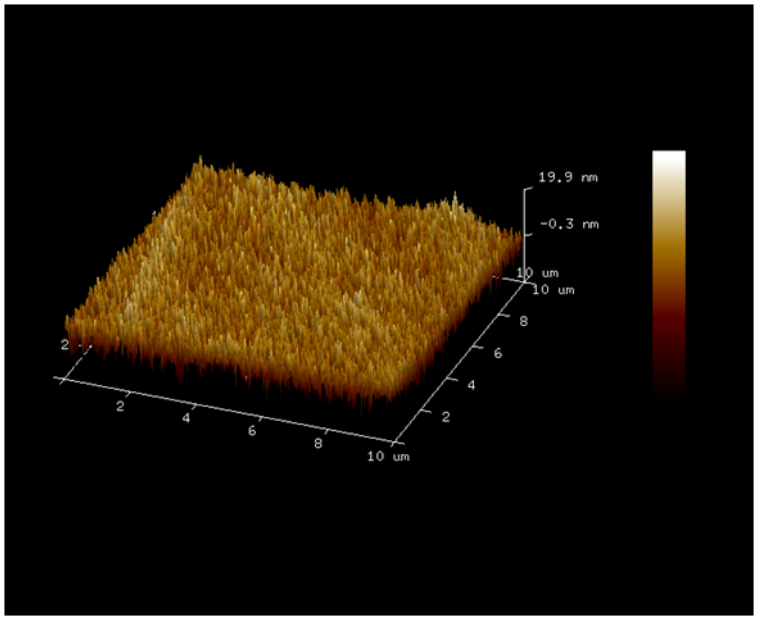

Figure 6-12: 3D AFM of AZO showing 20nm roughness.

Whilst the cause of the trenches is unknown, it can be concluded that this is an issue specific to the green epitaxy. Such trenches occurred across all of the green samples and none in the blue samples. The AZO was deposited in 3 different runs, but the issue arose in all of these. From the information available the epitaxial structure of both samples is nominally the same with the exception that the green sample has an InGaN capping layer. It is possible that there may be some indium segregation and this is the source of these features, but that is high speculative. Further measurements such as SIMS, EBIC and XPS would be beneficial in achieving a comprehensive conclusion. Such experiments would prove helpful in the further development of improved green devices.

6.4 Summary

Several conclusions can be drawn from this work. The inclusion of an anneal step before AZO deposition enhances the wall plug efficiency of the device. Overall an anneal in O_2 is of most benefit. This is likely due to the creation of NiO which increases the hole concentration (the mechanism for this is discussed in the previous chapter). Using a slightly thicker Ni layer improves the efficiency further. This provides strong evidence that the inclusion of an interlayer is a

means of enhancing the contact performance and also makes the possibility of realising a commercially viable In free transparent contact a reality. Ensuring the AZO is of good quality is incredibly important, as problems in this layer cause significant device failure. Further work is needed to characterise the nature of the problems observed in this work, especially as they seem to be specific to green epitaxy.

Chapter 7

Ultraviolet MIS LEDs

All work in this chapter was carried out out between Imperial College London and University of Bath. Sputter deposition, most of the device fabrication, CV measurements, x-ray diffraction and simulation were performed by Chen-Sheng Lin at Imperial College. PL, EL, LI and IV measurements were performed by the author at the University of Bath. Analysis and writing were shared between Chen-Sheng Lin and the author. All results are presented so as to present a complete discussion. The author would like to reiterate thanks to Chen-Sheng and his supervisor, Michelle Moran, for their invitation to participate in this work and for the fruitful collaboration.

The Minamata convention on mercury is an international treaty which aims to protect both humans and the environment against the detrimental effects of mercury. Mercury is a critcal material in traditional ultraviolet (UV) lamps, which are used in a diverse range of applications. Due to such protocols , UV LEDs have gained significant attention, as they offer not only an alternative to mercury vapour lamps but one that has the potential to be considerably more efficient(and thus less of a drain on resources) [160]. Whilst the technology surrounding GaN based visible LEDs has improved dramatically in recent years, shifting the emission wavelength outside of that region has proved problematic. In order to adjust the bandgap to a suitable region GaN must be alloyed with aluminium (Al), to form AlGaN. Similar to the problems of increasing In content in InGaN based devices, increasing Al (to shorten the emission wavelength), results in a significant drop off in efficiency. There are also significant issues regarding

the p-type doping of AlGaN, the absorption of this p-type layer and high defect densities. The latter are particularly problematic for the typically complicated device structures employed to optimise efficiency.

This chapter will present and discuss results related to an alternative device structure which directly circumnavigates some of the greatest challenges faced in the realisation of this powerful technology [161]. Here a metal-insulator-semiconductor structure is employed, completely omitting the p-type layer, and thus the inherent issues that come with that. The structure also avoids complicated device structure, something which is especially helpful when it comes to characterising (and thus understanding) the device behaviour and lends itself to more robust optimisation.

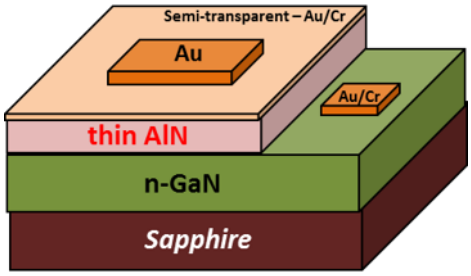

Figure 7-1: Schematic of the MIS LED structures discussed in this section [161]

The devices all employ a structure which consists of a thick n-GaN layer grown on a sapphire substrate. A thin AlN layer was deposited on top of the n-type layer, with a semi-transparent current spreading layer. Metal contact pads are deposited on the n-GaN and the transparent contact. A schematic can be seen in Figure 7-1.

7.1 MIS structures emitting at 365nm

Initial work focused on determining a suitable thickness for the AlN insulating barrier layer. Four samples were prepared with varying insulating layer thicknesses; 3nm, 5nm, 10nm, 20nm. These layers were deposited on top of the n-AlGaN layer by RF sputtering. Ion milling was used to define a $0.45mm^2$ mesa. A 7nm Cr/Au current spreading layer was deposited on top of the AlN by thermal evaporation. Cr/Au was chosen due to limits in material available

and is not an ideal choice for forming a quasi-ohmic contact. This was followed by a Au probing contact, which was also thermally evaporated. To characterise the role of the interface between the insulating layer and the metal contact layers and to study any effects of oxidisation on the AlN surface, an additional sample was produced with the metal being sputtered immediately after the AlN, without breaking vacuum. Results for varying thickness are presented first, followed by the optimised sample.

7.1.1 The effect of varying AlN thickness

Photoluminescence

Photoluminescence (PL) measurements were performed at room temperature and used a pulsed Nd:YAG laser with a wavelength of 266nm.

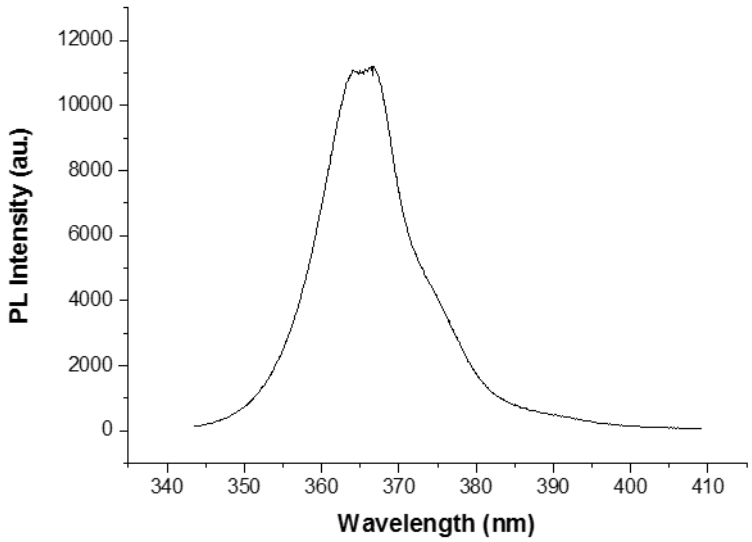

Figure 7-2: PL spectra of n-AlGaN layer

The PL spectra was used as a means of determining the epitaxial quality of the n-type layer before further work proceeded. Figure Figure 7-2 shows the emission peak at approximately 365nm, and it was concluded that the crystal quality was suitable to proceed.

Electrical Characterisation

After devices were fabricated, current-voltage (IV) measurements were performed. The results of these are shown in figure Figure 7-3. The sample with the 3nm AlN layer exhibits somewhat ohmic behaviour. This is indicative of carriers easily tunnelling through the insulating layer. This ohmic behaviour is readily suppressed with only a small increase in AlN thickness. The 5nm sample exhibits diode behaviour, albeit poor. This is observed as a significant reverse bias leakage current, indicating that electrons are still able to tunnel through the layer. When the barrier thickness is doubled, to 10nm, good diode behaviour is observed, with little reverse bias leakage. Increasing the thickness again, to 20nm, negatively impacts the device behaviour with resistance becoming high in forward bias thus preventing current from flowing. Of these four samples it is clear that a 10nm AlN layer provides the most suitable IV characteristics for realising light emission from such structures.

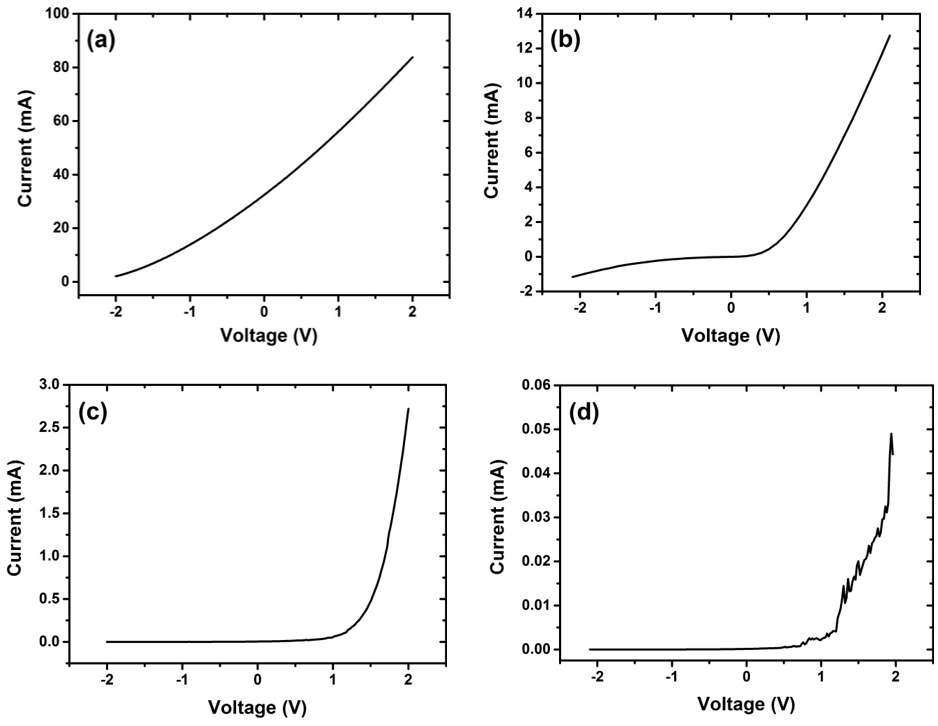

Figure 7-3: I-V characteristics of MIS structures with varying AlN layer thicknesses. (a) 3 nm, (b) 5 nm, (c) 10 nm and (d) 20 nm. [161]

Electrolumiescence characteristics

A Keithley 2602A was used to electrically drive the device under test, with all measurements being performed at room temperature. The output was measured with a spectrometer.

Figure Figure 7-4 shows how the electroluminescence (EL) spectra of the samples at 250mA drive current (a), and the EL spectra of the 10nm sample at different injection currents. Unsurprisingly (given its IV behaviour), no emission was observed from the 3nm sample. Only very weak emission was detected from the sample with the thickest AlN layer. Emission was observed from all the other samples, with the 5nm and 10nm devices giving the strongest emission. The emission was observed at 369nm and 367nm respectively. This slight offset occurs due to the voltage required to apply the 250mA injection current varying, and resulting in a difference in the relative band alignments near the active region.

Due to the absence of any p-type layer in this structure, it is most likely that carriers tunnel directly from the n-AlGaN valance band, through the AlN layer, to the Au/Cr contact and this provides the supply of holes required for radiative recombination. This is further reinforced by the reduced emission from the 20nm sample. Increasing injection current causes a broadening and red-shift of the peak, with similar behaviour being attributed to band bending at the interface [162].

The second graph in Figure 7-4 depicts the change in EL intensity of the 10nm AlN sample with varying injection current . Emission grows with increasing injection current before decreasing. Here the dominant mechanisms for this "efficiency droop" are not the same as those attributed to conventional GaN based LEDs (see 2.1.1, where the emission output which initially increases with injection current becomes sub-linear and only drops if there is Joule heating [163].

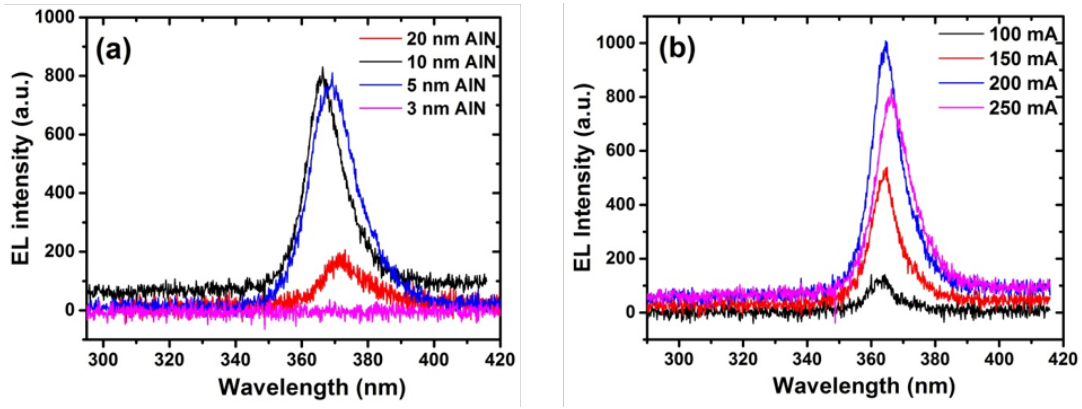

Figure 7-4: (a) EL spectra of devices with different AlN thicknesses under an injection current of 250 mA and (b) EL spectra of the MIS LED device with a 10 nm AlN insulating layer under different injection currents [161].

7.1.2 Optimised MIS device

A further MIS LED sample was fabricated, employing a 10nm AlN layer. In this instance to prevent contamination or oxidisation of the AlN surface, the metal contact was deposited immediately after AlN growth, without breaking vacuum.

Electrical characteristics

The I-V characteristic of this device can be seen in Figure 7-5, where the region of negative differential resistance (NDR) is clearly visible. These devices had also displayed some reverse bias leakage, although this was not significant (i.e. 100nA). This is a key characteristic of resonant tunnelling behaviour and was reproducible over repeated measurements as well as stable over time. This behaviour was observed in multiple devices processed on this wafer. This behaviour appears at larger voltages than those displayed in Figure 7-3, however those devices were measured at higher voltages and NDR was not observed.

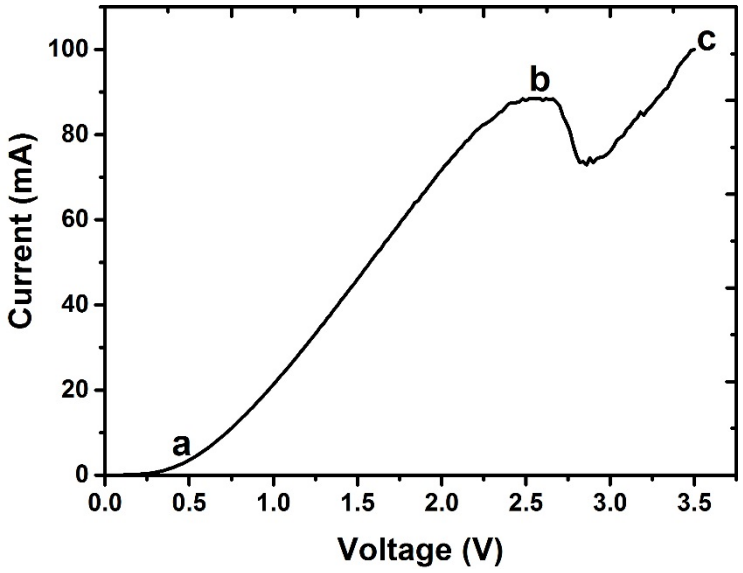

Figure 7-5: IV characteristics of MIS diode with 10 nm thick AlN layer.The labels a – c correspond to different regions of device behaviour [161]

Optical output characteristics

The variation in EL intensity with increasing injection current is shown in Figure 7-6. This device has a maximum peak intensity an order of magnitude greater than the sample structure with the metal contact deposited in a second step. Additionally the peak from this device is narrower and has a reduced red-shift than the previous device. This is indicative of the improved emission output and resonant tunnelling behaviour correlating with an enhanced metal/AlN interface.

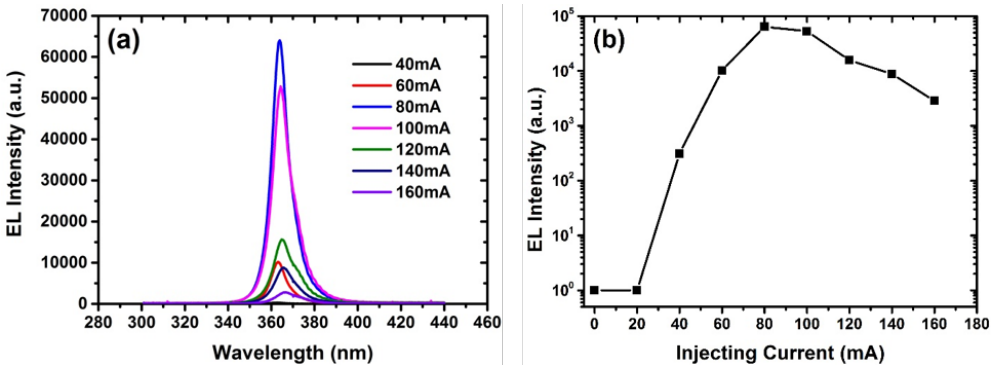

Figure 7-6: (a) EL spectra for the optimised device (b) Peak EL intensity against injection current for the same device [161].

The observed loss in efficiency cannot be attributed to Joule heating and so other mechanisms must be responsible. Such heating can be dismissed for several reasons. The device was processed and measured on wafer and the wafer was clamped to a heat sink whilst devices were tested, thus helping with local heat dissipation. A thermocouple was used in conjunction with the measurement set up and no temperature variation was observed. When compared with commercial LEDs emitting in the same region, the forward resistance was notably lower. The I-V characteristic of the devices remained consistent throughout the measurements, even after the LED was driven at high current. This is further evidence that Joule heating was not a dominant mechanism in the efficiency loss. Such stable performance can be partially attributed to the lack of a p-type layer, which is typically highly resistive and thus a significant contributor to heating and loss. The clean insulator/metal layer also helped to reduce contact resistance, improve current spreading and reduce any associated efficiency losses.

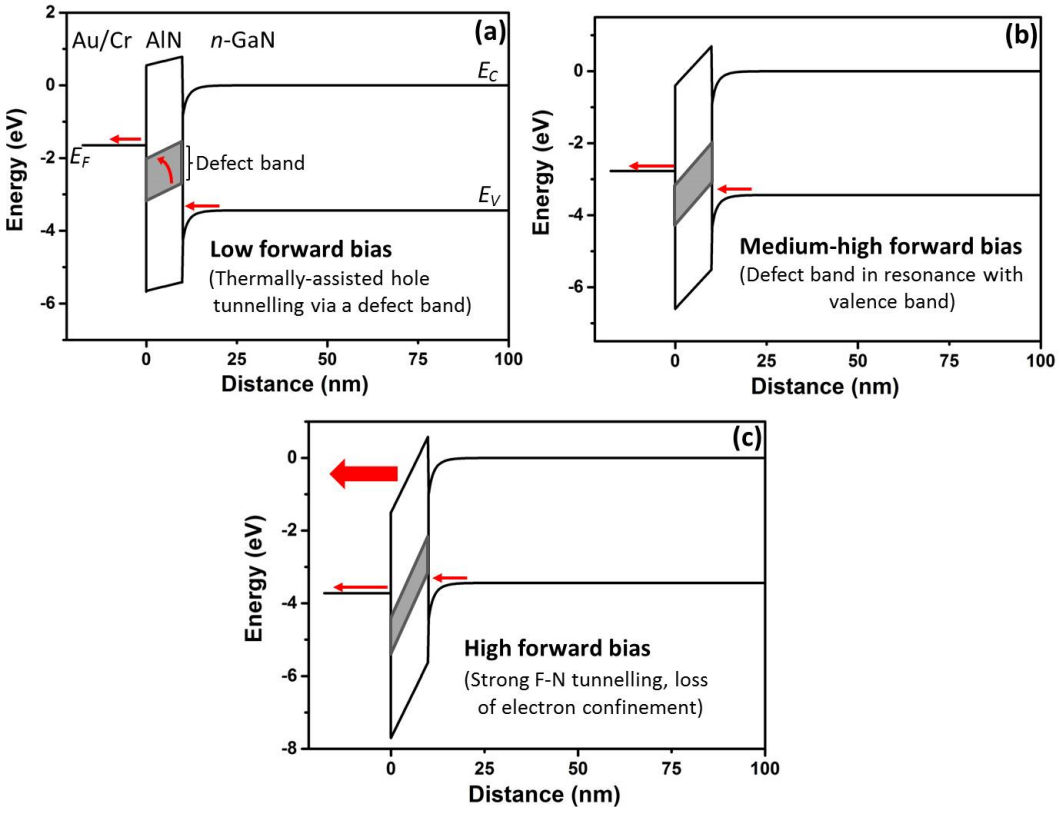

Figure 7-7: Energy band diagrams corresponding to the regions shown in Figure 7-5 [161]

The band diagrams shown in figure Figure 7-7 were obtained by modelling done by using the 1D-DDCC simulator and values obtained in the literature [164]. [1]

Most interestingly however, as the device starts to exhibit resonant tunnelling behaviour it also reaches its peak optical output, suggesting that tunnelling is responsible for supplying carriers [165]. A defect band in the sputtered AlN layer was anticipated and can be seen as the 400nm peak in the PL spectra shown in Figure 7-8. This measurement was taken from a reference sample. The band diagrams and mechanisms shown in Figure 7-7 are in alignments with the electrical and optical characteristics observed. At low forward bias the tunnelling probability is low but carriers are able to undergo thermally assisted tunnelling through a defect band. These correspond to point a in Figure 7-5 and inset a in 7-7. Point b in Figure 7-5 and diagram b in Figure 7-7 relate to an increase in applied voltage. Here there is an increase in band bending which leads to the AlN defect band and the metal's Fermi level aligning with valence band of the n-GaN meaning carriers can readily tunnel through the barrier. The defect and valence bands go out of resonance as the voltage is increased, resulting in few valence band holes being generated. Increasing the applied voltage further, as shown in point c Figure 7-5 and diagram c in Figure 7-7, results in carriers in the n-GaN conduction being able to easily tunnel; a process known as Fowler-Nordheim tunnelling. This is the process in which electrons can tunnel through a barrier in the presence of a strong electric field [166]. Electrons are no longer confined at the GaN/AlN interface and as such the rate of radiative recombination decreases. Defect states between the insulating layer and the contact metal also have a detrimental effect on light output and also increase the probability of Fowler-Nordheim tunnelling into the contact from the GaN conduction band. It is suggested that, due to the inability to thoroughly clean the n-GaN surface, defects present at the insulator/semiconductor interface may contribute to the resonant tunnelling mechanism.

[1] Simulations were performed by Chen-Sheng Lin at Imperial College, London.

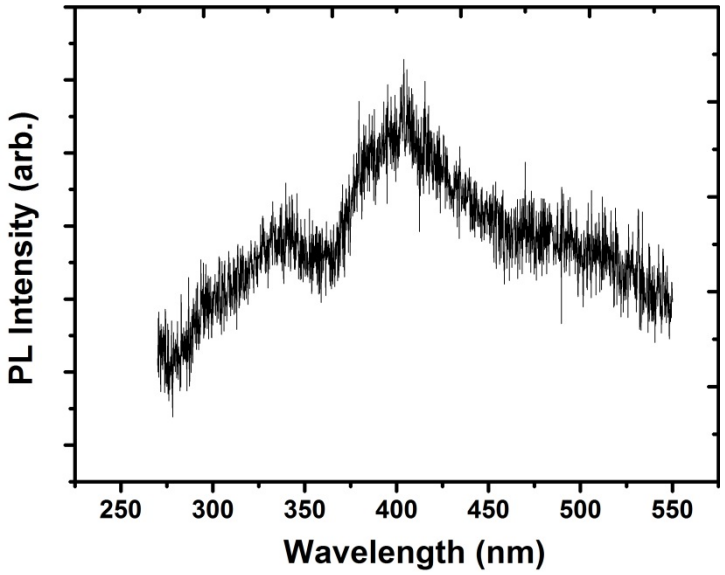

Figure 7-8: PL spectra from the defect band of sputtered AlN

7.1.3 Conclusion

Emission at 365nm was observed in simple MIS structures. It was found that a 10nm insulating layer gave optimal electrical and optical behaviour. The structure was further optimised when the insulating layer and metal contact were deposited in the same run in order to prevent surface contamination. Furthermore increased light emission correlates with the region of the IV characteristic that exhibits negative differential resistance and it is likely the free holes in the valence band arise from resonant tunnelling. The decrease in light emission at increased drive current is thought to be due to fewer conduction band electrons due to Fowler-Nordheim tunnelling. The resonant tunnelling occurs because of the presence of a defect band in the AlN layer. This work shows that such a structure can be used as a source of UV emission and is proof-of-principle. Further work can be focused in a number of directions including shortening emission wavelength and/or improving the efficiency of such structures by use of quantum well type structures for improved carrier confinement. Work on devices emitting at shorter wavelengths is presented below.

7.2 MIS structures emitting at 335nm

All work presented in this section is pending publication.

Further to the work presented on MIS devices emitting at 365nm, the remainder of this chapter will discuss work on devices emitting at 335nm.

The device consisted of an n-type AlGaN layer grown by MOCVD grown on top of a thick AlN buffer on a sapphire substrate. A thin, 10nm, AlN layer was deposited by sputter coating on top of the n-AlGaN layer. A 7nm layer of Ti/Au was deposited on top of the AlN layer and acted as a current spreader. A gold contact pad was deposited on top of this. A Ti/Al/Ni/Au contact was deposited on top of the n-type layer. A schematic and top view photo can be see in Figure 7-9.

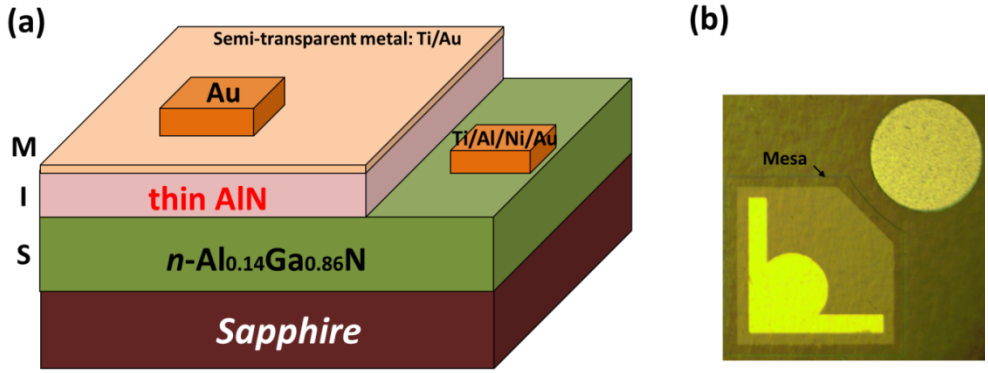

Figure 7-9: (a)Schematic the n-AlGaN based MIS LED structure discussed in this section. (b) The top view of one of these devices.

7.2.1 Characterisation of epitaxy

A 1 um thick n-AlGaN layer was grown by MOCVD on a thick AlN buffer layer on c-plane sapphire substrate. This layer was characterised by x-ray diffraction as is shown in 7-10 and is indicative that the growth is epitaxial, however in-plane orientation is required to confirm this.

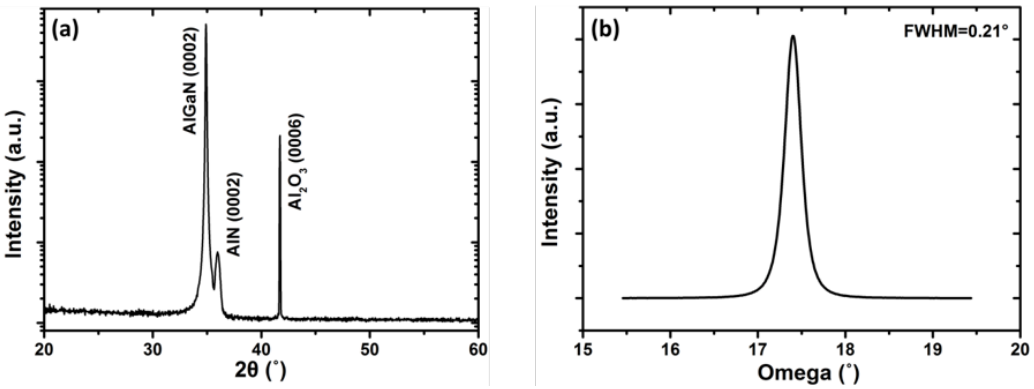

Figure 7-10: XRD diffractogram of an AlGaN layer grown on an AlN buffer layer with sapphire substrate. (a) Omega- 2θ scan. (b) Omega scan for the peak of AlGaN(0002).

The AlGaN bandgap and Al content were calculated from photoluminescence measurements using a pulsed Nd:YAG laser (266nm) at room temperature. The PL peak (see 7-11 was found to be at 334.7nm with a FWHM of 18.9nm, meaning the Al composition is around 14

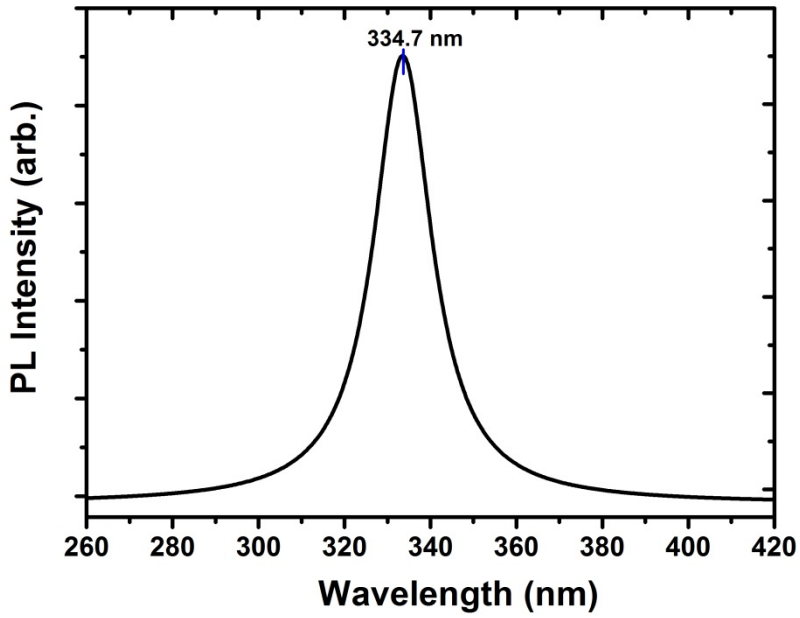

Figure 7-11: PL spectra of AlGaN layer.

7.2.2 Electrical characteristics

Again IV measurements were the primary means of testing the device characteristics and allow for the determination of carrier transport mechanisms. The results are plotted in 7-12 , with the linear nature of the IV characteristic of the annealed metal contact (Ti/Al/Ni/Au) and the n-AlGaN, shown in inset, confirming the ohmic nature of the contact. There is clear diode behaviour with a turn on voltage around 1.8V. The forward current at 5V was found to be around 40mA and at the same voltage in reverse bias $1.5x10^{-5}$ A, suggesting relatively low leakage.

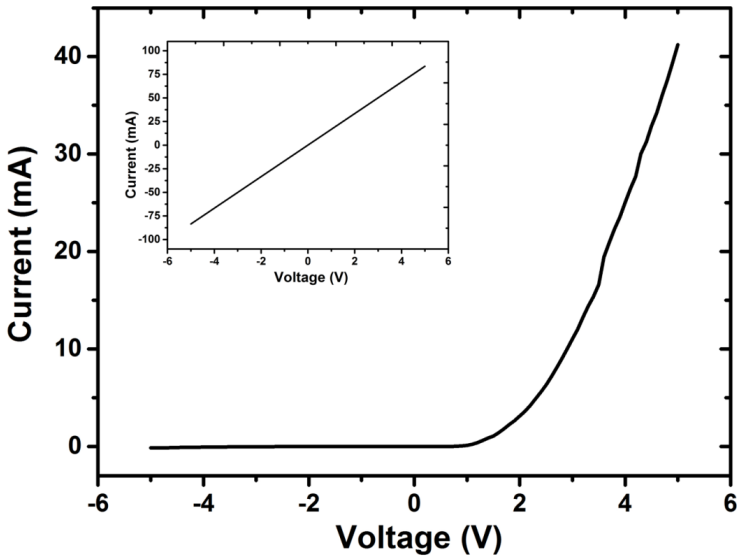

Figure 7-12: I-V characteristic of the MIS LED. Inset shows the IV characteristic of the ohmic contact between the Ti/Al/Ni/Au electrode and the n-AlGaN

Similar to the 365nm device, defect assisted tunnelling is observed in this device. IV characteristics can be replotted a number of ways in order to determine the mechanisms of carrier transport within the structure. Plotting the characteristic on a log-log scale shows there are three distinct regions, which can be seen in Figure 7-13. At low forward bias (region 1), the device behaves according to Ohm's Law i.e. the current is linearly related to voltage [167]. The exponential increase in current with voltage observed in region 2 is indicative of carriers tunnelling and recombining via defect states [168].

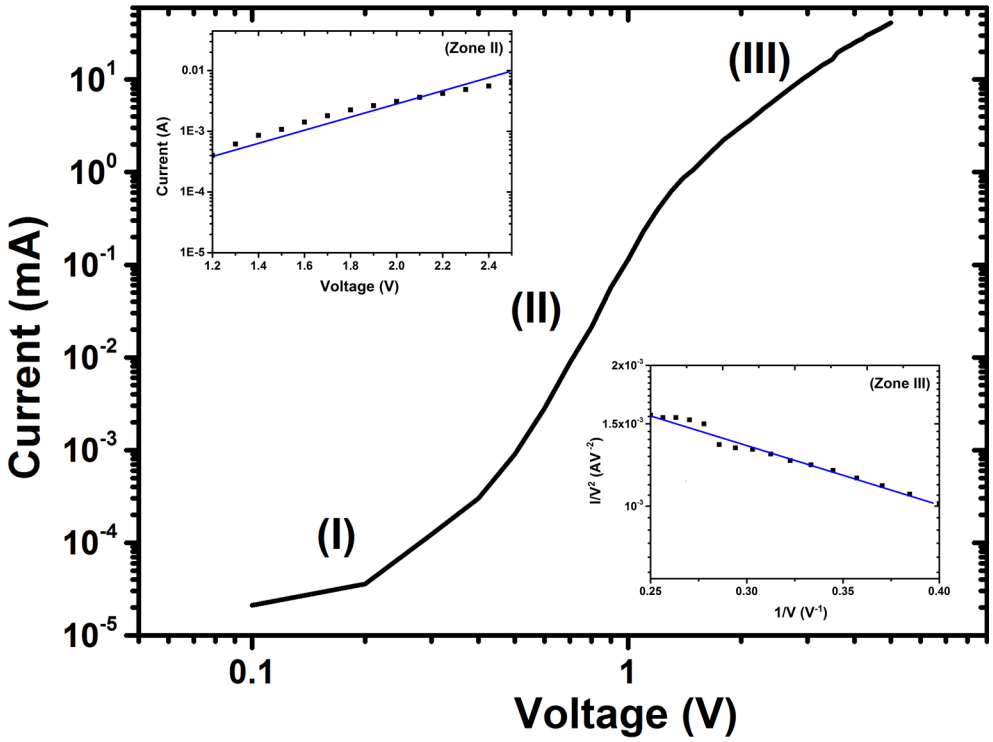

Figure 7-13: Log-log scale I-V characteristic with three zones labelled. Upper inset depicts the linear I-V plot on a semi-log scale in the zone II range. Lower inset presents I/V^2 against $1/V$ plotted on a semi-log scale

The upper inset of Figure 7-13 shows a semi-log plot of the second zone and shows a linear relationship. As the applied bias is increased the device moves into the third zone. The high electric field in this regions means the barrier is triangular in shape and there is only a thin barrier which means electrons can easily tunnel i.e. the dominant transport mechanism here is once again Fowler-Nordhiem [169]. This third zone is the standard one used in relation to this process. The IV characteristic was also plotted as I/V^2 vs $1/V$ on a semi-log scale and can be seen in the lower inset of Figure 7-13.

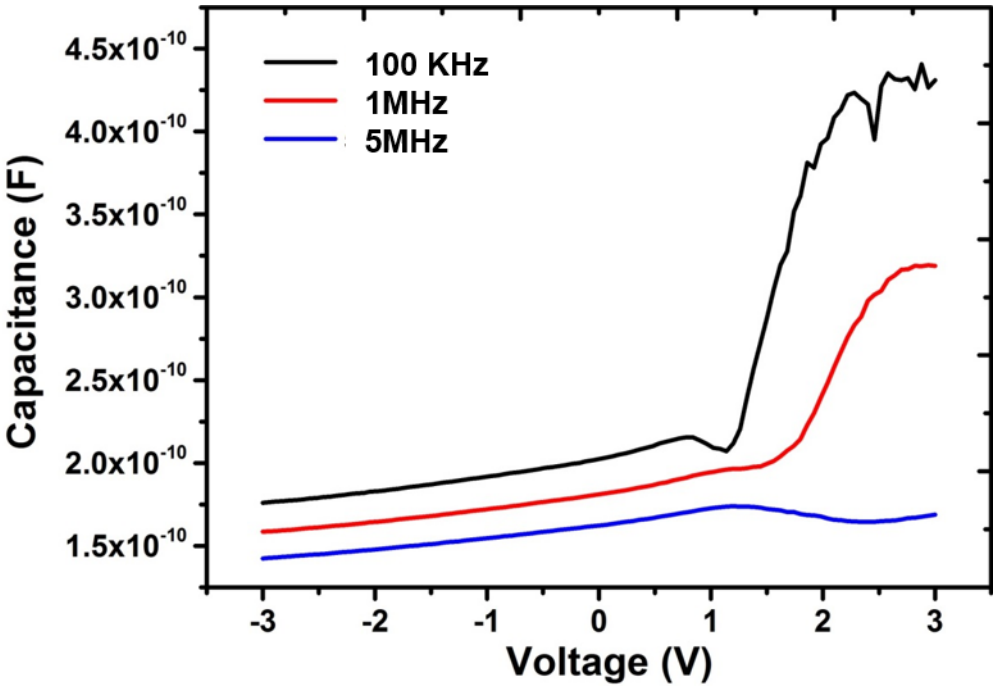

Figure 7-14: Frequency dependent capacitance-voltage characteristic of the device

Frequency dependent capacitance voltage (CV) measurements, shown in Figure 7-14, were taken to characterise any defects in the device. Interface defects are suggested by the dispersion between frequencies. The values of capacitance give different peaks at different frequencies and were not observed at high frequency, which suggests there are different types of interface defects with variable lifetimes [170]. A capacitance drop was found at 1MHz which is indicative of resonant tunnelling.

Both the IV and CV characteristics support the suggestion the carrier transport within the device is dominated by defect assisted tunnelling.

7.2.3 Electrolumiescence characteristics

As in the previous section, the device was driven using a Keithley 2602A and at room temperature. The electroluminescence spectra of the device can be seen in Figure 7-15. The peak emission intensity occurs at 335.4nm with a FWHM of roughly 18nm. This is strikingly close to the PL peak from the n-AlGaN layer which was 334.7nm, suggesting near band emission was achieved. The FWHM is narrower than p-n junction devices emitting at similar wavelengths, reported in

the literature by Yan et al [171]. The MIS structure has sharper emission peaks, as well as being easier to achieve and thus suggests it is a promising route to achieving deep UV emission.

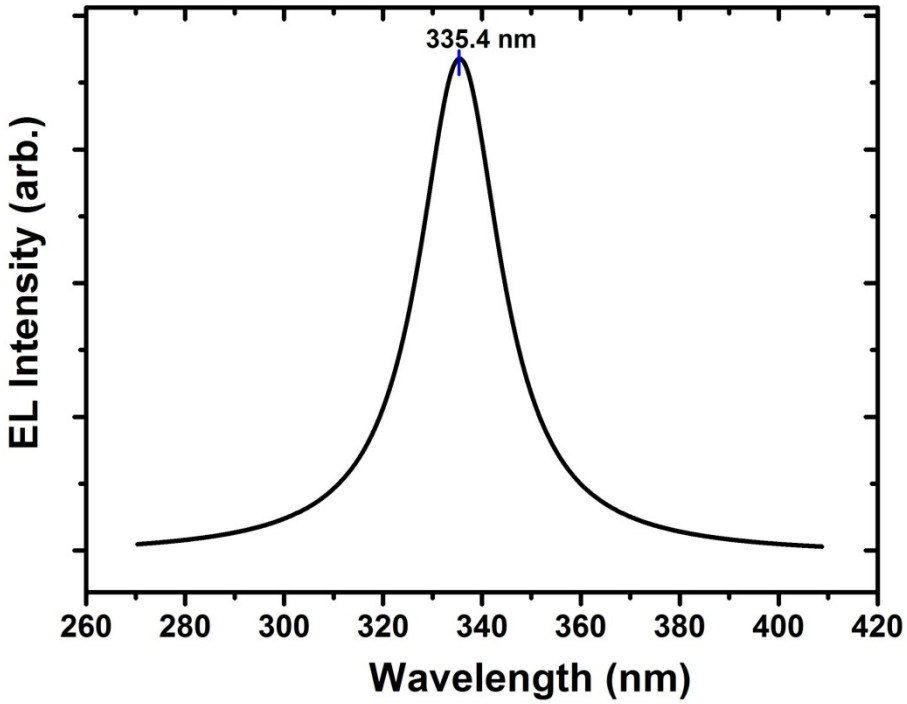

Figure 7-15: EL spectra of the LED.

7.2.4 Conclusion

An additional proof-of-concept structure was created to show the further potential for deep UV emission from simple p-layer free structures. Emission at 335nm was achieved using a Au/AlN/n-AlGaN device structure. As with the 365nm structure, a 10nm insulating layer was employed. X-ray diffraction and PL measurements were used to characterise the material before the device processing. Simple electrical characterisation indicates that defect-assisted tunnelling allows holes to be generated in the AlN layer and then recombine. This work proves that MIS type structures can be used to generate UV emission at different wavelengths.

7.3 Summary

This work demonstrates that alternatives to the tradition pn-junction foundations for LEDs are feasible for UV emission, an important result especially when considering the wider applications of low cost UV devices. It is hoped this work will lend itself to developing a straight forward approach to producing devices emitting in the UVC (100nm-280nm) region. Such developments may include the employment of quantum wells to improve carrier confinement within these MIS structures.

Chapter 8

Conclusion

This chapter aims to summarise the main findings of this work, as well as identify avenues for further work. Also included is a statement of impact which aims to put the work into context in broader terms.

8.1 Conclusions

A simple procedure was identified for detailed characterisation of loss mechanisms in long wavelength emitting devices. This was done through the use of extended analysis of the electrical behaviour (including temperature dependent measurements) and correlating this with the optical behaviour of the devices. A strong quantum confined stark effect was observed and correlated with the presences of Poole-Frenkle emission, reverse bias luminescence and significant leakage currents. All of these correlate with increased non-radiative recombination and all worsen as wavelength (and indium content) increase.

The use of interlayers as a means of improving the transparent conducting layer was then investigated. They are found to improve the opto-electrical properties of the devices. They act by means of increasing the hole concentration, which helps to circumnavigate the issues arising from the decreased hole concentration in p-type GaN. Inclusion of interlayers gives improved current spreading. Additionally interlayers significantly lower the contact resistance when compared to samples which do not have one. By annealing the interlayer before the thick oxide layer is deposited the overall efficiency is found to increase when compared to samples that were not annealed. Annealing in an ambient O_2 environment

improves the electrical characteristics. Following from that result further devices were fabricated using slightly thicker (3nm) Ni. This was annealed in O_2 before AZO was deposited. An additional sample was also prepared using a 5nm/5nm Ni/Au layer underneath the AZO. It was found that they had comparable contact resistances and that the 3nm Ni interlayer sample performed best overall. This shows that interlayer/AZO layers can compete with Ni/Au and ITO based contacts, without suffering from poor optical transmittance and thus could replace the traditional contacts.

Finally it was demonstrated that structures omitting a p-layer are a potential alternative to the traditional pn structure when creating UV emission sources.The optimal insulating layer thickness was found to be 10nm. The device behaviour was improved when metal contacts were deposited without vacuum being broken, suggesting surface contamination is detrimental to device performance. Electrical characterisation suggests that holes are generated via defect-assisted tunnelling. Additionally it was found that these devices can exhibit resonant tunnelling behaviour and this behaviour correlates with enhanced emission output.

8.2 Future Work

A number of areas have been identified as potential avenues for future work.

- Further work on the use of interlayers with AZO. Different metals, varying thickness, varying annealing conditions are needed to optimise the contact if AZO is to be realised as a true alternative to ITO.
- Additional alternative materials to ITO should be considered, with several prospects being suggested such as delafossites, such as $CuFeO_2$ [172].
- Characterisation of the specific causes of the poor quality AZO deposited on to the green epitaxy may prove vital if there are inherent incompatibilities between the materials.
- Further work is required on the optimisation of the MIS resonant tunnelling devices if they are to become commercially viable and useful. This must be done in all aspects of device creation including growth, the inclusion

of quantum well structures to improve carrier confinement, fabrication and contact development.

8.3 Impact statement

When conducting any research its wider impact should be considered. How the work presented in this thesis can be viewed in a broader landscape is discussed briefly here.

Comprehensive characterisation, especially of failure mechanisms, in complex structures in which specific mechanisms are hard to isolate is a vital step in realising improved efficiency. It is hoped that by identifying some of these, a greater understanding of device failure is gained. From this steps can be taken to avoid growth and processing techniques which encourage such mechanisms, and ultimately high efficiency green-gap devices can be realised. This will be most beneficial for white light systems and display applications, where greater efficiency means lower power consumption and thus not only lowers energy demand, but may allow for use in remote and developing communities.

Indium is now deemed a critical resource, but its consumption is increasing dramatically for use in electronics. As well as the environmental concerns regarding the mining of this material, it is also in short supply [173]. This is motivation to find more sustainable replacements. Here it has been shown that by including a very thin interlayer, AZO becomes a viable alternative to ITO. This could result in a reduced demand for a scarce resource and would allow it to only be used when necessary. AZO is also more cost effective, meaning it may push costs down, making the resulting technology available to all.

Perhaps the most interesting work in this thesis is discussed in the final chapter. Here is proved that MIS structures can be used as a source of UV emission, and that it is possible to reduce the wavelength. This is early stage work, but the concept is proved. The simple nature of these structures lends itself to low cost processing. The realisation of low cost deep UV devices has world changing consequences due to the germicidal nature of UVC (100nm - 280nm) radiation. Water-borne disease is the worlds biggest killer and antibiotic resistance is a growing problem, so low cost, efficient UVC devices could be employed as a means of sterilisation of water [174] and air, and ultimately could save millions of lives.

Bibliography

[1] H. J. Round, "A note on carborundum," *Electrical World 19*, vol. 19, pp. 309–310, 1907.

[2] O. Lossev, "Luminous carborundum detector and detection effect and oscillations with crystals," *The London, Edinburgh, and Dublin Philosophical Magazine and Journal of Science*, vol. 6, no. 39, pp. 1024–1044, 1928.

[3] M. G. Craford, R. W. Shaw, A. H. Herzog, and W. O. Groves, "Radiative recombination mechanisms in GaAsP diodes with and without nitrogen doping," *Journal of Applied Physics*, vol. 43, no. 10, pp. 4075–4083, 1972.

[4] H. Maruska, D. Stevenson, and J. Pankove, "Violet luminescence of Mg-doped GaN," *Applied Physics Letters*, vol. 22, pp. 303 – 305, 04 1973.

[5] S. Nakamura, M. Senoh, and T. Mukai, "Highly p-Typed Mg-Doped GaN Films Grown with GaN Buffer Layers," *Japanese Journal of Applied Physics*, vol. 30, pp. L1708–L1711, 1991.

[6] S. Nakamura, M. Senoh, and T. Mukai, "P-GaN/N-InGaN/N-GaN Double-Heterostructure Blue-Light-Emitting Diodes," *Japanese Journal of Applied Physics*, vol. 32, no. 1A, p. L8, 1993.

[7] S. Nakamura, M. Senoh, N. Iwasa, and S. Nagahama, "High Brightness InGaN Blue, Green and Yellow Light Emitting Diodes with Quantum Well Structures," *Japanese Journal of Applied Physics*, vol. 34, no. 7A, p. L797, 1995.

[8] I. Akasaki, H. Amano, K. Itoh, N. Koide, and K. Manabe, "GaN based UV/blue light-emitting devices," *GaAs and Related Compounds conference Institute of Physics Conference Series*, vol. 129, no. 851, 1992.

[9] H. Seong, T.Y., Han, J., Amano, H., Morkoc, *III-Nitride Based Light Emitting Diodes and Applications*. Springer Netherlands, 2013.

[10] E. F. Schubert, *Light Emitting Diodes*. Cambridge University Press, 2nd ed., 2006.

[11] W. Shockley and W. Read, "Statistics of the Recombinations of Holes and Electrons," *Phys. Rev.*, vol. 87, pp. 835–842, Sep 1952.

[12] R. Hall, "Electron-Hole Recombination in Germanium," *Phys. Rev.*, vol. 87, pp. 387–387, Jul 1952.

[13] W. Grieshaber, E. F. Schubert, I. D. Goepfert, R. F. Karlicek, M. J. Schurman, and C. Tran, "Competition between band gap and yellow luminescence in GaN and its relevance for optoelectronic devices," *Journal of Applied Physics*, vol. 80, p. 4615, 1996.

[14] Y. Rong, Y. Huo, E. T. Fei, M. Fiorentino, M. R. T. Tan, T. Ochalski, G. Huyet, L. Thylen, M. Chacinski, T. I. Kamins, and J. S. Harris, "High speed optical modulation in Ge quantum wells using quantum confined stark effect," *Frontiers of Optoelectronics*, vol. 5, no. 1, p. 82, 2012.

[15] S. Nakamura, M. Senoh, N. Iwasa, and S. ichi Nagahama, "Optimization of Electroluminescent Efficiencies for Vapor-Grown GaAsP diodes," *J.Electrochem Soc.: Solid State Sci*, vol. 116, no. 248, 1969.

[16] R. Zwierz, *Plasma enhanced growth of GaN single crystalline layers from vapour phase.* PhD thesis, Leibniz Institute for Crystal Growth, 07 2014.

[17] W. C. Johnson, J. B. Parson, and M. C. Crew, "Nitrogen Compounds of Gallium," *The Journal of Physical Chemistry*, vol. 36, no. 10, pp. 2651–2654, 1931.

[18] H. Maruska and J. Tietjen, "The Preparation and Properties of Vapor-Deposited Single-Crystal GaN," *Applied Physics Letters*, vol. 15, pp. 327–329, Nov 1969.

[19] J. Pankove, E. Miller, and J. Berkeyheiser, "GaN blue light-emitting diodes ," *Journal of Luminescence*, vol. 5, no. 1, pp. 84 – 86, 1972.

[20] J. Pankove, E. Miller, D. Richman, and J. Berkeyheiser, "Electroluminescence in GaN," *Journal of Luminescence*, vol. 4, no. 1, pp. 63 – 66, 1971.

[21] H. Maruska, W. Rhines, and D. Stevenson, "Preparation of Mg-doped GaN diodes exhibiting violet electroluminescence," *Materials Research Bulletin*, vol. 7, no. 8, pp. 777 – 781, 1972.

[22] S. Yoshida, S. Misawa, and S. Gonda, "Improvements on the electrical and luminescent properties of reactive molecular beam epitaxially grown GaN films by using AlN-coated sapphire substrates," *Applied Physics Letters*, vol. 42, pp. 427–429, 1983.

[23] S. Nakamura, "GaN Growth Using GaN Buffer Layer," *Japanese Journal of Applied Physics*, vol. 30, no. 10A, p. L1705, 1991.

[24] S. Nakamura, N. Iwasa, M. Senoh, and T. Mukai, "Hole Compensation Mechanism of p-Type GaN Films," *Japanese Journal of Applied Physics*, vol. 31, no. 5R, p. 1258, 1992.

[25] H. Amano, M. Kito, K. Hiramatsu, and I. Akasaki, "P-Type Conduction in Mg-Doped GaN Treated with Low-Energy Electron Beam Irradiation (LEEBI)," *Japanese Journal of Applied Physics*, vol. 28, no. 12A, p. L2112, 1989.

[26] L. Liu and J. Edgar, "Substrates for Gallium Nitride epitaxy," *Materials Science and Engineering: R: Reports*, vol. 37, no. 3, pp. 61–127, 2002.

[27] F. Brunner, A. Knauer, T. Schenk, M. Weyers, and J. Zettler, "Quantitative analysis of in situ wafer bowing measurements for III-nitride growth on sapphire ," *Journal of Crystal Growth*, vol. 310, no. 10, pp. 2432 – 2438, 2008.

[28] M. E. Levinshtein, S. L. Rumyantsev, and M. S. Shur, *Properties of Advanced Semiconductor Materials: GaN, AlN, InN, BN, SiC, SiGe.* Wiley, 2nd ed., 2001.

[29] T. Zhu and R. A. Oliver, "Unintentional doping in GaN," *Phys. Chem. Chem. Phys.*, vol. 14, pp. 9558–9573, 2012.

[30] H. M. Manasevit, "Single-crystal Gallium Arsenide on Insulating Substrates," *Applied Physics Letters*, vol. 12, no. 4, pp. 156–159, 1968.

[31] J. J. Coleman, "Metalorganic chemical vapor deposition for optoelectronic devices," *Proceedings of the IEEE*, vol. 85, no. 11, pp. 1715–1729, 1997.

[32] M. H. Crawford, "LEDs for Solid-State Lighting : Performance Challenges and Recent Advances," *IEEE Journal of Selected Topics in Quantum Electronics*, vol. 15, no. 4, pp. 1028–1040, 2009.

[33] R. S. Berns, "Designing white-light LED lighting for the display of art: A feasibility study," *Color Research & Application*, vol. 36, no. 5, pp. 324–334, 2011.

[34] S. Nakamura, M. Senoh, N. Iwasa, and S. Nagahama, "High-Brightness InGaN Blue, Green and Yellow Light-Emitting Diodes with Quantum Well Structures," *Japanese Journal of Applied Physics*, vol. 34, no. 7A, p. L797, 1995.

[35] F. Ponce and D. Bour, "Nitride-based semiconductors for green and blue light emitting devices," *Nature*, vol. 386, pp. 351–359, 1997.

[36] E. K. Kim and J. S. Kim, "Electrical Study on Indium-Rich InGaN/GaN Multi-Quantum-Well System," *Journal of the Korean Physical Society*, vol. 49, no. 5, pp. 2132–2135, 2006.

[37] K. Cavanagh, "Innovative InGaN based long wavelength light emitting diode structures," March 2015.

[38] C. K. Z. Liliental-Weber and S. Nakamura, "Atomic scale indium distribution in a $GaN/In_{0.43}GaN/Al_{0.1}Ga_{0.9}N$ quantum well structure," *Jpn. J. Appl. Phys*, vol. 36, pp. 6932–6936, 1997.

[39] K. H. Baloch, A. C. Johnston-Peck, K. Kisslinger, E. a. Stach, and S. Gradecak, "Revisiting the "In-clustering" question in InGaN through the use of aberration-corrected electron microscopy below the knock-on threshold," *Applied Physics Letters*, vol. 102, no. 19, p. 191910, 2013.

[40] S. E. Bennett, D. W. Saxey, M. J. Kappers, J. S. Barnard, C. J. Humphreys, G. D. Smith, and R. A. Oliver, "Atom probe tomography assessment of the impact of electron beam exposure on $In_xGa_{1-x}N/GaN$ quantum wells," *Applied Physics Letters*, vol. 99, no. 2, 2011.

[41] Y. C. Shen, G. O. Mueller, S. Watanabe, N. F. Gardner, A. Munkholm, and M. R. Krames, "Auger recombination in InGaN measured by photoluminescence," *Applied Physics Letters*, vol. 91, no. 14, p. p. 141101, 2007.

[42] M.-H. Kim, M. F. Schubert, Q. Dai, J. K. Kim, E. F. Schubert, J. Piprek, and Y. Park, "Origin of efficiency droop in GaN-based light-emitting diodes," *Applied Physics Letters*, vol. 91, no. 18, p. 183507, 2007.

[43] Y. Li, Y. Huang, and Y. Lai, "Efficiency droop behaviors of InGaN/GaN multiple quantum well light emitting diodes with varying quantum well thickness," *Applied Physics Letters*, vol. 91, no. 18, p. 181113, 2007.

[44] B. Monemar and B. E. Sernelius, "Defect related issues in the "current roll-off" in InGaN based light emitting diodes," *Applied Physics Letters*, vol. 91, no. 18, p. 181103, 2007.

[45] E. Kioupakis, P. Rinke, K. T. Delaney, and C. G. Van de Walle, "Indirect Auger recombination as a cause of efficiency droop in nitride light-emitting diodes," *Appl. Phys. Lett.*, vol. 98, p. 161107, 2011.

[46] J. Iveland, L. Martinelli, J. Peretti, J. Speck, and C. Weisbuch, "Direct Measurement of Auger Electrons Emitted from a Semiconductor Light-Emitting Diode under Electrical Injection: Identification of the Dominant Mechanism for Efficiency Droop," *Phys. Rev. Lett.*, vol. 110, p. 177406, Apr 2013.

[47] Q. Dai, Q. Shan, J. Wang, S. Chhajed, J. Cho, E. F. Schubert, M. H. Crawford, D. D. Koleske, M.-H. Kim, and Y. Park, "Carrier recombination mechanisms and efficiency droop in GaInN/GaN light-emitting diodes," *Applied Physics Letters*, vol. 97, no. 13, p. 133507, 2010.

[48] S. Kim, K. Lee, K. Park, and C.-S. Kim, "Effects of barrier growth temperature on the properties of InGaN/GaN multi-quantum wells," *Journal of Crystal Growth*, vol. 247, no. 1, pp. 62 – 68, 2003.

[49] P. Ruterana, S. Kret, A. Vivet, G. Maciejewski, and P. Dłużewski, "Composition fluctuation in InGaN quantum wells made from molecular beam or metalorganic vapor phase epitaxial layers," *Journal of Applied Physics*, vol. 91, pp. 8979–8985, 06 2002.

[50] Y. Wu, "Investigation of strain effect in InGaN/GaN multi-quantum wells," *Indian Journal of Pure & Applied Physics*, vol. 51, no. 1, pp. 39–43, 2013.

[51] J. Piprek, R. Farrell, S. Denbaars, and S. Nakamura, "Effects of Built-In Polarization on InGaN – GaN," *IEEE Photonics Technology Letters*, vol. 18, no. 1, pp. 2005–2007, 2006.

[52] U. T. Schwarz, H. Braun, K. Kojima, Y. Kawakami, S. Nagahama, and T. Mukai, "Interplay of built-in potential and piezoelectric field on carrier recombination in green light emitting InGaN quantum wells," *Applied Physics Letters*, vol. 91, no. 12, p. 123503, 2007.

[53] C. Bayram, J. Pau, R. McClintock, and M. Razeghi, "Comprehensive study of blue and green multi-quantum-well light-emitting diodes grown on conventional and lateral epitaxial overgrowth GaN," *Appl Phys B*, vol. 95, pp. 307–314, 2009.

[54] L. Y. Lee, "Cubic zincblende gallium nitride for green-wavelength light-emitting diodes," *Materials Science and Technology*, vol. 33, no. 14, pp. 1570–1583, 2017.

[55] T. Paskova, D. A. Hanser, and K. R. Evans, "GaN Substrates for III-Nitride Devices," *Proceedings of the IEEE*, vol. 98, no. 7, pp. 1324–1338, 2010.

[56] A. Avramescu, T. Lermer, J. Muller, S. Tautz, D. Queren, S. Lutgen, and U. Strauss, "InGaN laser diodes with 50 mW output power emitting at 515 nm," *Applied Physics Letters*, vol. 95, no. 7, p. 071103, 2009.

[57] Y.-Y. Wong, E. Y. Chang, T.-H. Yang, J.-R. Chang, J.-T. Ku, M. K. Hudait, W.-C. Chou, M. Chen, and K.-L. Lin, "The Roles of Threading Dislocations on Electrical Properties of AlGaN/GaN Heterostructure Grown by MBE," *Journal of The Electrochemical Society*, vol. 157, no. 7, pp. H746–H749, 2010.

[58] T. J. Rupert, D. S. Gianola, Y. Gan, and K. J. Hemker, "Experimental Observations of Stress-Driven Grain Boundary Migration," *Science*, vol. 326, no. 5960, pp. 1686–1690, 2009.

[59] F. K. Yam, L. L. Low, S. A. Oh, , and Z. Hassan, *Gallium Nitride: An Overview of Structural Defects*. Rijeka: IntechOpen, 2011.

[60] S. Lazar, J. L. Weyher, L. Macht, F. D. Tichelaar, and H. W. Zandbergen, "Nanopipes in GaN: photo-etching and TEM study," *The European Physical Journal Applied Physics*, vol. 27, no. 1-3, p. 275–278, 2004.

[61] G. Li, S. J. Chua, S. J. Xu, W. Wang, P. Li, B. Beaumont, and P. Gibart, "Nature and elimination of yellow-band luminescence and donor–acceptor emission of undoped GaN," *Applied Physics Letters*, vol. 74, no. 19, pp. 2821–2823, 1999.

[62] M. Ferdous, *Effect of defects on the electrical/optical performance of gallium nitride based junction devices*. PhD thesis, The University of New Mexico, 2008.

[63] X. Cao, E. Stokes, P. Sandvik, S. LeBoeuf, J. Kretchmer, and D. Walker, "Diffusion and tunneling currents in GaN/InGaN multiple quantum well light-emitting diodes," *IEEE Electron Device Letters*, no. 9, pp. 535–537, 2002.

[64] X. A. Cao, J. M. Teetsov, M. P. D'Evelyn, D. W. Merfeld, and C. H. Van, "Electrical characteristics of InGaN/GaN light-emitting diodes grown on GaN and sapphire substrates," *Applied Physics Letters*, vol. 85, pp. 7–9, 2004.

[65] M. a. Reshchikov and H. Morkoc, "Luminescence properties of defects in GaN," *Journal of Applied Physics*, vol. 97, no. 6, p. 061301, 2005.

[66] R. Arif, H. Zhao, Y.-K. Ee, and N. Tansu, "Spontaneous Emission and Characteristics of Staggered InGaN Quantum-Well Light-Emitting Diodes," *Quantum Electronics, IEEE Journal of*, vol. 44, pp. 573–580, June 2008.

[67] R. A. Arif, Y.-K. Ee, and N. Tansu, "Polarization engineering via staggered InGaN quantum wells for radiative efficiency enhancement of light emitting diodes," *Applied Physics Letters*, vol. 91, no. 9, p. 091110, 2007.

[68] H. Zhao, G. Liu, X.-H. Li, G. S. Huang, J. D. Poplawsky, S. T. Penn, V. Dierolf, and N. Tansu, "Growths of staggered InGaN quantum wells light-emitting diodes emitting at 520–525 nm employing graded growth-temperature profile," *Applied Physics Letters*, vol. 95, no. 6, p. 061104, 2009.

[69] S.-H. Park, D. Ahn, B.-H. Koo, and J.-W. Kim, "Electronic and optical properties of staggered InGaN/InGaN quantum-well light-emitting diodes," *Physica status solidi (a)*, vol. 206, no. 11, pp. 2637–2640, 2009.

[70] S.-H. Park, D. Ahn, and J.-W. Kim, "High-efficiency staggered 530 nm InGaN/InGaN/GaN quantum-well light-emitting diodes," *Applied Physics Letters*, vol. 94, no. 4, pp. –, 2009.

[71] S.-H. Park, D. Ahn, J. Park, and Y.-T. Lee, "Optical Properties of Staggered InGaN/InGaN/GaN Quantum-Well Structures with Ga- and N-Faces," *Japanese Journal of Applied Physics*, vol. 50, no. 7R, p. 072101, 2011.

[72] R. A. Arif, H. Zhao, and N. Tansu, "Type-II InGaN-GaNAs quantum wells for lasers applications," *Applied Physics Letters*, vol. 92, no. 1, pp. 011104–01114–3, 2008.

[73] H. Zhao, G. Liu, J. Zhang, J. D. Poplawsky, V. Dierolf, and N. Tansu, "Approaches for high internal quantum efficiency green InGaN light-emitting diodes with large overlap quantum wells," *Opt. Express*, vol. 19, pp. A991–A1007, Jul 2011.

[74] Z.-H. Zhang, W. Liu, Z. Ju, S. T. Tan, Y. Ji, Z. Kyaw, X. Zhang, L. Wang, X. W. Sun, and H. V. Demir, "InGaN/GaN multiple-quantum-well light-emitting diodes with a grading InN composition suppressing the Auger recombination," *Applied Physics Letters*, vol. 105, no. 3, p. 033506, 2014.

[75] C. H. Wang, S. P. Chang, W. T. Chang, J. C. Li, Y. S. Lu, Z. Y. Li, H. C. Yang, H. C. Kuo, T. C. Lu, and S. C. Wang, "Efficiency droop alleviation in InGaN/GaN light-emitting diodes by graded-thickness multiple quantum wells," *Applied Physics Letters*, vol. 97, no. 18, pp. –, 2010.

[76] T. Onuma, Y. Uchinuma, E.-K. Suh, H.-J. Lee, T. Sota, and S. F. Chichibu, "Improved Emission Efficiency in InGaN / GaN Quantum Wells with Compositionally-Graded Barriers Studied by Time-Resolved Photoluminescence Spectroscopy," *Japanese Journal of Applied Physics*, vol. 42, no. 11B, p. L1369, 2003.

[77] W. Lei, L. Sowing, Z. Yang, L. Ding, T. Yu, N. Liu, L. Liu, C. Weihua, and H. Xiaodong, "Emission rate asymmetrically graded 480 nm InGaN / Gan quantum well light-emitting diodes," *Applied Physics Letters*, vol. 95, no. 21, p. 211104, 2009.

[78] Y.-A. Chang, Y.-T. Kuo, J.-Y. Chang, and Y.-K. Kuo, "Investigation of InGaN green light-emitting diodes with chirped multiple quantum well structures," *Opt. Lett.*, vol. 37, pp. 2205–2207, Jun 2012.

[79] J.-Y. Zhang, J.-Y. Zhang, L.-E. Cai, L.-E. Cai, B.-P. Zhang, B.-P. Zhang, X.-L. Hu, X.-L. Hu, F. Jiang, F. Jiang, J.-Z. Yu, J.-Z. Yu, Q.-M. Wang, and Q.-M. Wang, "Efficient hole transport in asymmetric coupled InGaN multiple quantum wells," *Appl. Phys. Lett.*, vol. 95, no. 16, pp. 161110–161110–3, 2009.

[80] H. Zhao, G. Liu, and N. Tansu, "Analysis of InGaN-delta-InN quantum wells for light-emitting diodes," *Applied Physics Letters*, vol. 97, no. 13, p. 131114, 2010.

[81] J. Park and Y. Kawakami, "Photoluminescence property of InGaN single quantum well with embedded AlGaN delta layer," *Applied Physics Letters*, vol. 88, no. 20, p. 202107, 2006.

[82] J. Zhang and N. Tansu, "Improvement in spontaneous emission rates for InGaN quantum wells on ternary InGaN substrate for light-emitting diodes," *Journal of Applied Physics*, vol. 110, no. 11, pp. 113110–113110, 2011.

[83] M. Krames, O. Shchekin, R. Mueller-Mach, G. O. Mueller, L. Zhou, G. Harbers, and M. Craford, "Status and Future of High-Power Light-Emitting Diodes for Solid-State Lighting," *Display Technology, Journal of*, vol. 3, pp. 160–175, June 2007.

[84] H. Li, P. Li, J. Kang, Z. Li, Y. Zhang, Z. Li, J. Li, X. Yi, J. Li, and G. Wang, "Quantum Efficiency Enhancement of 530nm InGaN Green Light-Emitting Diodes with Shallow Quantum Well," *Applied Physics Express*, vol. 6, p. 052102, 2013.

[85] I.-K. Park, M.-K. Kwon, and S.-J. Park, "A comparison of the recombination efficiency in green-emitting InGaN quantum dots and quantum wells," *Journal of the Korean Physical Society*, vol. 60, no. 10, pp. 1666–1670, 2012.

[86] I.-K. Park, M.-K. Kwon, J.-O. Kim, S.-B. Seo, J.-Y. Kim, J.-H. Lim, S.-J. Park, and Y.-S. Kim, "Green light-emitting diodes with self-assembled In-rich InGaN quantum dots," *Applied Physics Letters*, vol. 91, no. 13, p. 133105, 2007.

[87] S.-H. Han, D.-Y. Lee, S.-J. Lee, C.-Y. Cho, M.-K. Kwon, S. P. Lee, D. Y. Noh, D.-J. Kim, Y. C. Kim, and S.-J. Park, "Effect of electron blocking layer on efficiency droop in InGaN/GaN multiple quantum well light-emitting diodes," *Applied Physics Letters*, vol. 94, no. 23, pp. –, 2009.

[88] C. S. Xia, Z. M. Simon Li, and Y. Sheng, "On the importance of AlGaN electron blocking layer design for GaN-based light-emitting diodes," *Applied Physics Letters*, vol. 103, no. 23, pp. –, 2013.

[89] H. Zhao, G. Liu, R. A. Arif, and N. Tansu, "Current injection efficiency induced efficiency-droop in InGaN quantum well light-emitting diodes," *Solid-State Electronics*, vol. 54, no. 10, pp. 1119 – 1124, 2010. Selected Papers from ISDRS 2009.

[90] S. Choi, H. J. Kim, S.-S. Kim, J. Liu, J. Kim, J.-H. Ryou, R. D. Dupuis, A. M. Fischer, and F. A. Ponce, "Improvement of peak quantum efficiency and efficiency droop in III-nitride visible light-emitting diodes with an InAlN electron-blocking layer," *Applied Physics Letters*, vol. 96, no. 22, 2010.

[91] H. J. Kim, S. Choi, S.-S. Kim, J.-H. Ryou, P. D. Yoder, R. D. Dupuis, A. M. Fischer, K. Sun, and F. A. Ponce, "Improvement of quantum efficiency by employing active-layer-friendly lattice-matched InAlN electron blocking layer in green light-emitting diodes," *Applied Physics Letters*, vol. 96, no. 10, 2010.

[92] M. Reed, E. Readinger, H. Shen, M. Wraback, A. Syrkin, A. Usikov, O. Kovalenkov, and V. Dmitriev, "n-InGaN/p-GaN single heterostructure light emitting diode with p-side down," *Applied Physics Letters*, vol. 93, pp. 133505–133505–3, Sep 2008.

[93] M. L. Reed, E. D. Readinger, C. G. Moe, H. Shen, M. Wraback, A. Syrkin, A. Usikov, O. V. Kovalenkov, and V. A. Dmitriev, "Benefits of negative polarization charge in n -InGaN on p -GaN single heterostructure light emitting diode with p -side down," *physica status solidi (c)*, vol. 6, no. 2, pp. 585–588, 2009.

[94] K. S. A. Butcher, B. W. Kemp, I. B. Hristov, P. Terziyska, P. W. Binsted, and D. Alexandrov, "Gallium Nitride Film Growth Using a Plasma Based Migration Enhanced Afterglow Chemical Vapor Deposition System," *Japanese Journal of Applied Physics*, vol. 51, no. 1S, p. 01AF02, 2012.

[95] X. H. Wang, P. T. Lai, and H. W. Choi, "The contribution of sidewall light extraction to efficiencies of polygonal light-emitting diodes shaped with laser micromachining," *Journal of Applied Physics*, vol. 108, no. 2, 2010.

[96] S. E. Brinkley, C. L. Keraly, J. Sonoda, C. Weisbuch, J. S. Speck, S. Nakamura, and S. P. DenBaars, "Chip Shaping for Light Extraction Enhancement of Bulk c -Plane Light-Emitting Diodes," *Applied Physics Express*, vol. 5, no. 3, p. 032104, 2012.

[97] B. Sun, L. Zhao, T. Wei, X. Yi, Z. Liu, G. Wang, and J. Li, "Shape designing for light extraction enhancement bulk-GaN light-emitting diodes," *Journal of Applied Physics*, vol. 113, no. 24, pp. –, 2013.

[98] Y. D. Zhuang, S. Lis, J. Bruckbauer, S. E. J. O'Kane, P. A. Shields, P. R. Edwards, J. Sarma, R. W. Martin, and D. W. E. Allsopp, "Optical Properties of GaN Nanorods Containing a Single or Multiple InGaN Quantum Wells," *Japanese Journal of Applied Physics*, vol. 52, no. 8S, p. 08JE11, 2013.

[99] M. Clampham, P.B. Hutley, "Reduction of Lens Reflexion by the Moth Eye Principle," *Nature*, vol. 244, p. 281, 1973.

[100] S. Li and A. Waag, "GaN based nanorods for solid state lighting," *Journal of Applied Physics*, vol. 111, no. 7, pp. –, 2012.

[101] T. Fujii, Y. Gao, R. Sharma, E. Hu, S. DenBaars, and S. Nakamura, "Increase in the extraction efficiency of GaN-based light-emitting diodes via surface roughening," *Applied Physics Letters*, vol. 84, pp. 855–857, Feb 2004.

[102] H.-W. Huang, J. T. Chu, C. C. Kao, T. H. Hseuh, T. C. Lu, H. C. Kuo, S. C. Wang, and C. C. Yu, "Enhanced light output of an InGaN/GaN light emitting diode with a nano-roughened p-GaN surface," *Nanotechnology*, vol. 16, no. 9, p. 1844, 2005.

[103] D.-S. Leem, T. Lee, and T.-Y. Seong, "Enhancement of the light output of GaN-based light-emitting diodes with surface-patterned ITO electrodes by maskless wet-etching," *Solid-State Electronics*, vol. 51, no. 5, pp. 793 – 796, 2007.

[104] M. Ma, A. N. Noemaun, J. Cho, E. F. Schubert, G. B. Kim, and C. Sone, "Emission pattern control and polarized light emission through patterned graded-refractive-index coatings on GaInN light-emitting diodes," *Opt. Express*, vol. 20, pp. 16677–16683, Jul 2012.

[105] N. Abu-Ageel and D. Aslam, "Laser-Driven Visible Solid-State Light Source for Etendue-Limited Applications," *Display Technology, Journal of*, vol. 10, pp. 700–703, Aug 2014.

[106] M. Ma, J. Cho, E. F. Schubert, G. B. Kim, and C. Sone, "Optically functional surface structures for GaN-based light-emitting diodes," *Journal of Materials Chemistry C*, vol. 1, no. 48, p. 8134, 2013.

[107] D. Feezell, J. Speck, S. Denbaars, and S. Nakamura, "Optoelectronic Devices Grown on Nonpolar and Semipolar Free-Standing GaN Substrates," *2011 International Conference on Compound Semiconductor Manufacturing Technologys 2011*, pp. 2–5, 2011.

[108] X. Wang, G. Yu, B. Lei, X. Wang, C. Lin, Y. Sui, S. Meng, M. Qi, and A. Li, "Recovery of Dry Etching Induced Damage in n-GaN by Nitrogen Plasma Treatment at Growth Temperature," *Journal of Electronic Materials*, vol. 36, no. 6, pp. 697–701, 2007.

[109] J.-M. Lee, K.-S. Lee, and S.-J. Park, "Removal of dry etch damage in p-type GaN by wet etching of sacrificial oxide layer," *Journal of Vacuum Science & Technology B: Microelectronics and Nanometer Structures*, vol. 22, no. 2, p. 479, 2004.

[110] A. Zangwill, *Physics at Surfaces*. Cambridge University Press, 1988.

[111] S. Sze, *Physics of Semiconductor Devices*. Wiley, 3rd ed., 2006.

[112] A. Rockett, *The Materials Science of Semiconductors*. Springer US, 1st ed., 2008.

[113] C.-m. Kang, H. Shin, and C. Lee, "High-frequency organic rectifiers through interface engineering," *MRS Communications*, pp. 1–15, 09 2017.

[114] Q. Liu and S. Lau, "A review of the metal–GaN contact technology," *Solid-State Electronics*, vol. 42, no. 5, pp. 677 – 691, 1998.

[115] J. K. Sheu, Y. K. Su, G. C. Chi, P. L. Koh, M. J. Jou, C. M. Chang, C. C. Liu, and W. C. Hung, "High-transparency Ni/Au ohmic contact to p-type GaN," *Applied Physics Letters*, vol. 74, no. 16, pp. 2340–2342, 1999.

[116] C.-Y. Chang, Y. Fang, and S. Sze, "Specific contact resistance of metal-semiconductor barriers," *Solid-State Electronics*, vol. 14, p. 541–550, 07 1971.

[117] S. N. Mohammad, "Contact mechanisms and design principles for alloyed ohmic contacts to n-GaN," *Journal of Applied Physics*, vol. 95, no. 12, pp. 7940–7953, 2004.

[118] L. L. Smith, R. F. Davis, R.-J. Liu, M. J. Kim, and R. W. Carpenter, "Microstructure, electrical properties, and thermal stability of Ti-based ohmic contacts to n-GaN," *Journal of Materials Research*, vol. 14, no. 3, p. 1032–1038, 1999.

[119] L. Dobos, B. Pécz, L. Tóth, Z. Horváth, Z. Horváth, E. Horváth, A. Tóth, B. Beaumont, and Z. Bougrioua, "Al and Ti/Al contacts on n-GaN," *Vacuum*, vol. 84, no. 1, pp. 228 – 230, 2009.

[120] J. O. Song, J. Ha, and T. Seong, "Ohmic-Contact Technology for GaN-Based Light-Emitting Diodes: Role of p-Type Contact," *IEEE Transactions on Electron Devices*, vol. 57, pp. 42–59, Jan 2010.

[121] D. J. King, L. Zhang, J. C. Ramer, S. D. Hersee, and L. F. Lester, "Temperature Behavior of Pt/Au Ohmic Contacts to p-GaN," *MRS Proceedings*, vol. 468, p. 421, 1997.

[122] J. Xie, X. Ni, Q. Fan, R. Shimada, U. Ozgur, and H. Morkoc, "On the efficiency droop in InGaN multiple quantum well blue light emitting diodes and its reduction with p-doped quantum well barriers," *Applied Physics Letters*, vol. 93, no. 12, pp. –, 2008.

[123] H.-Y. Ryu and J.-I. Shim, "Effect of current spreading on the efficiency droop of InGaN light-emitting diodes," *Opt. Express*, vol. 19, pp. 2886–2894, Feb 2011.

[124] M. Yamada, T. Mitani, Y. Narukawa, S. Shioji, I. Niki, S. Sonobe, K. Deguchi, M. Sano, and T. Mukai, "InGaN-Based Near-Ultraviolet and Blue-Light-Emitting Diodes with High External Quantum Efficiency Using a Patterned Sapphire Substrate and a Mesh Electrode," *Japanese Journal of Applied Physics*, vol. 41, no. 12B, p. L1431, 2002.

[125] D.-H. Youn, Y.-J. Yu, H. Choi, S.-H. Kim, S.-Y. Choi, and C.-G. Choi, "Graphene transparent electrode for enhanced optical power and thermal stability in GaN light-emitting diodes," *Nanotechnology*, vol. 24, no. 7, p. 075202, 2013.

[126] J. Song, D.-S. Leem, J. S. Kwak, Y. Park, S. W. Chae, and T. Seong, "Improvement of the luminous intensity of light emitting diodes by using highly transparent Ag-indium tin oxide p-type Ohmic contacts," *IEEE Photonics Technology Letters*, vol. 17, pp. 291–293, Feb 2005.

[127] J.-K. Ho, C.-S. Jong, C. C. Chiu, C.-N. Huang, C.-Y. Chen, and K.-K. Shih, "Low-resistance ohmic contacts to p-type GaN," *Applied Physics Letters*, vol. 74, no. 9, pp. 1275–1277, 1999.

[128] J.-O. Song, H.-G. Hong, J.-W. Jeon, J.-I. Sohn, J.-S. Jang, and T.-Y. Seong, "Possible Ohmic Mechanisms of Ag/Indium Tin Oxide p-Type Contacts for High-Brightness GaN -Based Light Emitting Diodes," *Electrochemical and Solid-State Letters*, vol. 11, no. 2, pp. H36–H38, 2008.

[129] D. C. Look, D. C. Reynolds, J. W. Hemsky, J. R. Sizelove, R. L. Jones, and R. J. Molnar, "Defect Donor and Acceptor in GaN," *Phys. Rev. Lett.*, vol. 79, pp. 2273–2276, Sep 1997.

[130] C. Tun, J.-K. Sheu, B.-J. Pong, M.-L. Lee, M.-Y. Lee, C.-K. Hsieh, C.-C. Hu, and G.-C. Chi, "Enhanced Light Output of GaN-Based Power LEDs with Transparent Al-Doped ZnO Current Spreading Layer," *Photonics Technology Letters, IEEE*, vol. 18, pp. 274 – 276, 02 2006.

[131] R. C. Jaeger, *Introduction to Microelectronic Fabrication.* Pearson, 2nd ed., 2001.

[132] D. Rawal, B. Sehgal, R. Muralidharan, H. Malik, and A. Dasgupta, "Effect of BCl_3 concentration and process pressure on the GaN mesa sidewalls in BCl_3/Cl_2 based inductively coupled plasma etching," *Vacuum*, vol. 86, pp. 1844–1849, July 2012.

[133] T. Wang, W. Hsu, Y. Che, and Y. Chen, "Inductively Coupled Plasma Mesa Etched InGaN/GaN Light Emitting Diodes Using Cl_2 /BCl_3 /Ar Plasma," *Japanese Journal of Applied Physics*, vol. 45, pp. 6800–6802, Sept. 2006.

[134] D. M. Mattox, *The Foundations of Vacuum Coating Technology.* Springer-Verlag Berlin Heidelberg, 1st ed., 2003.

[135] L. Reimer, *Scanning Electron Microscopy* . Springer, Berlin, Heidelberg, 1st ed., 1985.

[136] R. Reifenberger, *Fundamentals of Atomic Force Microscopy.* World Scientific, 2015.

[137] Q. Shan, *Non-Ideal Properties of Gallium Nitride Based Light-Emitting Diodes.* PhD thesis, Rensselaer Polytechnic Institute, 2012.

[138] Q. Shan, D. S. Meyaard, Q. Dai, J. Cho, E. Fred Schubert, J. Kon Son, and C. Sone, "Transport-mechanism analysis of the reverse leakage current in GaInN light-emitting diodes," *Applied Physics Letters*, vol. 99, no. 25, 2011.

[139] H. C. Casey, J. Muth, S. Krishnankutty, and J. M. Zavada, "Dominance of tunneling current and band filling in InGaN/AlGaN double heterostructure blue light emitting diodes," *Applied Physics Letters*, vol. 68, no. 20, pp. 2867–2869, 1996.

[140] J. Kim, J. Kim, Y. Tak, J. Kim, H. Hong, M. Yang, S. Chae, J. Park, Y. Park, and U.-I. Chung, "Investigation of Reverse Leakage Characteristics of InGaN/GaN Light-Emitting Diodes on Silicon," *Electron Device Letters, IEEE*, vol. 33, pp. 1741–1743, Dec 2012.

[141] J. Frenkel, "On Pre-Breakdown Phenomena in Insulators and Electronic Semi-Conductors," *Phys. Rev.*, vol. 54, pp. 647–648, 1938.

[142] P. van der Heide, *Secondary Ion Mass Spectrometry: An Introduction to Principles and Practices.* Wiley, 2014.

[143] J. D. Zook, "Theory of beam-induced currents in semiconductors," *Applied Physics Letters*, vol. 42, no. 7, pp. 602–604, 1983.

[144] K. Cavanagh, C. Liu, T. Martin, M. A. Hopkins, S. Sivaraya, and D. W. E. Allsopp, "Detailed optical and electrical characterisation of green - orange InGaN/GaN LEDs grown by MOVPE," in *The Tenth International Conference on Advanced Semiconductor Devices and Microsystems*, pp. 1–4, Oct 2014.

[145] M. J. Wallace, P. R. Edwards, M. J. Kappers, M. A. Hopkins, F. Oehler, S. Sivaraya, D. W. E. Allsopp, R. A. Oliver, C. J. Humphreys, and R. W. Martin, "Bias dependence and correlation of the cathodoluminescence and electron beam induced current from an InGaN/GaN light emitting diode," *Journal of Applied Physics*, vol. 116, no. 3, 2014.

[146] T. Hikosaka, T. Narita, Y. Honda, M. Yamaguchi, and N. Sawaki, "Optical and electrical properties of (1-101)GaN grown on a 7 off-axis (001)Si substrate," *Applied Physics Letters*, vol. 84, no. 23, pp. 4717–4719, 2004.

[147] B. Heying, E. J. Tarsa, C. R. Elsass, P. Fini, S. P. DenBaars, and J. S. Speck, "Dislocation mediated surface morphology of GaN," *Journal of Applied Physics*, vol. 85, no. 9, pp. 6470–6476, 1999.

[148] M. Missous and E. Rhoderick, "New way of plotting current/voltage characteristics of Schottky diodes," *Electronics Letters*, vol. 22, pp. 477–478, April 1986.

[149] P. H. Bueno, D. F. Costa, A. Eick, A. Carvalho, and D. W. L. Monteiro, "The behavior of series resistance of a p-n junction: the diode and the solar cell cases," in *Proc.SPIE*, vol. 9743, pp. 9743 – 9743 – 9, 2016.

[150] Y. D. Qi, H. Liang, D. Wang, Z. D. Lu, W. Tang, and K. M. Lau, "Comparison of blue and green InGaN GaN multiple quantum well light emitting diodes grown by metalorganic vapor phase epitaxy," *Applied Physics Letters*, vol. 86, no. 10, p. 101903, 2005.

[151] A. Mao, J. Cho, Q. Dai, E. F. Schubert, J. K. Son, and Y. Park, "Characteristics of dotlike green satellite emission in GaInN light emitting diodes," *Applied Physics Letters*, vol. 98, no. 2, pp. –, 2011.

[152] M. Schillgalies, A. Laubsch, S. Lutgen, A. Avramescu, G. Braderl, D. Queren, and U. Strauss, "Defect-related recombination in InGaN-lasers," *Physica status solidi (c)*, vol. 5, no. 6, pp. 2192–2194, 2008.

[153] L. S. Wang, W. K. Fong, C. Surya, K. W. Cheah, W. H. Zheng, and Z. G. Wang, "Photoluminescence of rapid-thermal annealed Mg-doped GaN films," *Solid-State Electronics*, vol. 45, pp. 1153–1157, 2001.

[154] J.-S. Park, D. W. Fothergill, P. Wellenius, S. M. Bishop, J. F. Muth, and R. F. Davis, "Origins of Parasitic Emissions from 353 nm AlGaN-based Ultraviolet Light Emitting Diodes over SiC Substrates," *Japanese Journal of Applied Physics*, vol. 45, no. 5R, p. 4083, 2006.

[155] R.-H. Horng, D.-S. Wuu, Y.-C. Lien, and W.-H. Lan, "Low-resistance and high-transparency Ni/indium tin oxide ohmic contacts to p-type GaN," *Applied Physics Letters*, vol. 79, no. 18, pp. 2925–2927, 2001.

[156] R.-H. Horng, D.-S. Wuu, Y.-C. Lien, and W.-H. Lan, "Low-resistance and high-transparency Ni/indium tin oxide ohmic contacts to p-type GaN," *Applied Physics Letters*, vol. 79, no. 18, pp. 2925–2927, 2001.

[157] C. L. Tseng, M. J. Youh, G. P. Moore, M. A. Hopkins, R. Stevens, and W. N. Wang, "Mechanism for the increased light transmission through Ni/Au/ZnO contacts on p-GaN for high power optoelectronic devices," *Applied Physics Letters*, vol. 83, no. 18, pp. 3677–3679, 2003. ID number: ISI:000186256300011.

[158] J. O. Song, J. Ha, and T. Seong, "Ohmic Contact Technology for GaN Based Light Emitting Diodes: Role of p-Type Contact," *IEEE Transactions on Electron Devices*, vol. 57, pp. 42–59, Jan 2010.

[159] D. Chen, J. Lu, R. Lu, L. Chen, and Z. Ye, "High-Performance GaN-Based LEDs With AZO/ITO Thin Films as Transparent Contact Layers," *IEEE Transactions on Electron Devices*, vol. 64, no. 6, pp. 2549–2555, 2017.

[160] V. Avrutin, U. Ozgur, H. Morkoc, K. Ding, U. Özgür, and H. Morkoç, "Status of Growth of Group III-Nitride Heterostructures for Deep Ultraviolet Light-Emitting Diodes," *Crystals.*, vol. 7, no. 10, 2017.

[161] C. S. Lin, K. Cavanagh, H. C. L. Tsui, A. Mihai, B. Zou, D. W. E. Allsopp, and M. A. Moram, "Ultraviolet emission from resonant tunnelling Metal/Insulator/Semiconductor light emitting tunnel diodes," *IEEE Photonics Journal*, vol. 9, no. 4, pp. 1–8, 2017.

[162] M. J. Hanna, H. Zhao, and J. C. Lee, "Poole frenkel current and schottky emission in sin gate dielectric in algan/gan metal insulator semiconductor heterostructure field effect transistors," *Applied Physics Letters*, vol. 101, no. 15, p. 153504, 2012.

[163] H. Ryu, D. Shin, and J. Shim, "Analysis of efficiency droop in nitride light-emitting diodes by the reduced effective volume of InGaN active material," *Applied Physics Letters*, vol. 100, no. 13, p. 131109, 2012.

[164] H. Huang, G. Fang, X. Mo, H. Long, L. Yuan, B. Dong, X. Meng, and X. Zhao, "ZnO-based fairly pure ultraviolet light-emitting diodes with a low operation voltage," *IEEE Electron Device Letters*, vol. 30, pp. 1063–1065, Oct 2009.

[165] L. Iogansenm, "The possibility of resonance transmission of electrons in crystals through a system of barriers," *Sov. Phys. Jetp-USSR*, vol. 18, pp. 146–150, 1964.

[166] R. H. Fowler and L. Nordheim, "Electron emission in intense electric fields," *Proceedings of the Royal Society of London. Series A, Containing Papers of a Mathematical and Physical Character*, vol. 119, no. 781, pp. 173–181, 1928.

[167] F. Chiu, "A Review on Conduction Mechanisms in Dielectric Films," *Advances in Materials Science and Engineering*, vol. 2014, pp. 1–18, 2014.

[168] X. Aymerich-Humet and F. Serra-Mestres, "Resonant tunneling current for general junction potential barrier," *Physica status solidi (a)*, vol. 51, no. 2, 1979.

[169] P. Chowdhury, H. C. Barshilia, N. Selvakumar, B. Deepthi, K. Rajam, A. R. Chaudhuri, and S. Krupanidhi, "The structural and electrical properties of TiO2 thin films prepared by thermal oxidation," *Physica B: Condensed Matter*, vol. 403, no. 19, pp. 3718 – 3723, 2008.

[170] S. Z. M. M. Bülbül, "Frequency dependent capacitance and conductance-voltage characteristics of Al/Si3N4/p-Si(1 0 0) MIS diodes," *Microelectron. Eng*, vol. 83, no. 11–12, 2006.

[171] J. Yan, J. Wang, P. Cong, L. Sun, N. Liu, Z. Liu, C. Zhao, and J. Li, "Improved performance of UV-LED by p-AlGaN with graded composition," *Phys. Status Solidi*, vol. 8, no. 2, pp. 461–463, 2011.

[172] S. Sheng, G. Fang, C. Li, S. Xu, and X. Zhao, "P-type transparent conducting oxides," *Physica Status Solidi (a)*, vol. 203, no. 8, pp. 1891–1900, 2006.

[173] G. Phipps, C. Mikolajczak, and T. Guckes, "Indium and Gallium: long-term supply," *Renewable Energy Focus*, vol. 9, no. 4, pp. 56 – 59, 2008.

[174] K. Song, M. Mohseni, and F. Taghipour, "Application of ultraviolet light-emitting diodes (UV-LEDs) for water disinfection: A review," *Water Research*, vol. 94, 03 2016.